AD NUMBER

AD821674

LIMITATION CHANGES

TO:

Approved for public release; distribution is unlimited.

FROM:

Distribution authorized to U.S. Gov't. agencies and their contractors; Critical Technology; AUG 1967. Other requests shall be referred to Air Force Space and Missile Systems Organization, Norton AFB, CA. This document contains export-controlled technical data.

AUTHORITY

samso usaf ltr, 28 feb 1972

TURBULENCE MEASUREMENTS IN AN AXISYMMETRIC COMPRESSIBLE WAKE

Publication No. UG-4118

TECHNICAL REPORT

TURBULENCE MEASUREMENTS IN AN AXISYMMETRIC COMPRESSIBLE WAKE

Monitored By: Ballistic Systems Division
Air Force Systems Command
Norton Air Force Base, California

Under Contract: AF 04(694)-994

Sponsored By: Advanced Research Projects Agency
Department of Defense
ARPA Order No. 888, Amendment No. 1

Prepared By: A. Demetriades

1 August 1967

PHILCO-FORD CORPORATION
Space and Re-entry Systems
Newport Beach, California

PREFACE

This report is the second of a series describing experimental work presently under way at Philco-Ford Corporation on the character of compressible free turbulent flows, and especially on the characteristics of hypersonic wakes. It deals with the measurement and the spatial and spectral resolution of fluctuations in an axi-symmetric compressible wake and discusses the similarity rules by which these results can be extended to higher speeds. This work has been preceded by Philco-Ford Report No. U-3978, "Mean-Flow Measurements in an Axi-symmetric Compressible Turbulent Wake," 1 March 1967, in which measurements of the mean properties of the wake dealt with herein were presented. A third report, "Turbulent Front Structure of an Axi-symmetric Compressible Wake," describing the intermittency measurements, is being prepared.

The author acknowledges with gratitude, the financial support and encouragement of the Advanced Research Projects Agency, the Space and Missile Systems Organization, USAF, and the Philco-Ford Corporation; the Analysis Section of the latter was especially helpful with the machine programming and computations. Special thanks are also due Dr. John Laufer, Consultant, for many stimulating discussions, and Mr. Lee Von Seggern, whose expert assistance with the equipment and instrumentation proved of great value in this work.

ABSTRACT

The turbulence characteristics of an axi-symmetric wake shed by a very slender body at Mach 3 have been measured with the hot-wire anemometer. The region covered began at transition, located immediately downstream of the model, and ended about 100 virtual wake diameters downstream. By using computer-aided corrections to the anemometer frequency response, maps of the temperature and axial velocity fluctuations, their cross-correlations, spectral density, and auto correlation macroscales were obtained as a function of the axial and radial coordinates. Beyond 40 wake diameters from the virtual origin, dynamic equilibration forces these distributions into seemingly self-preserving forms. These forms are identical with their imcompressible counterparts except for a coordinate transformation already suggested by the dynamic equilibrium hypothesis and the Reynolds analogy typical of adiabatic flows. The density macroscale is numerically smaller than that of the velocity, although they both approximate the transverse wake scale. Away from the axis, both the fluctuation magnitudes and their spectral densities are distorted by the pseudoturbulence generated by the intermittent boundary, which was found to be a weakly periodic structure with a wavelength on the order of the wake diameter.

NOMENCLATURE

A	Transfer function of voltmeter detector
A'_w	Dimensionless hot-wire overheat (Equation (21))
C	Transfer function of amplifier (Equation (6))
c	Heat capacity of hot-wire
c_f	Function of hot-wire finite circuit factor
$C_D A$	Virtual turbulent wake diameter (squared)
e	Actual rms frequency-integrated output of overall system (rms volts)
e^*	Ideal rms frequency-integrated output of overall system (rms volts)
$\bar{e}$	Mean voltage across hot-wire
$e(f)$	Rms voltage output of system within passband at frequency f (modally unresolved)
$e(f)_{flow}$	Rms voltage "input" at frequency f into the wire (or, same type of voltage output from a perfect wire)
$e(f)_{wire}$	Rms voltage output at frequency f from wire (including its lag)
$e(f)_{amp}$	Same as above, but at amplifier output
$e(f)_{comp}$	Same as above, but at compensator output

NOMENCLATURE (Continued)

$e^{*2}(f)$	Ideal mean-square output of system at frequency f
e^2_{VTVM}	Vacuum-tube (mean-square) voltmeter output of entire system: actual system
e^{*2}_{VTVM}	Same as above: ideal system
E^2	Equation (3)
E'	Equation (12)
e_m	Hot-wire sensitivity to mass-flux fluctuations
e_t	Hot-wire sensitivity to total temperature fluctuations
e_σ	Hot-wire sensitivity to entropy (temperature) fluctuations
e_τ	Hot-wire sensitivity to vorticity (velocity) fluctuations
f	Frequency (dimensional)
f_B	Frequency passband used (dimensional)
$f(\eta)$	Universal function of similarity radial distribution of fluctuations
$g(\eta)$	Universal function of similarity radial distribution of fluctuations
$g(0)$	Value of g on axis
G	Amplifier gain
G_o	Amplifier gain at zero frequency
H	Wave-analyzer transfer function
I	Hot-wire current
J	Error ratio (Equation (16))
K	Function of hot-wire overheat

NOMENCLATURE (Continued)

l	Hot-wire length
L	Transverse scale of wake
m	Local mass-flux (product ρu)
M	Mach number
M	Wire time constant
M_I	Hot-wire constant at current I
M_s	Time constant of amplifier
n_T	Nondimensional frequency (based on velocity macroscale)
n_s	Nondimensional frequency (based on density macroscale)
Nu_o	Hot-wire Nusselt number based on stagnation conductivity
OTF	Overall transfer function
p	pressure
p_t	Pitot pressure
r	Density defect (Equation (86))
R	Hot-wire resistance
r_{mt}	Mass-flux-total temperature cross-correlation coefficient
$r_{\sigma\tau}$	Velocity-temperature cross-correlation coefficient
R_I	Hot-wire resistance at current I
R_r	Recovery resistance of wire
R_w	Heated resistance of wire
R_T	Turbulent Reynolds number

NOMENCLATURE (Continued)

Re_o	Wire Reynolds number (based on stagnation viscosity)
S	Function of the turbulent Prandtl number
t	Nondimensional total temperature fluctuation
T	Temperature
T_o	Total (local) temperature
$\tilde{T}$	Nondimensional temperature (Equation (88))
u	Axial velocity
$\tilde{u}$	Nondimensional axial velocity (Equation (87))
U	Local velocity scale (Equation (57))
V	Wave analyzer output (volts dc)
V_m	Same as V
V_n	Noise output of wave analyzer (volts dc)
w	Velocity defect (Equation (64))
W	Compensator transfer function
WEB	Designation of present experiment
WEB-Q	Q (= I, II.....) designation of computer program
X	Axial coordinate
$\bar{X}$	Nondimensional axial coordinate (Equation (81))
X_o	Axial position of virtual origin
X-Station	Axial position of measurements
Y	Radial coordinate
α	Function of Mach number (Equation (37))
α_r	Temperature coefficient of resistivity at recovery temperature

NOMENCLATURE (Continued)

β	Function of the Mach number (Equation (38))
γ	Ratio of specific heat
ΔQ	Rms value of the local variable Q
Δf	Frequency interval
ϵ	Finite circuit factor
η	Hot-wire recovery factor
η	Nondimensional radial coordinate (Equation (60))
θ	Temperature defect (Equation (85))
Λ_S	Autocorrelation macroscale of the density fluctuations
Λ_T	Autocorrelation macroscale of the velocity fluctuations
ρ	Local density of flow
ρ'	Density scale
$\tilde{\rho}$	Nondimensional density (Equation (89))
σ	Rms nondimensional frequency-integrated temperature (density) fluctuation
$\sigma(f)$	Same as above but within a passband Δf (i.e., density fluctuation density)
σ_T	Turbulent Prandtl number
τ	Rms nondimensional frequency-integrated velocity fluctuation
$\tau(f)$	Same as above but within a passband Δf (i.e., velocity fluctuation density)
τ_{wr}	Function of the wire overheat

Indices

∞	Conditions external to wake
(0)	Conditions on axis

CONTENTS

CONTENTS (Continued)

APPENDICES

ILLUSTRATIONS

ILLUSTRATIONS (Continued)

ILLUSTRATIONS (Continued)

ILLUSTRATIONS (Continued)

ILLUSTRATIONS (Continued)

ILLUSTRATIONS (Continued)

ILLUSTRATIONS (Continued)

SECTION 1

INTRODUCTION

Renewed interest in the study of turbulence in compressible wakes has been generated by the need to predict the radar-scattering characteristics of re-entry flow fields. Formidable difficulties in fluid mechanics and chemistry have directed current research toward two distinct goals. One is the study of the wake turbulent structure itself; the other is a search for the link between the gasdynamical and electronic turbulence properties of a hydrodynamically turbulent plasma. This report addresses itself to the first problem.

Because high-speed wakes involve fluctuations in the pressure, density, and temperature in addition to the velocity, unknowns of interest should now include the density or temperature fluctuation magnitude and its radial and axial distributions, as well as the distribution of spectra, autocorrelation functions, and scales of the same properties. To these, one should add the statistical distribution of fluctuation magnitudes and, of course, the intermittency characteristics of the turbulent boundary. Further, there are two idiosyncracies of the compressible wake which bear heavily on the design of an experiment. First, the inviscid gradients generated by vehicle shock waves force the wake to grow into a nonuniform stream; this puts a premium on the search for the self-preserving characteristics of the turbulent

wake so that the turbulent structure can be predicted regardless of inviscid gradients. Second, in contrast to low speeds, transition in the supersonic wake can occur at some distance behind the vehicle; the question arises as to the initial values of the turbulence properties in the transition zone.

Very little has been done to answer these questions. Most of the available information comes from two sources; low-speed experiments (References 1 through 5) and very recent attempts to measure these properties in ballistic ranges (References 6 and 7). The attractiveness of producing wakes with hypervelocity pellets in the latter is severely offset by two factors; first, the lack of pellet path control and probe position; and, second, difficulties with Taylor's hypothesis (Reference 8). For example, it is impossible to perform repeated shots with slender bodies at zero angle of attack and to control, a priori, the path of the probe in the wake; the radial position of the measurement point is therefore always in doubt, and measurements near the wake axis obviously cannot be made for many tens (perhaps hundreds) of base diameters. However, at these far distances, the mean flow velocity around the probe might be so low that the turbulence structure might change significantly; the so-called Taylor's hypothesis, which is crucial to the interpretation of data, is thus invalid.

We conclude that ballistic range experiments, although of qualitative value at high Mach numbers, cannot match the precision and accuracy of wind tunnel work in this regard.

In the meantime, attempts have been made to approach the problem theoretically; several are summarized in Reference 9. Recently, Morkovin (Reference 10) correlated low- and high-speed experimental data within the scope of the so-called dynamic equilibrium hypothesis and his suggestions were expanded by Laufer (Reference 11) specifically to the axi-symmetric hypersonic wake. The power of this latter approach lies in the dependence on concepts verified experimentally (Reference 1) and on its potential of providing useful predictions for the hypersonic wake by unifying incompressible and compressible behavior into relatively simple rules. By virtue of both its simplicity and promise, this theory will play a central role in interpreting the present experimental data.

No wind tunnel turbulence measurements of compressible wake flows have been reported to date. Such experiments are held back mainly by shortcomings of hot-wire anemometry and, in the case of axi-symmetric wakes, by the difficulty of suspending axi-symmetric models at high speeds. Of these two problems, the former is the most serious, and was overcome in the present experiment by a complex and admittedly laborious process.

The present work deals with the turbulent field alone and has been preceded by a detailed study of the mean (time-averaged) flow field in the axi-symmetric wake. These mean-flow measurements, described in Reference 12, are necessary in order to compute the sensitivity of the hot wire to the different modes of turbulence and to relate the turbulence properties to the local and integral properties of the flow. The reader should consult Reference 12 for details regarding the mean-flow properties and the instrumentation and techniques by which these properties were measured.

SECTION 2

APPARATUS AND TECHNIQUE

2.1 WIND TUNNEL AND MODEL

The experiment was performed at Mach 3 in a continuous air wind tunnel. The wake was produced by a circular rod supported by a strut upstream of the nozzle throat and cantilevered into the test section through the throat. The Reynolds number in the test section was 50,000 per cm, generated by a tunnel total pressure and temperature of 508 mm Hg abs and 27°C, respectively. Further details on the tunnel itself appear in Reference 13.

2.2 GENERAL FEATURES OF THE FLOW FIELD

Figure 1 shows a schematic view of the model and wake flow. The wake is formed by the boundary layer shed off the body; transition to turbulence could be located at will along the axi-symmetric wake by changing the tunnel total (supply) pressure. At the chosen pressure of 508 mm Hg, transition lies between about 10 and 15 base diameters downstream of the base, allowing for the maximum turbulent wake length accessible to probes; at the same time, the wake is relatively thinner than would be obtained if transition was moved to the model surface. Furthermore, since laminar reattachment (at the wake neck) incurs a lower pressure rise than turbulent reattachment, inviscid gradients around the wake were extremely mild; the

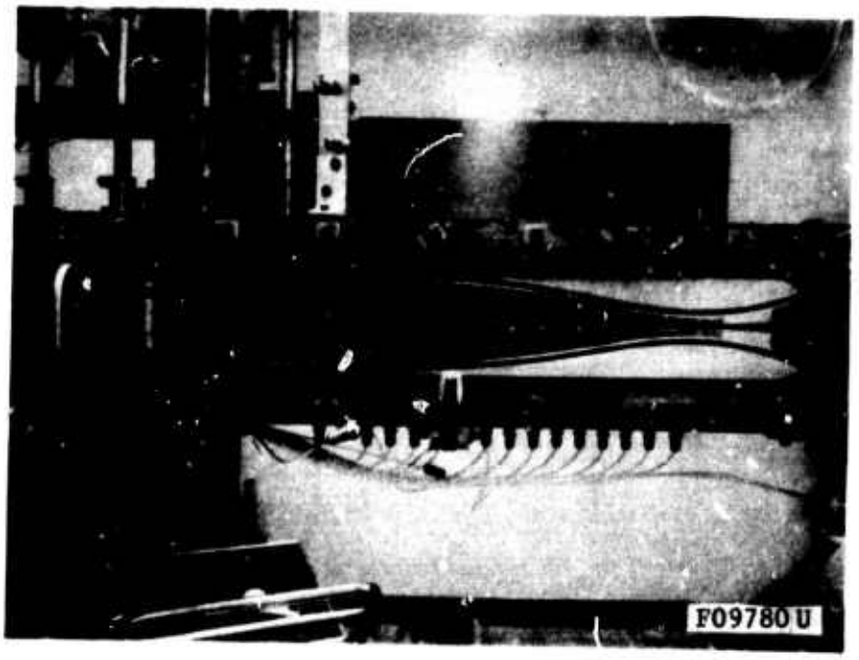

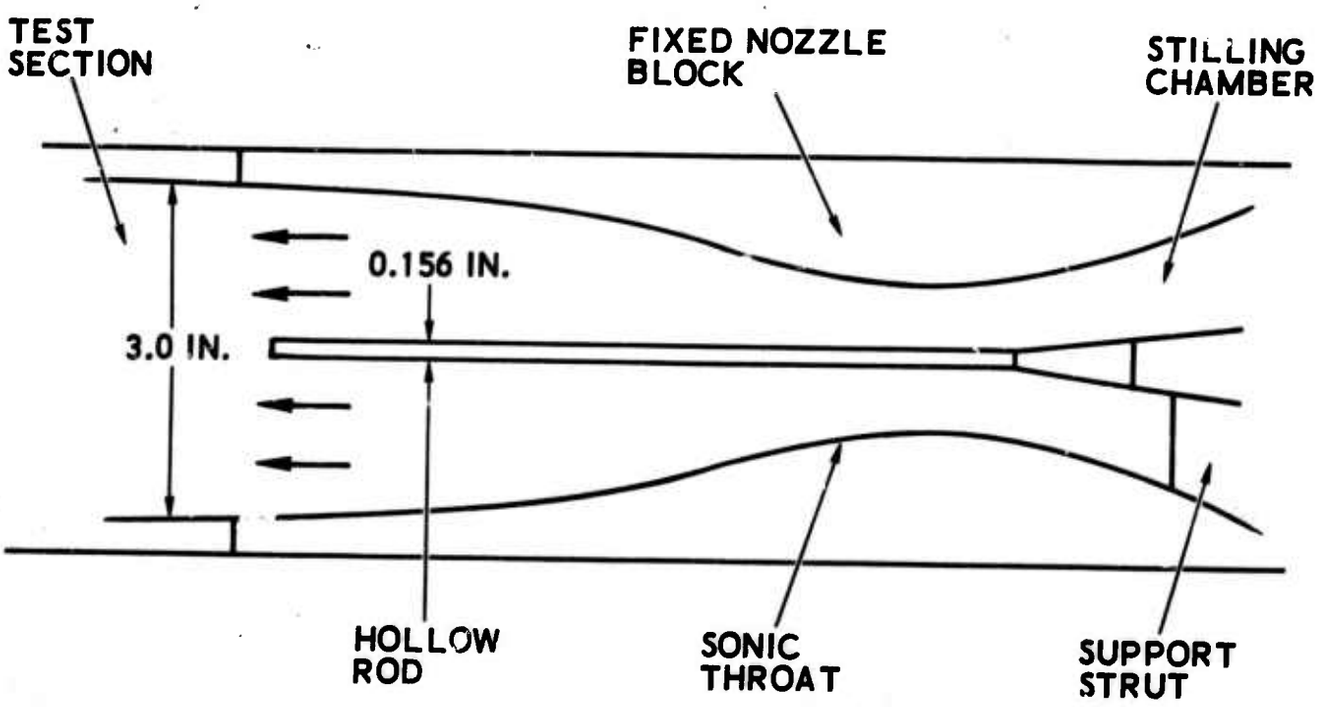

F09781 U

FICURE 1. TOP: PHOTOGRAPH OF TEST SECTION SHOWING AXISYMMETRIC MODEL AT LEFT, PROBE AT LEFT AND PROBE ACTUATOR (TOP LEFT). BOTTOM: DETAILS OF THE AXISYMMETRIC MODEL.

wake shock disappeared completely at this pressure and the Mach number external to the turbulent region was 2.96 ±0.02 for the entire wake length.

2.3 HOT-WIRE ANEMOMETER

The turbulence properties were measured with a single 0.00005-inch-diameter, 0.01-inch-long pt 10% Rh wire; the hot-wire probe is pictured in Figure 2. Prior to use, each wire underwent a temperature-resistance calibration in a controlled oven and a calibration of its heat-transfer characteristics in a known supersonic flow external to the wake. The details of these preparatory steps are given in Reference 12, together with numerical results of the calibrations.

The single most important precaution in mounting the hot wire for use was its strain gage characteristic. The problem, arising from structural oscillations of the wire in the flow and superposing on the output spectrum numerous misleading energy peaks, has been thoroughly described by Morkovin (Reference 14). By using only those wires with significant slack (e.g., a quarter-circle), it was possible to obtain completely undistorted spectra. In practice, each single wire was routinely subjected to a test whereby its output spectrum in the turbulent wake was obtained prior to use. A wave analyzer with a mechanically driven frequency sweep was especially helpful in these tests. In practice, about 80 percent of the wires mounted were rejected because the spectrum so obtained showed discernible strain gage problems, of the type shown in Figure 3.

Spatial resolution of the wire in the transverse direction was controlled, of course, by its length, which was 0.01 inch. By contrast, the wake diameter was about 0.30 inch on the average so that the probe resolution was of order 1/30. It should be also noted that the wire was positioned at all times along a direction normal to the distance between it and the wake axis. In addition to the spatial resolution necessary for these measurements, the temporal resolution was of great importance. This was controlled by the wire time-constant limit at zero current (on the order

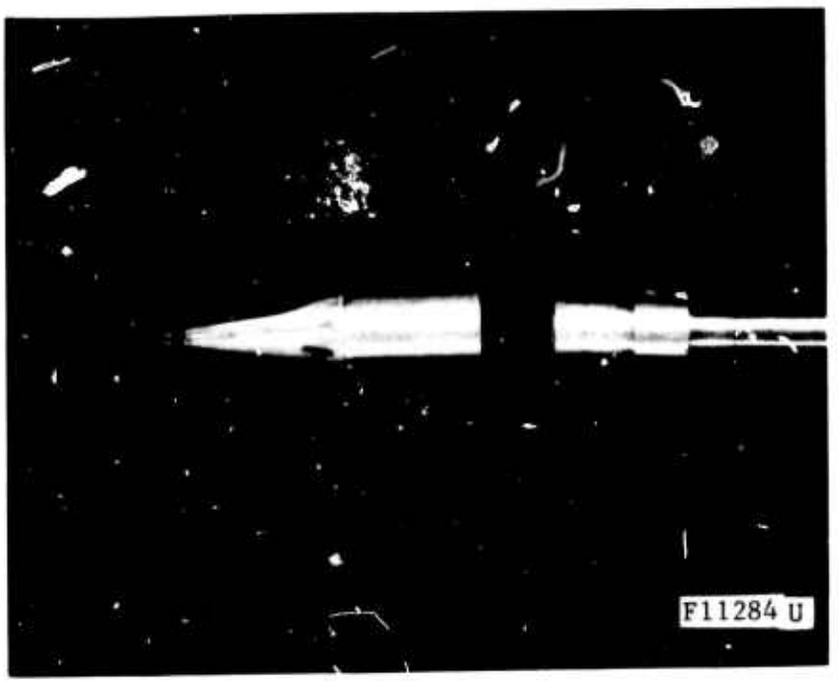

FIGURE 2. HOT-WIRE ANEMOMETER PROBE SHOWN AT NEARLY FULL-SCALE AND ABOUT 100 X MAGNIFICATION (BELOW, RIGHT)

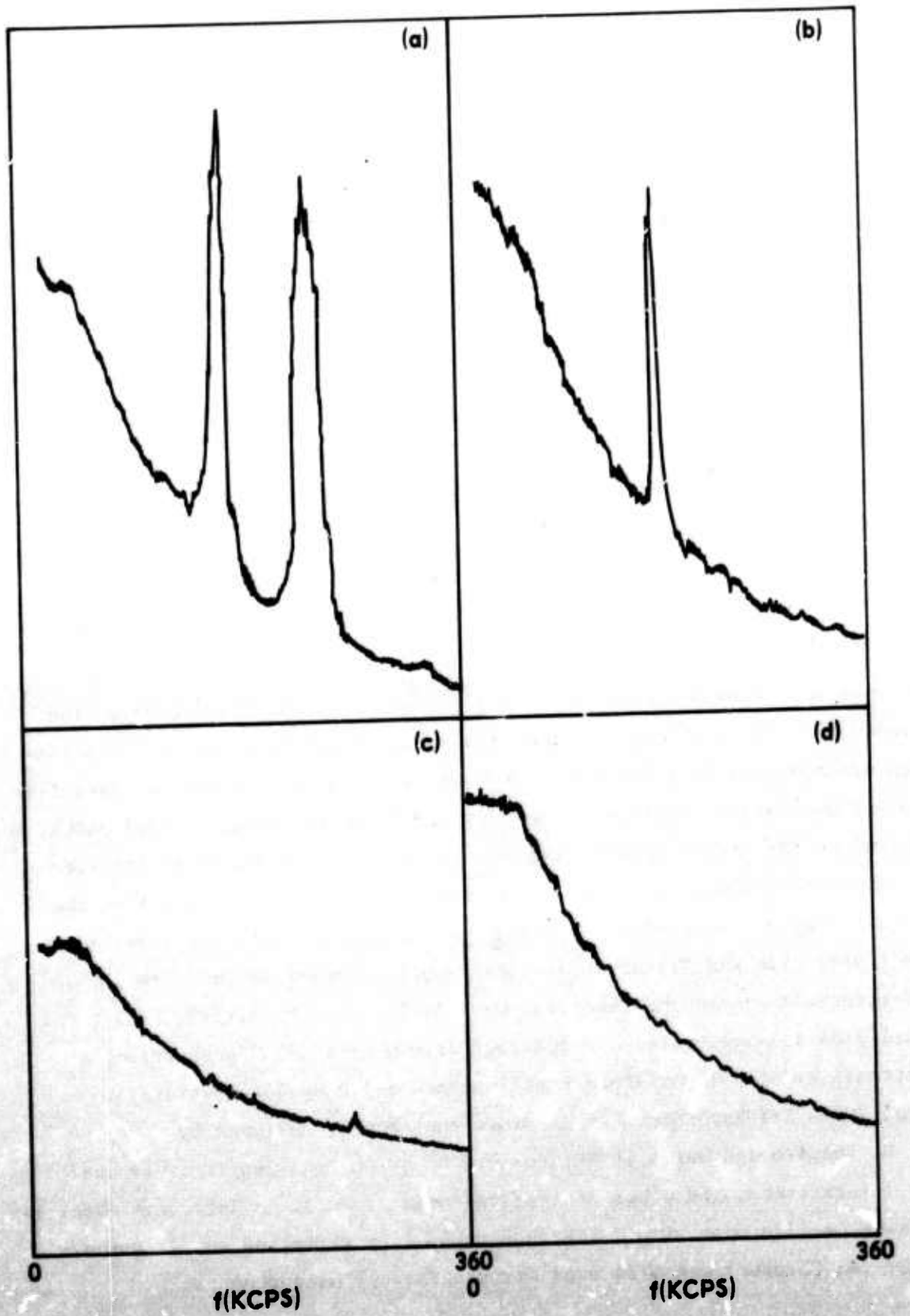

F09812 U

FIGURE 3. STRAIN-GAGE CHARACTERISTICS OF HOT-WIRES PLOTTED AS INTEGRATED WIRE OUTPUT VS. FREQUENCY. TOP LEFT: SEVERE TOP RIGHT: TYPICAL, BOTTOM LEFT: ACCEPTABLE BOTTOM RIGHT: IDEAL (CURVES REPRODUCED DIRECTLY FROM X-Y PLOTTER SPECTRA)

of 0.1 millisecond) and the floor-to-ceiling ratio of the compensating amplifier, which was 500 in the present instance. The resulting frequency response of 800 kilocycles per second represented, when divided by the free-stream velocity, a scale of about 0.2 the body diameter. This shortcoming was significant but not prohibitive and, as will be seen below, was overcome by detailed spectral measurements at the higher frequencies. The frequency response of the anemometer (its transfer function) is discussed in Appendix A. An idea of the response speed of the instrument under typical operating conditions can be obtained from Figure 4.

2.4 ELECTRONIC INSTRUMENTATION

A block diagram of the instrumentation necessary to record the turbulence data is shown in Figure 5; the same equipment was earlier used for the mean measurements.

The wire was powered by mercury cells contained in the Transmetrics, Inc. Model 6401-1 Current Control Panel, and signal amplification and compensation was achieved by a Transmetrics Model 6401-5 Constant Current Amplifier and a Model 6401-7 Square Wave Generator. A Hewlett-Packard Model 3440A Digital Voltmeter and a switching circuit selectively displayed the wire current and voltage, alleviating the need of bridge-balancing during the probe traverse. Measurement and display instruments included a Ballantine Model 320A true RMS Voltmeter, a Singer-Metrics Model SB-76Z 1 to 300-kilocycle-per-second Panoramic Wave Analyzer, a Hewlett-Packard Model 310A 1.5-megacycle Wave Analyzer driven by a 297A Sweep Drive, a Tektronix Model 551 Dual-Beam Oscilloscope, and a Hewlett-Packard Model 7000A X-Y Recorder. An intermittency meter, designed by Dr. H. Shapiro and built at Philco-Ford by Mr. L. Von Seggern, was used for intermittency and other statistical measurements. A Tektronix Model 549 Storage Oscilloscope with dual-trace capability (effected by a Tektronix Model 1A1 Chopper) was also used for statistical measurements.

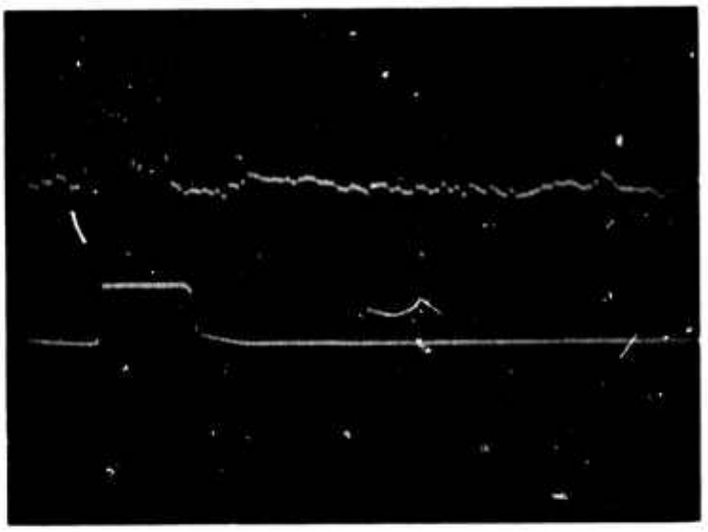

FIGURE 4. TYPICAL OSCILLOGRAM OF INTERMITTENT WIRE OUTPUT NEAR WAKE EDGE. TOP TRACE IS VOLTAGE OUTPUT SHOWING A 15-MICROSECOND "EVENT" DURING WHICH THE WIRE IS IMMERSED IN TURBULENCE. BOTTOM TRACE IS RECTIFIED ANALOG OF THE TOP TRACE, USED FOR MEASURING THE INTERMITTENCY FACTOR. NOTE FAST HOT-WIRE RESPONSE: DOTS ARE SPACED ONE MICROSECOND APART.

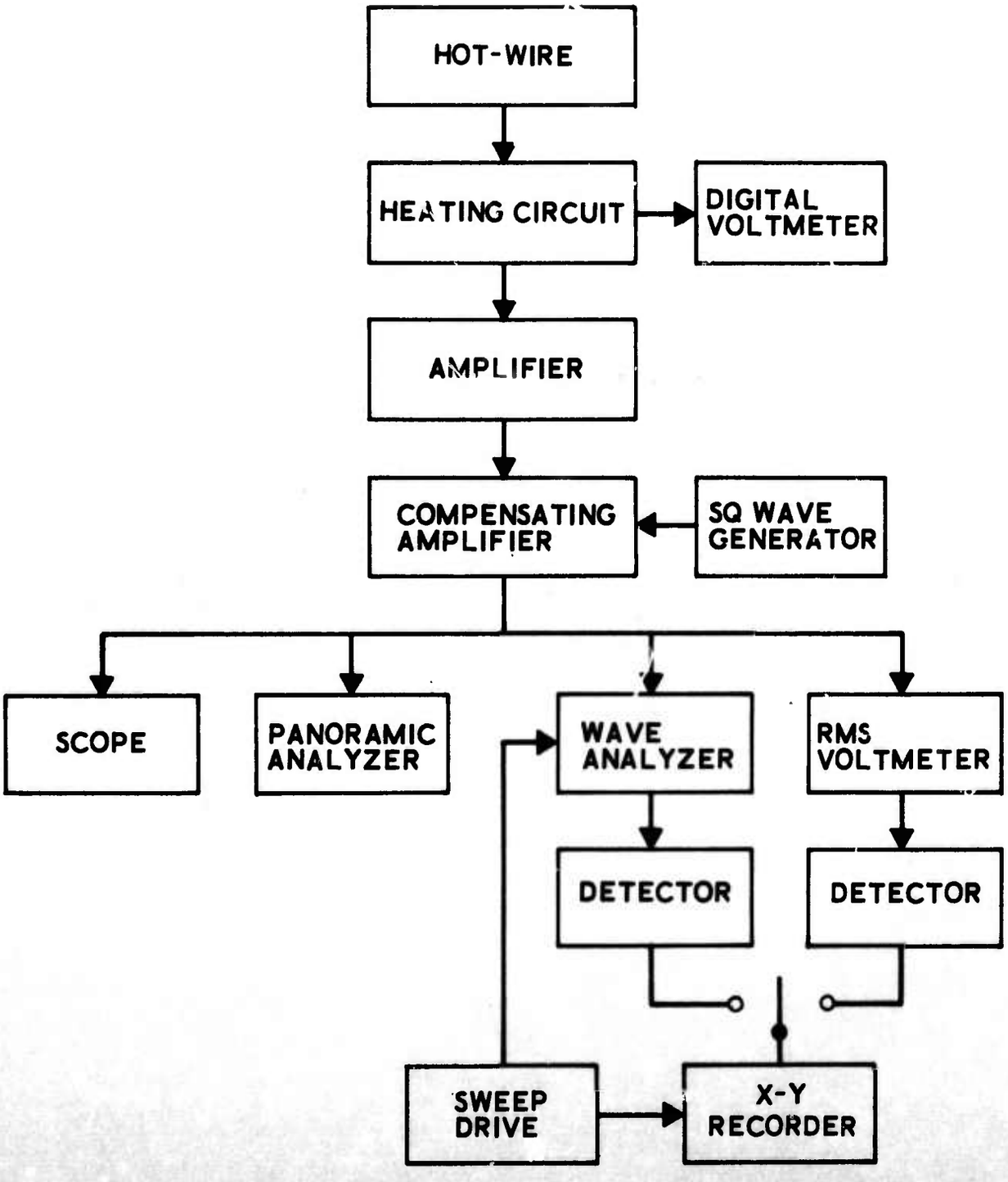

F09813 U

FIGURE 5. ELECTRONIC CIRCUIT USED FOR TURBULENCE MEASUREMENTS.

2.5 EXFERIMENTAL PROCEDURE

The measurement of the rms fluctuations of the flow variables and of their spatial correlations in the wake lies within the capability of the constant-current anemometric technique developed for compressible flows by Kovasznay, Morkovin, and their co-workers (References 14 and 15). The latter technique, bolstered by the computer-aided process of extending the wire frequency response, was used throughout this work. The measurements were performed by obtaining radial profiles of hot-wire output at 14 axial positions along the wake (designated X-Station 0 through 13) beginning at 17 model base diameters downstream of the base and spaced 0.500 inch apart. The several weeks needed to obtain the necessary data and the inevitable wire breakage* forced the use of several wires during the measurements. All data were obtained from traverses along the Z-axis.

There are two types of analyses of the hot-wire output which are of interest. By the modal analysis, we seek to break down the fluctuations received within a certain bandwidth into contributions from each flow variable (mode); e.g., the velocity or the density. The bandwidth chosen may be small, in which case the spectrum of each separate mode can be obtained, or large enough to cover the entire frequency range, in which case the frequency-integrated contribution of each mode to the total hot-wire output can be determined. In the former instance, the spectral analysis of the signal yields the relative importance of each mode at different frequencies (or wave numbers) and allows for the computation of the mode autocorrelation function and its turbulence scales. In any case, the first basic step consists of measuring the total wire output at each of at least three heating currents; knowledge of the mean-flow properties is also necessary to compute the sensitivity coefficients (Reference 14). Three equations are thus obtained and one can solve for three unknowns: the mass-flux fluctuation, $\Delta(\rho u)/\rho u$, total temperature fluctuation, $\Delta T_o/T_o$, and the cross-correlation,

*Some 0.00005-inch-diameter wires survived more than 50 hours of tunnel time; the average was closer to 20 hours.

r_{mt}, of these two fluctuations. The accuracy of this measurement can be increased if more than 3 measurements are taken and, in fact, 15 different values of heating current have been chosen in the present experiment. The highly redundant system of 15 equations was then solved by the least-squares method.

At each axial station, the wire was first placed just outside the wake, its current was fixed to the desired value, its time constant was measured by the square-wave method, and the compensating amplifier was adjusted to that value of the time constant. The wire was then traversed radially across the wake and a continuous trace of its average voltage and the frequency-integrated mean square of its fluctuating output, deriving from the maximum possible bandwidth of the system, were obtained. This procedure was repeated for each of 15 different wire currents for a total of 30 data curves at each axial station. There were 15 mean-wire voltage versus radius, such as shown in Figure 6, and 15 traces of the frequency-integrated mean-square ac component of the wire output versus radius. An example of the latter is shown in Figure 7.

If the frequency response of the wire-amplifier-compensator system were linear over the range of the flow fluctuation spectrum, the data mentioned in the above paragraph would be sufficient to resolve the signal into the frequency-integrated contributions from each turbulence mode at any desired point in the wake. However, neither the amplifier nor the compensator could attain a linear transfer function over the 500-kilocycle-per-second (kcps) range where signals were, by preliminary measurement, known to occur. In addition, because of the local Reynolds number variation in the wake, the constant-current wire underwent a change of its time constant with radius and thus a change of its own transfer function (frequency response). Because of the intense turbulence, proper compensation of the wire within the wake was not possible. Even if it were, the point-by-point adjustment of the compensator transfer function would increase the already taxing labor of fluctuation measurements well beyond practical proportions. It is

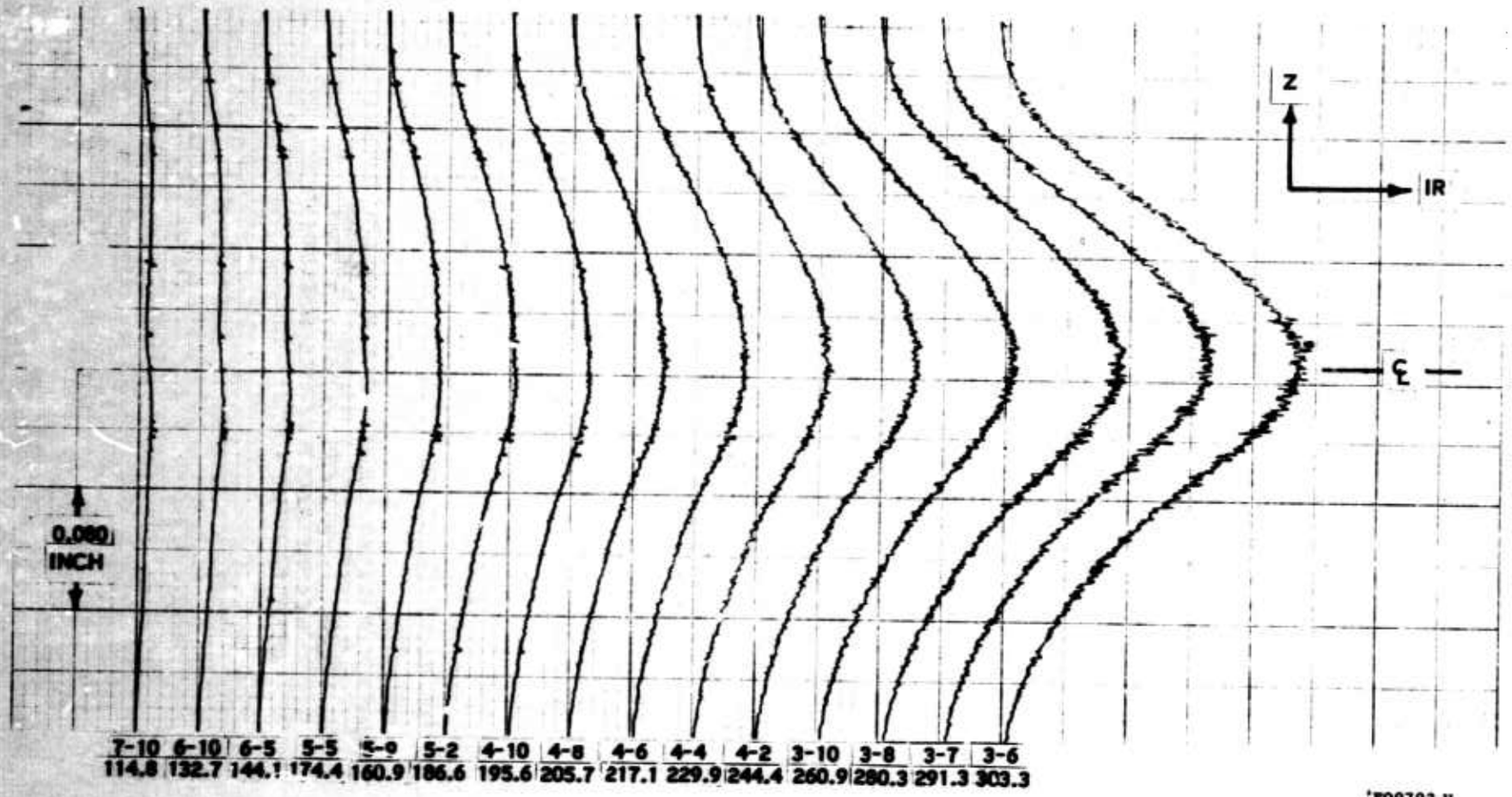

F09793 U

FIGURE 15. MEAN HOT-WIRE PROFILES (WIRE VOLTAGE VS. RADIUS) AT DIFFERENT CURRENTS REPRODUCED DIRECTLY FROM THE X-Y PLOTTER TO SHOW WAKE RADIAL SYMMETRY.

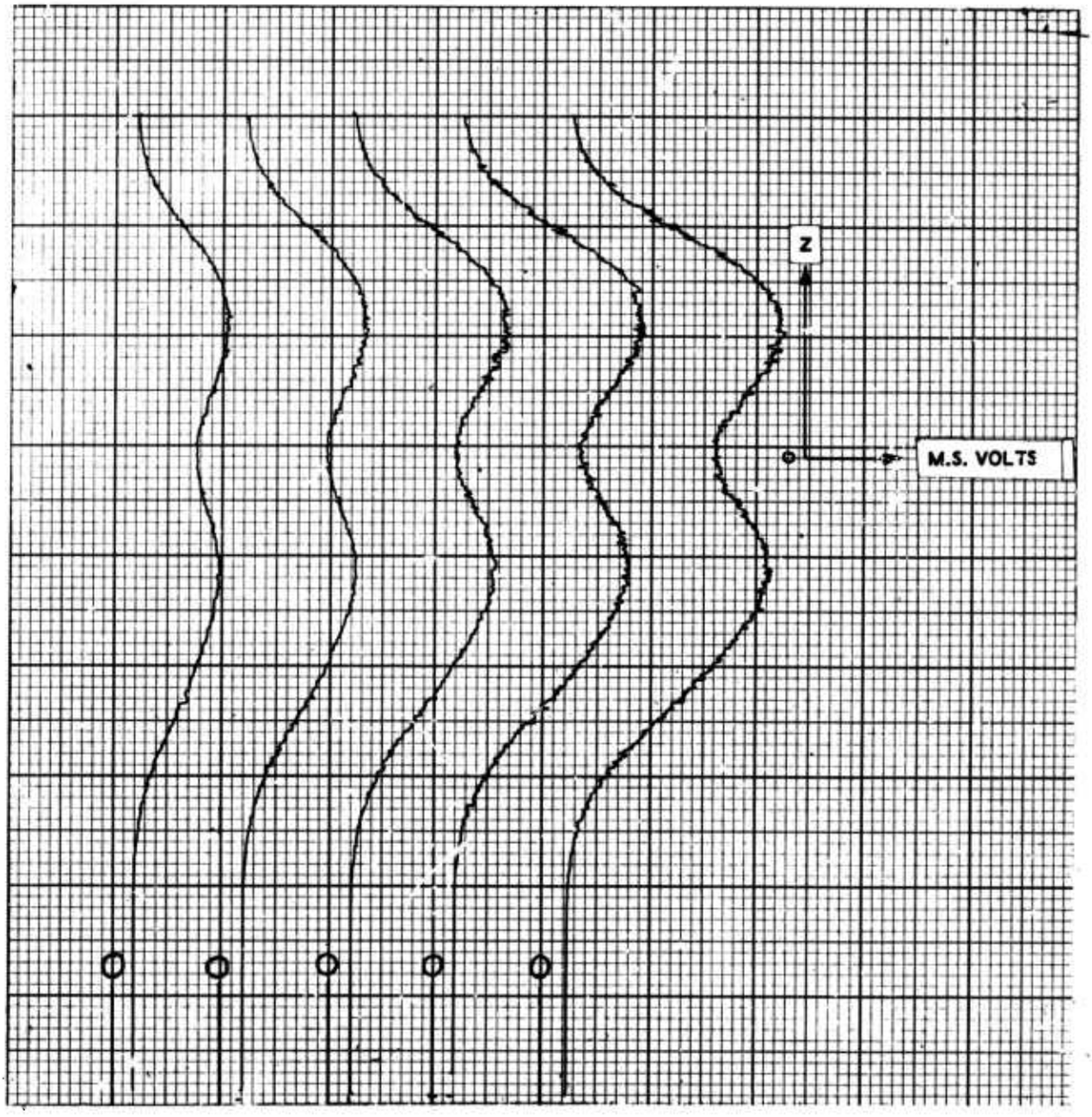

F09814U

FIGURE 7. TYPICAL RAW TURBULENCE DATA AS REPRODUCED DIRECTLY FROM X-Y PLOTTER. ORDINATE IS WAKE RADIUS; ABSCISSA IS INTEGRATED OUTPUT. EACH CURVE CORRESPONDS TO DIFFERENT WIRE CURRENT (SENSITIVITY). NOTE SYMMETRY.

therefore clear that some of the signals contained in the turbulent fluid, (i.e., those at the higher frequencies), were missing from the 15 traverses previously mentioned.

To overcome this difficulty, the following principle was invoked: the amount by which an imperfect mechanical system distorts (e.g., attenuates) an input signal can be found by measuring the transfer function (i.e., the frequency response) of the system itself and of its output. Thus, the output spectra of the wire at each axial position were recorded for a number of currents and radial positions*. The results were combined with the known overall transfer function of the wire-amplifier-compensator system to yield the ideal frequency-integrated mean square voltage output, e^{*2}, of the wire as a function of axial and radial coordinates x and y

$$\frac{e^{*2}(x,y)}{e^2(x,y)} = \frac{\int_o^{f_x} V^2(f)\, \frac{W^2}{C^2}\, \frac{G_o^2}{G^2}\, d\left(\frac{f}{f_B}\right)}{\int_o^{f_x} V^2(f)\, d\left(\frac{f}{f_B}\right)} \equiv J(x, y, I) \qquad (1)$$

where e^2 is the recorded mean square output, $W_o^2 G_o^2 / C^2 G^2$ the overall transfer function, $V^2(f)$ the wave analyzer output at each frequency, and f and f_B are the 1-kilocycle-per-second analyzer bandwidth. The error ratio, J, thus obtained was then applied to the mean square output from the constant-current traverses of the type shown in Figure 7 to correct for the nonlinear response of the system. A separate computer program was set up to bring about this response restoration effect; this is the WEB-II program (See Appendix B). Figure 9 shows the variation of the wire time constant and error ratio across the wake 17 diameters downstream of the base. Interestingly, J approaches a limit independent of wire current as the latter

*This was done for each of 8 currents and at 10 radial positions for a total of 80 spectra at each axial station. Combined with the mean and turbulence measurements, a total of 115 traces were necessary at each axial station. An example of such spectra is shown in Figure 8.

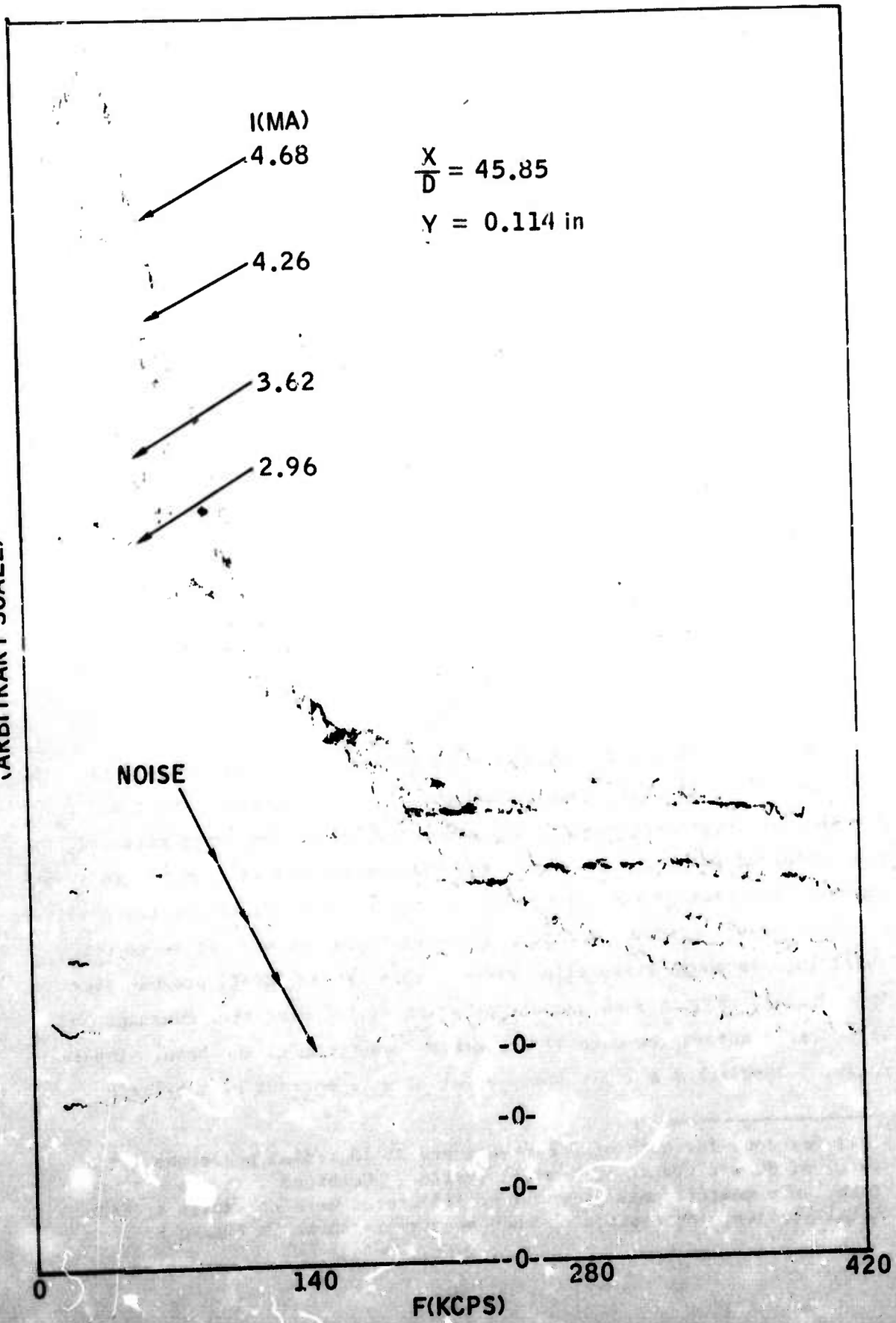

FIGURE 8. TYPICAL SPECTRAL OUTPUTS OF HOT-WIRE IN THE WAKE.

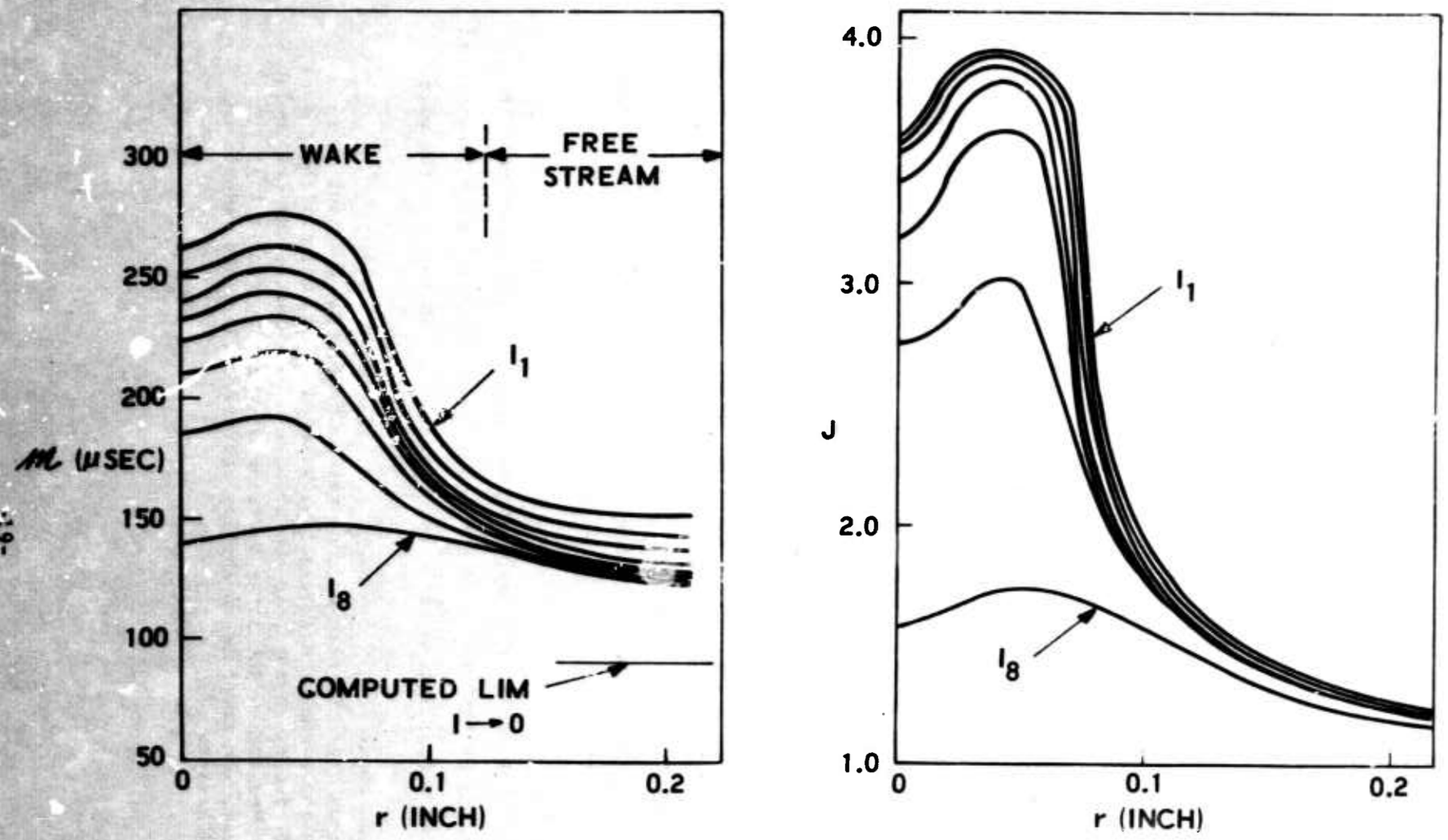

F09815 U

FIGURE 9. MEASURED VARIATION OF WIRE TIME CONSTANT (LEFT) AND ERROR RATIO (RIGHT) ACROSS THE WAKE FOR CURRENTS VARYING FROM 6.425 MD TO 2.976 MD. CONDITIONS ARE X/D = 17, WIRE 3-4/2.

increases.* It should be noted that the time constant, M, inside the wake was computed, for each current, by

$$M = M_I \left[\frac{R_I}{(\partial R/\partial I)_I} \quad \frac{(\partial R/\partial I)}{R} \right] \tag{2}$$

where M_I is the time constant measured at the wake edge, I is the current, and R is the wire resistance. In this way, reliance on a theoretical calculation of M is largely circumvented and only the dependence of M on overheat and Reynolds number is retained (see Appendix A). A final point concerning the role of the error ratio, i.e., the need for the response restoration procedure, is shown in Figure 10. We see that, in the region investigated, J decreases towards the far wake but remains higher than unity. Corrections were thus necessary even at about 100 diameters downstream.

The procedure described above was necessary to give correct results for the modal analysis of the data, that is, correct values of the frequency-integrated but modally resolved fluctuations from point to point. The computer program set up to handle the above "response restoration" of the anemometer system (see Appendix B) also supplies the fluctuation spectrum (i.e., the true distribution of the flow disturbances with frequency corrected for any shortcomings of the instrumentation) at each axial position for each of 10 radial locations and, at each of the latter, at each of 8 heating currents. The output of spectra listed in WEB-II (Appendix B), thus formed the basis of the spectral analysis wherein the spectral density of the temperature (density) and axial velocity fluctuation and of the cross-correlation could be resolved at each point in the wake.

---

*Figure 9 shows that the zero-current value of the time constant in the free-stream approaches the theoretical value of about 0.1 millisecond by which the frequency response to 800 kilocycles per second was originally estimated. Because of the large increase of the time constant in the wake, however, the response capability decreases there and results in the large J's measured.

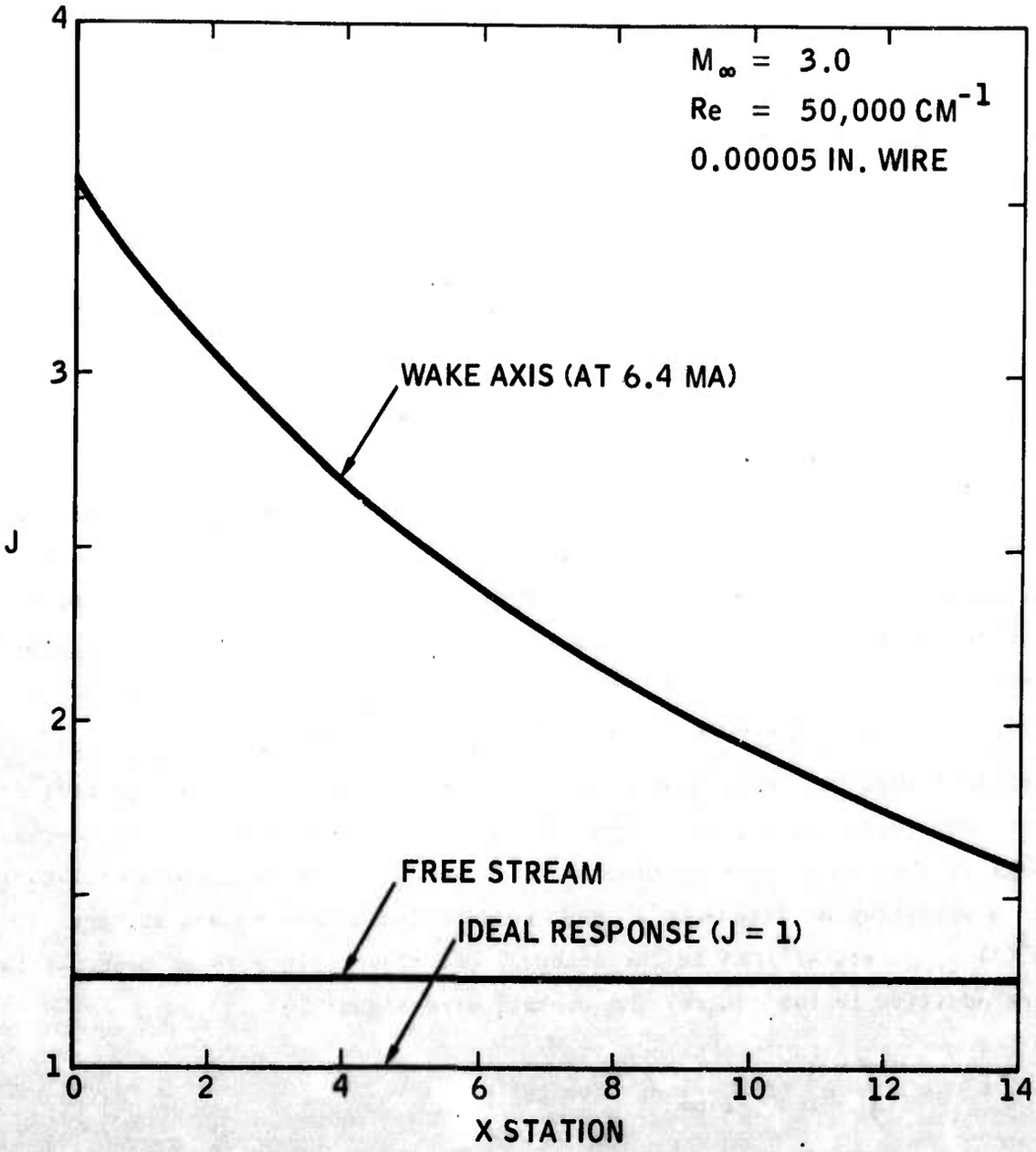

FIGURE 10. ERROR-RATIO VARIATION IN THE AXIAL DIRECTION AT THE HICHEST WIRE CURRENT USED.

The essential point here, hitherto not appreciated, is that at the present state of the art, spectral measurements are mandatory whether or not a spectral analysis of the data is intended.

2.6 DATA REDUCTION AND PROCESSING

2.6.1 SIGNAL PROCESSING

It is now necessary to describe how the data as obtained above were processed through the electronic equipment shown in Figure 5. This description utilizes the principles rather than the exact characteristics of the electronic components used in this experiment (the latter being given in Appendix A) so as to be of value to others engaged in similar work.

For a fixed current, the sensible real input to the measuring system of a constant-current anemometer is a voltage fluctuation into the wire. Between the latter and the recording device, the signal proceeds through the elements of the block diagram of Figure 5 and is thus affected by the transfer functions of these elements. Generally, these transfer functions execute selective filtering or amplification, squaring, averaging, integrating, and so on. Because these functions are often unobtainable from the manufacturer, they were measured carefully prior to this work, a procedure necessary to increase accuracy and, as shown in the preceding section, to make the work possible in the first place.

Consider that the continuous Fourier spectrum of the flow into the wire (or, otherwise stated, the output of the wire if the latter had no thermal lag) is the sum of contributions of a large number of discrete oscillators, each vibrating at frequency f, and contributing a mean square voltage $e^2(f)_{flow}$ $(volts)^2/cps$ in the interval Δf. Then, since these contributions are additive in the square, the overall wire signal is

$$E^2 = \int_0^{\infty} e^2(f)_{flow}\, df \quad (volts)^2 \qquad (3)$$

Because of the well-known thermal lag phenomenon (Reference 11), the actual mean square wire output $e^2(f)_{wire}$ will be lower than $e^2(f)_{flow}$, and the transfer function W(f) of the wire is then defined by

$$W(f) = \frac{e(f)_{flow}}{e(f)_{wire}} \geq 1 \qquad (4)$$

The signal is now inserted in an ac amplifier with transfer function G(f) which can be split into a frequency-independent zero-frequency gain, G_o, and the amplifier drop-off characteristics $G/G_o(f)$; the amplifier output, $e(f)_{amp}$, can then be defined by

$$G(f) = \frac{e(f)_{amp}}{e(f)_{wire}} = \frac{G}{G_o}(f)\, G_o \leq G_o \qquad (5)$$

The signal next proceeds to the compensating amplifier which has usually a zero-frequency gain of unity, a transfer function, C(f), and an output, $e(f)_{comp}$, such that

$$C(f) = \frac{e(f)_{comp}}{e(f)_{amp}} \qquad (6)$$

Note that C(f) is also a strong function of the compensator time-constant setting and that it generally rises well above unity to some maximum and thereafter decays.

If Equations (4), (5), and (6) are combined, the mean square voltage compensator output for a specific flow input, $e^2(f)_{flow}$, in the passband Δf around the frequency, f, is given by

$$e^2(f)_{comp}\,\Delta f = \frac{C^2(f)\,G^2(f)}{W^2(f)}\, e^2(f)_{flow}\,\Delta f \quad (volts)^2 \qquad (7)$$

It should be noted that the quantity CG is a given function of frequency for a given setting of the electronics. The quantity CG/W, on the other hand, which is equivalent to the overall transfer function (OTF) is additionally a function of the wire time constant and thus a function of the

wire and flow characteristics, changing from current to current and from point to point in the wake; however, it is insensitive to the magnitude of $e^2(f)_{flow}$ within broad limits. The OTF was provided, as a function of frequency at each wire current and point in the wake, by the output of the WEB-II program, and a typical plot is shown in Figure 11. Note that the system response deteriorates, although not greatly, as the frequency increases.

There are two alternatives to further processing of the data. For spectral analysis, one uses a wave analyzer with constant-bandwidth, f_B cps; in this case, the analyzer also incorporated a detector with transfer function, H, such that

$$V^2(f) = H^2 \left[e^2(f)_{comp} \, f_B \right] \quad (volts)^2 \quad (dc) \tag{8}$$

and thus

$$e^2(f)_{flow} = \frac{W^2}{C^2 G^2} \, \frac{V^2}{H^2 f_B} \quad (volts)^2 \quad (mean\ square) \tag{9}$$

The integrated fluctuations obtain when a wideband rms voltmeter obtains the sum of the compensator output

$$e^2_{VTVM} = \int_o^{\infty} e^2(f)_{comp} \, df \quad (volts)^2 \quad (mean\ square) \tag{10}$$

and thus

$$e^2_{VTVM} = \int_o^{\infty} \frac{C^2 G^2}{W^2} \, e^2(f)_{flow} \, df \quad (volts)^2 \quad (mean\ square) \tag{11}$$

This voltmeter also has a detector of transfer function A which converts the mean square fluctuating voltage into a dc voltage E' such that

$$E' = A \, e^2_{VTVM} \ volts\ (dc) \tag{12}$$

for use with the X-Y recorder.

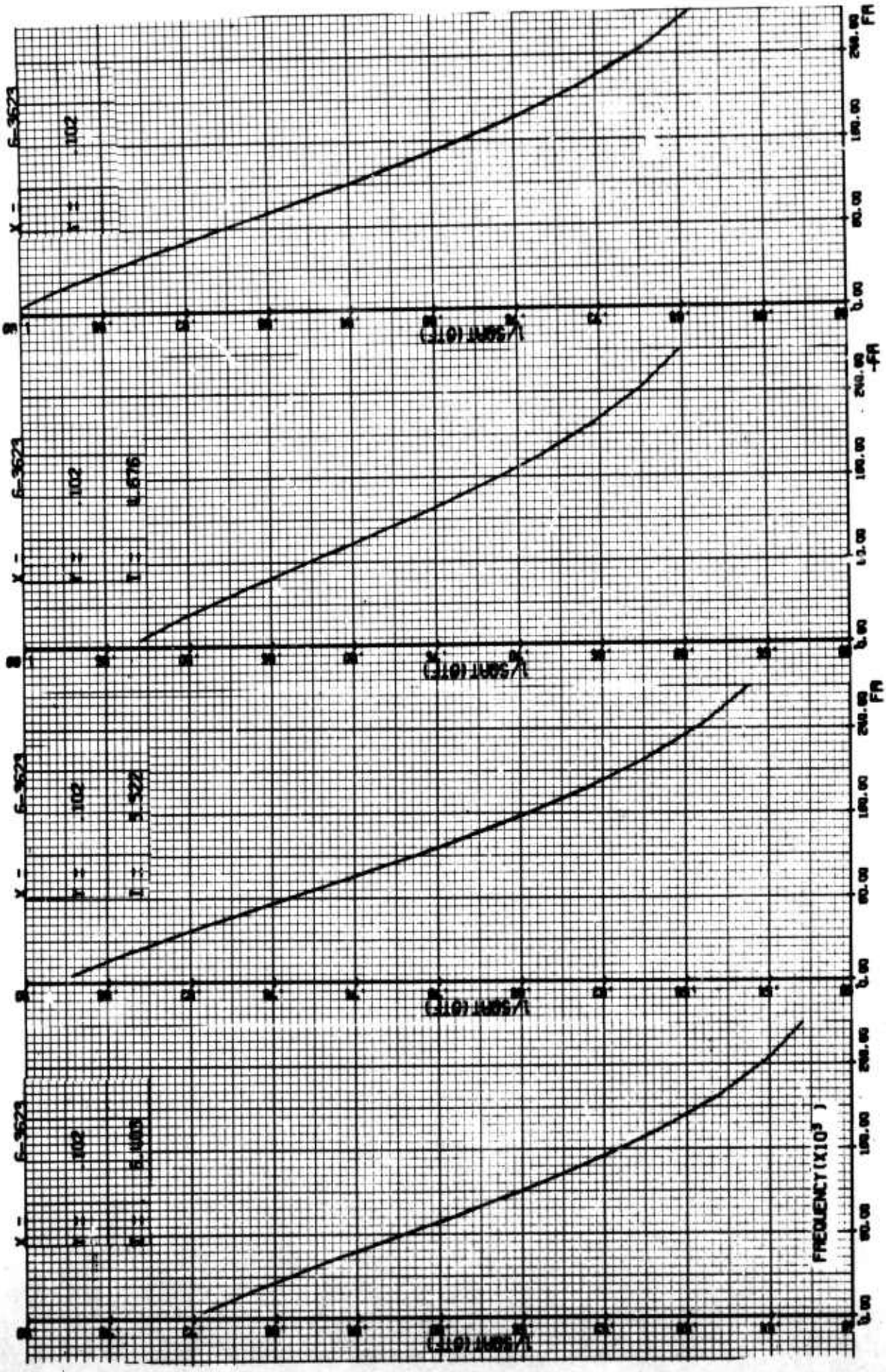

FIGURE 11. TYPICAL VARIATION WITH FREQUENCY OF THE OVERALL TRANSFER FUNCTIONS AT A POINT IN THE WAKE. NOTE IMPROVEMENT IN RESPONSE AS THE WIRE CURRENT I IS LOWERED.

When both the spectrum and the integrated measurements are performed, we have available a cross-check of the experiment since, by relating Equations (9), (11), and (12) we can write

$$\frac{E'}{A} = e^2_{VTVM} = \int_o \frac{C^2 G^2}{W^2} e^2(f)_{flow} \, df = \int_o \frac{V^2(f)}{H^2} \, d\left(\frac{f}{f_B}\right) \quad (13)$$

This check was performed at each measuring point with the aid of computer program WEB-II and gave satisfactory results, as can be seen in Figure 12.

Returning now to Equation (11), we rewrite it as

$$e^2_{VTVM} = G_o^2 \int_o \frac{G^2}{G_o^2} \frac{C^2}{W^2} e^2(f)_{flow} \, df \quad (14)$$

For an ideal amplifier (flat to infinite frequency), G/G_o is unity; C is supposed to have a characteristic exactly inverse to W below some frequency at which it peaks, and if $e^2(f)_{flow} = 0$ beyond that point, then C/W is also unity over the spectrum. In this case, the ideal mean square voltage

$$e^{*2}_{VTVM} = G_o^2 \int_o e^2(f)_{flow} \, df \quad (volts)^2 \quad (15)$$

is obtained, and thus the error ratio, J, is computed as explained in paragraph 2.5.

$$J \equiv \frac{e^{*2}_{VTVM}}{e^2_{VTVM}} = \frac{\int_o \frac{V^2(f)}{H^2} \frac{W^2}{C^2} \frac{G_o^2}{G^2} \, d\left(\frac{f}{f_B}\right)}{\int_o \frac{V^2(f)}{H^2} \, d\left(\frac{f}{f_B}\right)} \quad (16)$$

Note that, as explained previously, J = 1 for an ideal electromechanical system (W/C = 1, G/G_o = 1), and also that J can be obtained accurately if H and f_B are unknown but still independent of frequency.

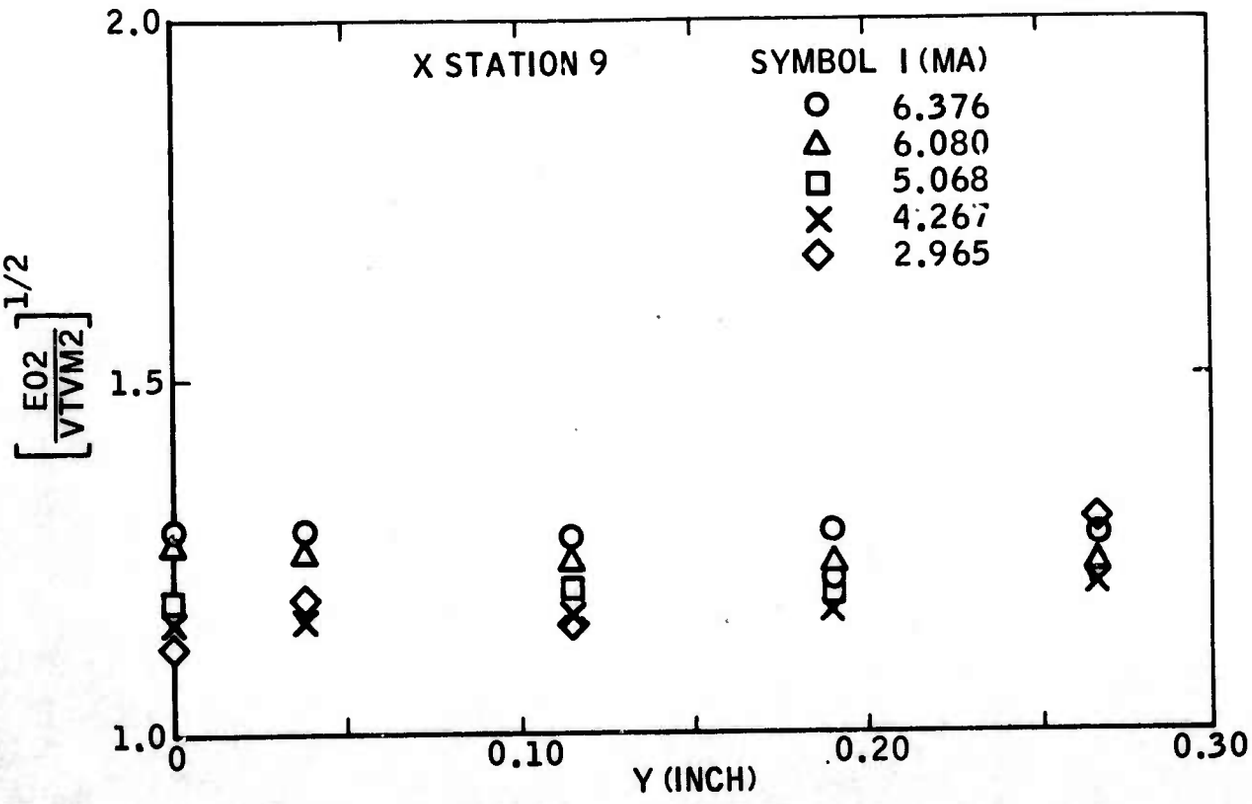

FIGURE 12. TYPICAL AGREEMENT BETWEEN MODALLY UNRESOLVED RMS SQUARE OUTPUT AS OBTAINED BY A VOLTMETER (VTVM2) AND AS RECONSTRUCTED FROM THE SPECTRUM (E02), FOR DIFFERENT CURRENTS.

A last point concerns the subtraction of electronic noise from the measurement. When the wire heating current is turned off, the rms voltmeter reads a noise level (e_{VTVM}) noise, whereas with the current turned back on, a reading (e_{VTVM}) meas is obtained. Because the turbulence and electronic noise are uncorrelated, one obtains

$$e^2_{VTVM} = \left(e^2_{VTVM}\right)_{meas} - \left(e^2_{VTVM}\right)_{noise} \tag{17}$$

for use with the previous formulas. A similar correction is necessary in the spectral measurement. If V_m (f) is the analyzer detector output (in volts) and V_n (f) is the corresponding noise at frequency f, then

$$\left(\frac{V}{H}\right)^2 = \left(\frac{V_m}{H}\right)^2 - \left(\frac{V_n}{H}\right)^2 \tag{18}$$

is the corrected reading (in volts squared) at that frequency.

Knowledge of the wire Reynolds number Re_o cause from the diagnosis of the mean properties of the wave, described in Reference 12. The modal analysis into the rms normalized mass-flux and total temperature fluctuations and their correlation

$$m \equiv \left[\frac{\Delta(\rho u)}{\rho u}\right]_{rms} \tag{25}$$

$$t \equiv \left(\frac{\Delta T_o}{T_o}\right)_{rms} \tag{26}$$

$$r_{mt} \equiv \overline{\left[\frac{\Delta(\rho u)}{\rho u}\right]\left(\frac{\Delta T_o}{T_o}\right)} \Big/ \left[\frac{\Delta(\rho u)}{\rho u}\right]_{rms}\left(\frac{\Delta T_o}{T_o}\right)_{rms} \tag{27}$$

was then made by the simultaneous solution for the 3 unknowns of 15 equations of the type*

$$\frac{e^{*2}}{G_o^2\,\bar{e}^2} = e_m^2\, m^2 + e_t^2\, t^2 - 2\, m t r_{mt}\, e_m\, e_t \tag{28}$$

where $(e^{*2}/G_o^2\,\bar{e}^2)$ is the normalized voltage fluctuation adjusted for the zero-frequency amplifier gain, G_o. (The bandwidth of these modal measurements was in each case sufficient to include sensible signals at all frequencies.) Here e* (volts) refers to the ideal frequency-integrated mean-square wire output at each particular value of the heating current

$$e^2 = G_o^2 \int_o^\infty e^2(f)_{flow}\, d_f \ (volts)^2 \tag{29}$$

Note the similarity with Equations (3) and (15), which say that

$$e^{*2} \equiv e^{*2}_{VTVM} \equiv E^2\, G_o^2 \tag{30}$$

* Following past practice, the unknowns are obtained by the computer from the shape parameters of the second-degree curve fitted to the 15 experimental points. (See Appendix D.)

2.6.2 MODAL ANALYSIS

Once supplied with a method for alleviating the response shortcomings of the system, the turbulence data (i.e., those described by the 15 traverses mentioned earlier) could be reduced. The sensitivity coefficients e_m and e_t to mass flux and total temperature fluctuations, respectively, were computed by the following slightly modified form of Morkovin's (Reference 14) formulas

$$e_m = e_f \left[A_w' \frac{Re_o}{Nu_o} \frac{\partial Nu_o}{\partial Re_o} - \frac{A_w'}{\tau_{wr}} \frac{Re_o}{\eta} \frac{\partial \eta}{\partial Re_o} \right] \tag{19}$$

$$e_t = c_f \left[K + A_w' \left(K + 0.765 \frac{Re_o}{Nu_o} \frac{\partial Nu_o}{\partial Re_o} - 1.885 \right) - 0.765 \frac{A_w'}{\tau_{wr}} \frac{Re_o}{\eta} \frac{\partial \eta}{Re_o} \right] \tag{20}$$

where c_f accounts for the circuit impedance, τ_{wr} and K are related to the resistance-temperature slope, and A_w' is Morkovin's overheat parameter

$$A_w' = \frac{1}{2} \frac{I}{R} \frac{\partial R}{\partial I} \tag{21}$$

associated with the wire resistance R change with current, I, which could be directly obtained from the traverses of Figure 6. For the type of hot wires employed (Reference 12), the zero-current Nusselt Number Nu_o based on the stagnation conductivity is given by

$$Nu_o = 0.04186\ Re_o + 0.1803 \sqrt{Re_o} + 0.1078 \tag{22}$$

whence

$$\frac{\partial Nu_o}{\partial Re_o} = 0.04186 + \frac{0.0902}{\sqrt{Re_o}} \tag{23}$$

Similarly

$$\eta = 0.99 + \frac{0.05661}{Re_o^{2.174}} \tag{24}$$

Alternatively, a more revealing and practically important modal split decomposes the signal into vorticity (velocity), entropy, and sound fluctuations (Reference 14 and 15). It is significant that both Kovasznay (Reference 15) and Kistler (Reference 17) have confirmed the relative unimportance of the sound mode inside compressible turbulent shear flows, compared to the vorticity and entropy modes. The data of the present experiment were thus further reduced on the assumption that there were no sound fluctuations inside the turbulent wake. At each point in the wake, another 15 equations are obtained of the type

$$\frac{e^{*2}}{G_o^2 \overline{e}^2} = e_\tau^2 \tau^2 + e_\sigma^2 \sigma^2 + 2\, e_\tau\, e_\sigma\, r_{\sigma\tau}\, \tau\sigma \tag{31}$$

where the vorticity fluctuation

$$\tau \equiv \left(\frac{\Delta u}{u}\right)_{rms} \tag{32}$$

and the entropy fluctuation

$$\sigma \equiv \left(\frac{\Delta T}{T}\right)_{rms} = \left(\frac{\Delta \rho}{\rho}\right)_{rms} \tag{33}$$

and, of course

$$r_{\sigma\tau} = \frac{\overline{\left(\frac{\Delta u}{u}\right)\left(\frac{\Delta T}{T}\right)}}{\left(\frac{\Delta u}{u}\right)_{rms}\left(\frac{\Delta T}{T}\right)_{rms}} = -\frac{\overline{\left(\frac{\Delta u}{u}\right)\left(\frac{\Delta \rho}{\rho}\right)}}{\left(\frac{\Delta u}{u}\right)_{rms}\left(\frac{\Delta \rho}{\rho}\right)_{rms}} \tag{34}$$

The coeffocients e_τ and e_σ of wire sensitivity to vorticity and entropy fluctuations, respectively, have been derived by Morkovin in terms of the corresponding coefficients e_m and e_τ given by Equations (19) and (20)

$$e_\tau = e_m + \alpha e_\tau \tag{35}$$

$$e_\sigma = \beta e_\tau - e_m \tag{36}$$

* Following past practice, the unknowns are obtained by the computer from the shape parameters of the second-degree curve fitted to the 15 experimental points. (See Appendix D.)

where α and β are functions of the specific heat ratio γ and the Mach number M

$$\alpha \equiv \left[1 + \frac{\gamma-1}{2} M^2\right]^{-1} \tag{37}$$

$$\beta \equiv \alpha (\gamma-1) M^2 \tag{38}$$

Again, the curve-fitting process was used to solve the redundant system of 15 equations, such as (31), for τ, σ, and the correlation $r_{\sigma\tau}$.

It is of interest to look at the variation of wire sensitivity to the different modes with heating current, as shown in Figure 13. The outstanding feature is the existence of values of the heating current for which the sensitivity e_τ to vorticity vanishes, as was mentioned in Paragraph 2.5. This important fact, first recognized by Kovasznay (Reference 15), implies that in the absence of sound the density fluctuations alone can be measured directly and quite simply if one knows the wire characteristics and local flow properties precisely; in the present instance, this circumstance was utilized to provide very satisfactory cross-checks of the entropy fluctuation results. It was also used for studying the intermittent nature of the density profile of the wake.

2.6.3 SPECTRAL ANALYSIS

As mentioned, the aim of Spectral analysis (or, more precisely, modal-spectral analysis) is to show the spectral distributions of each mode of fluctuation. The key to this analysis is that the equation of modal resolution, Equation (31), is independent of bandwidth. Because the fluctuations are constant with frequency f to good approximation within the 1-kilocycle-per-second bandwidth used, we can write the modal equation

$$\frac{e^{*2}(f)}{G_o^2} = e_\tau^2 \tau^2(f) + e_\sigma^2 \sigma^2(f) + 2 e_\tau e_\sigma r_{\sigma\tau}(f)\sigma(f)\tau(f) \tag{39}$$

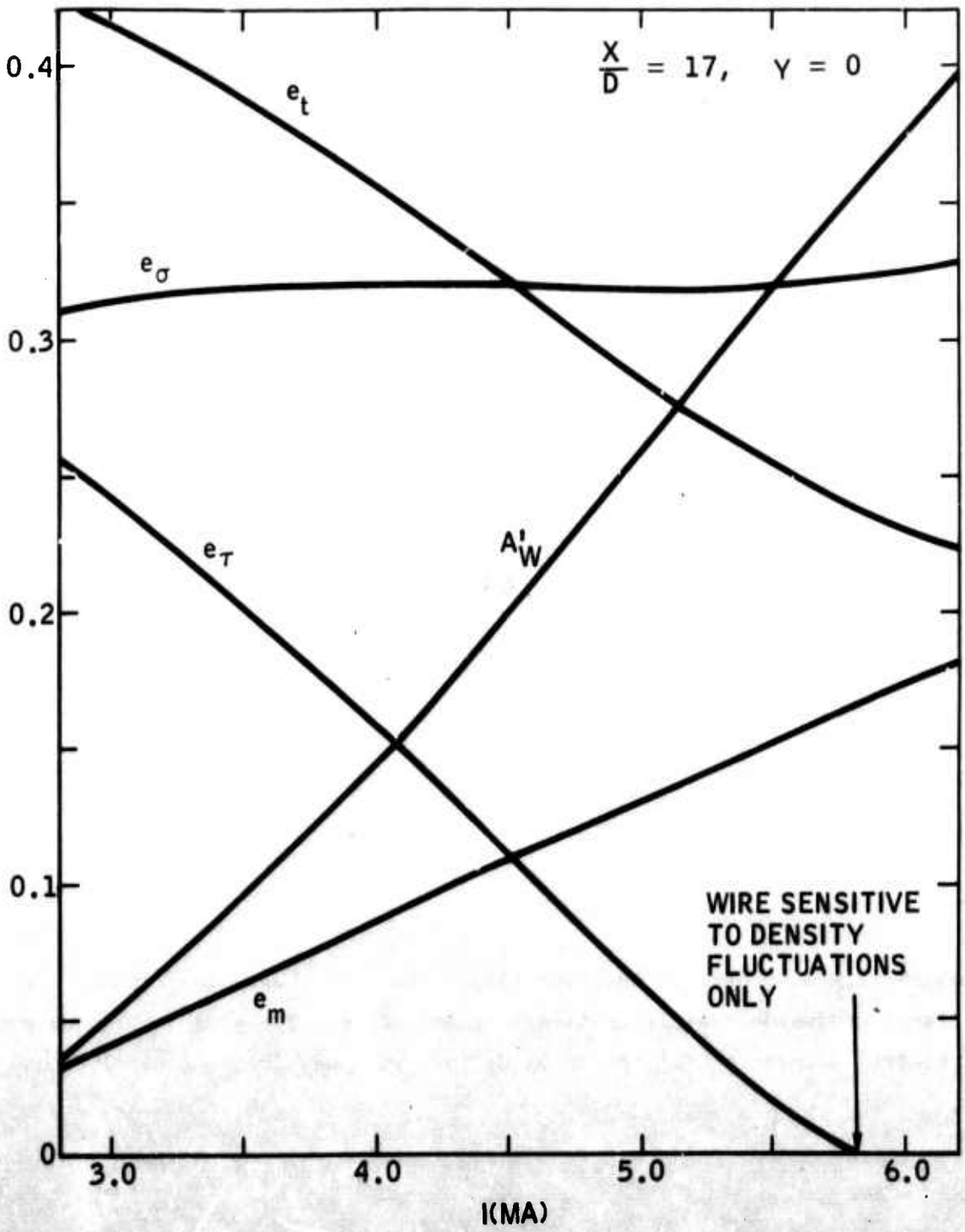

FIGURE 13. VARIATION OF THE WIRE SENSITIVITY COEFFICIENTS AND OVERHEATING PARAMETER A'_W WITH WIRE CURRENT AT A TYPICAL POINT IN THE WAKE.

at each frequence f, where $e^{*2}(f)/\bar{e}^2$ is the nondimensional mean-square output per kilocycle. The sensitivity coefficients retain their previous values.

By way of clarification, note that when the sum of signals in all adjoining passbands is taken and the result integrated over frequency, Equation (39) gives

$$\frac{1}{G_o^2\,\bar{e}^2}\int_o^\infty e^{*2}(f)df = e_\tau^2\int_o^\infty \tau^2(f)df + e_\sigma^2\int_o^\infty \sigma^2(f)df + 2\,e_\sigma\,e_\tau\int_o^\infty r_{\sigma\tau}(f)\sigma(f)\tau(f)df \tag{40}$$

so that

$$\int_o^\infty e^{*2}(f)df = e^{*2} \tag{41}$$

$$\int_o^\infty \sigma^2(f)df = \sigma^2 \tag{42}$$

$$\int_o^\infty \tau^2(f)df = \tau^2 \tag{43}$$

$$\int_o^\infty r_{\sigma\tau}(f)\sigma(f)\tau(f)df = r_{\sigma\tau}\,\sigma\,\tau \tag{44}$$

which brings us back to Equation (31). The latter equations should also dispel confusion regarding dimensions and units. For example, the output spectral deunity $e^{*2}(f)$ should be defined in a way (e.g., $(\text{volts})^2/\text{kcps}$)

consistent with the integrating interval df (e.g., kilocycles per second. If the quantities $\tau(f)/\tau$ and $\sigma(f)/\sigma$ are defined as the velocity (vorticity) and density (entropy) spectral densities, the spectra are normalized to unity; that is

$$\frac{1}{\tau^2}\int_0^\infty \tau^2(f)df = 1 \tag{45}$$

$$\frac{1}{\sigma^2}\int_0^\infty \sigma^2(f)df = 1 \tag{46}$$

The spectra can next be normalized by the characteristic frequency of the turbulent flow, which is u/Λ_i, where u is the local flow velocity and Λ_i is the integral scale appropriate to the quantity i (Λ_s is the entropy scale, Λ_T the vorticity scale) which is derivable from the Eulerian time integral scale for the single wire; the latter is connected with the spectrum (Reference 18) so that

$$\lim_{f\to o}\frac{\tau^2(f)}{\tau^2} = \frac{4\Lambda_T}{u} \equiv \frac{\tau^2(0)}{\tau^2} \tag{47}$$

$$\lim_{f\to o}\frac{\sigma^2(f)}{\sigma^2} = \frac{4\Lambda_S}{u} \equiv \frac{\sigma^2(0)}{\sigma^2} \tag{48}$$

SECTION 3

PRELIMINARY OBSERVATIONS

3.1 THE EXTERNAL TURBULENCE FIELD

The amount of free-stream (ambient) turbulence in the wind tunnel was measured prior to the study of the fluctuations in the wake. The stream turbulence is often a critical factor in that it can add to the noise of the electronic equipment in obscuring the turbulence level in the wake itself. Initial measurements without the model in place showed rather large fluctuations, on the order of 1 percent in the mass flow and 0.3 percent in the total temperature. Measurements performed later with the model in place and with the computerized data reduction process described in the previous paragraphs disclosed the above computations to be larger than the actual turbulence level by a factor of about 3. At no time was the stream turbulence level a serious obstacle to the fluctuations in the wake, including the points of observation farthest downstream.

3.2 OBSERVATIONS ON THE TRANSITION PROCESS

Although this work was not aimed at investigating the events in the laminar wake leading up to transition to turbulence, some interesting phenomena were detected in the laminar and pretransitional flow. Briefly, a sharp energy concentration at about 20 kilocycles per second was observed to

occur in the laminar wake, with the rest of the spectrum completely devoid of fluctuations. As the wire approached the transition zone, the energy prominence first increased in magnitude and then rapidly began to feed energy into the higher frequencies. Further downstream, the peak decayed so that a completely random spectrum remained in the turbulent wake. This result was obtained both by first keeping the wire stationary and moving the transition forward toward the probe by increasing the tunnel pressure, and also by keeping the flow fixed and moving the wire downstream in the laminar wake toward the transition zone. It was also obtained with different wires. These facts, added to the care exercised to recognize and reject extraneous signals, strongly suggest that the phenomenon is real and is further associated with the transition process. The intriguing possibility of finding a connection between laminar instability and transition to turbulence suggests that further exploration of this phenomenon is needed. These observations are pictured in Figure 14.

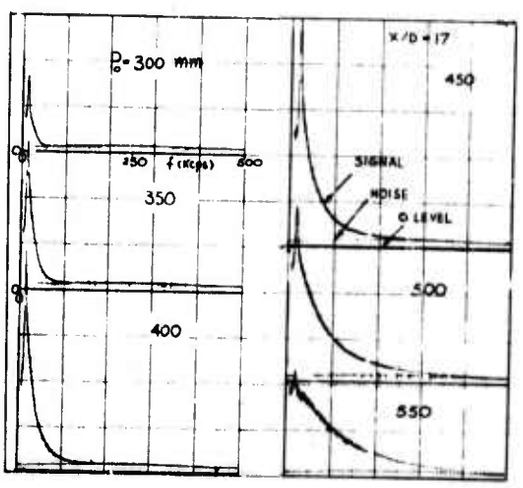

F09853 U

FIGURE 14. UNPROCESSED HOT-WIRE SPECTRA TAKEN AT A FIXED LOCATION IN THE WAKE FOR DIFFERENT TUNNEL STAGNATION PRESSURES SHOWING THE ONSET, INCREASE AND "SPECTRAL SPREADING" OF L AMINAR INSTABILITY.

SECTION 4

SIMILARITY CONSIDERATIONS

We shall preface the description of the experimental results by outlining current empirical predictions of the distribution of turbulence properties in the wake. Our chief premise is that, following a certain relaxation period, the turbulence properties may soon adjust to a self-preserving (similar) form connected simply with the local mean properties. If it exists, this similarity behavior should be closely connected with the behavior of incompressible turbulent flows. By providing experimental proof of a more general rule, insensitive to compressibility effects, we have a good chance of extending our present results to cover the dynamics of wake flows at very high Mach numbers.

The dynamic equilibrium hypothesis (DEH), discoursed at length by Townsend (Reference 1), prescribes that the large eddies maintain a dynamical balance between the extremities of turbulent shear zones in a way that simply relates the fluctuations and the mean properties. These ideas, formulated in context with incompressible flows, have been recently extended to compressible turbulent flows by Morkovin (Reference 10) and Laufer (Reference 11). Morkovin observed that, with appropriate scaling, the turbulent energy distribution in shear flows is insensitive to geometry

and Mach number. Extended to the compressible turbulent wake by Laufer, and restricted to adiabatic flows, this observation has the following implications:

(1) There are no fluctuations in the flow total temperature

$$\Delta T_o = o \tag{49}$$

(2) In consequence, the entropy (density) and vorticity (velocity) fluctuations are related through the local Mach number, M

$$\frac{(\Delta\rho/\rho)_{rms}}{(\Delta u/u)_{rms}} = (\gamma - 1)\, M^2 \tag{50}$$

(3) The temperature and velocity fluctuations are perfectly anti-correlated

$$r_{\sigma\tau} = -1 \tag{51}$$

(4) The nondimensional turbulent energy is a universal function g of a properly transformed transverse coordinate η

$$\rho\,(\Delta u)^2 = \rho'\, U^2\, g(\eta) \tag{52}$$

where ρ' and U are appropriate density and velocity scales, respectively.

4.1 VELOCITY FLUCTUATIONS

We can now write certain consequences of the dynamic equilibrium hypothesis arising from Equation (52). As Laufer (Reference 11) pointed out, a more-general form of Equation (52) is

$$\rho\,(\Delta u)^2\, Y^m = \rho'\, U^2\, \overline{Y}^m\, g(\eta) \tag{53}$$

where m = 0 or 1 for planar or axi-symmetric geometries, respectively, and where the quantity ΔQ stands for the root-mean-square (dimensional) fluctuation of the quantity Q. Here Y is a transformed radial coordinate which might be of the type

$$\bar{Y}^2 = 2 \int_o^r \frac{\rho}{\rho_\infty} Y \, dr \tag{54}$$

We immediately see that the latter choice is unacceptable if $\rho (\Delta u)^2$ is to be truly similar, because we would then have

$$\frac{(\Delta u)^2}{\rho' U^2} = \frac{\bar{Y}}{Y} (X, \eta) \, g(\eta) \tag{55}$$

because ρ/ρ_∞ is generally a function of both X and Y. We therefore choose $Y = \bar{Y}$; that is, we use the premise that similarity in the turbulent energy exists in the physical rather than the Howarth-Dorodnitzyn plane. This also implies a certain insensitivity to the geometry, in agreement with Morkovin's observations. Thus Equation (53) reduces to Equation (52).

We will next recognize that the scales are given by

$$\text{Density Scale:} \quad \rho' = \rho_\infty \tag{56}$$

$$\text{Velocity Scale:} \quad U = u - u(o) \tag{57}$$

were ∞ refers to conditions outside the wake and (o) refers to conditions on the axis. The first obvious result is that

$$\frac{\rho}{\rho_\infty} \frac{(\Delta u)^2}{U^2} = g(\eta) \tag{58}$$

which for the axis reduces to

$$\frac{\rho(o)}{\rho_\infty} \frac{(\Delta u(o))^2}{U^2} = g(o) = \text{constant} \tag{59}$$

in contrast with the incompressible wake for which $\Delta u(o)/U$ = constant. Since $\rho(o) \leq \rho_\infty$ in the compressible wake, the fluctuations are initially higher (and much more so for hypersonic wakes) than for low-speed wakes. Eventually, of course, $\rho(o) = \rho_\infty$ and the constant ratio of g(o) is attained.

The radial variation of the velocity fluctuations in terms of the variable

$$\eta = \frac{Y}{L} \tag{60}$$

where L is the transverse wake scale (to be discussed shortly), obtains, directly from Equations (58) and (59)

$$\frac{\rho}{\rho(o)} \left(\frac{\Delta u}{\Delta u(o)}\right)^2 = \frac{g(\eta)}{g(o)} = f(\eta) \tag{61}$$

where $f(\eta)$ is another unique function of η. The universality of this function can be tested by comparing (for example) velocity fluctuation profiles $(\Delta u)^2/(\Delta u(o))^2$ in incompressible flows with the profiles $\rho\,(\Delta u)^2/\rho(o)\,(\Delta u(o))^2$ of the present experiment. At any rate, since $\rho \geq \rho(o)$, the profile $(\Delta u)/(\Delta u\,(o))$ in the compressible wake is somewhat thinner than in the incompressible wake.

The following corollaries can be drawn from Equations (58) and (61)

$$\frac{l}{w^2} \frac{\rho}{\rho_\infty} \left(\frac{\Delta u}{u_\infty}\right)^2 = g\,(\eta) \tag{62}$$

$$\frac{\rho\, u^2}{\rho(o)\; u(o)^2} \; \frac{(\Delta u/u)^2}{(\Delta u(o)/u(o))^2} = f(\eta) \tag{63}$$

where w is the so-called velocity defect

$$w = \frac{u_\infty - u(o)}{u_\infty} \tag{64}$$

and also

$$\frac{\Delta u(o)}{u(o)}^2 = \frac{g(o)\, w^2}{(1 - r)\,(1 - w)^2} \tag{65}$$

where the density defect

$$r \equiv \frac{\rho_\infty - \rho(o)}{\rho_\infty} \tag{66}$$

As will be discussed below, the defects W and r are known functions of the axial coordinate $\bar{X}$ so that the $\bar{X}$-dependence of the velocity fluctuations can be predicted. In the meantime, we again note the influence of compressibility on the axial decay of the velocity fluctuation on the axis, as given by Equation (66) and the axis value of Equation (62)

$$\left(\frac{\Delta u(o)}{u_\infty}\right)^2 = g(o)\, w^2 \frac{\rho_\infty}{(o)} = g(o) \frac{w^2}{1 - r} \tag{67}$$

In both cases, we observe that the fluctuation decay is faster in the compressible wake because of the decrease in r with axial distance.

4.2 TEMPERATURE AND DENSITY FLUCTUATIONS

The prediction of Equation (49) for adiabatic flows together with the likelihood of insignificant sound fields allows us to construct the similarity behavior of the temperature and density fluctuations

$$\frac{d\rho}{\rho} = - \frac{dT}{T} \tag{68}$$

$$\frac{(\Delta\rho)}{\rho} = \frac{(\Delta T)}{T} \tag{69}$$

where the parentheses again denote rms values. Equation (50) rewritten as

$$\frac{\Delta T}{T} = (\gamma - 1)\, M^2 \frac{\Delta u}{u} \tag{70}$$

immediately leads to the radial profile of the temperature fluctuations as normalized to the axis value

$$\frac{\rho}{\rho(o)} \left(\frac{u(o)}{u}\right)^2 \left(\frac{\Delta T}{\Delta T(o)}\right)^2 = f(\eta) \tag{71}$$

and its corollaries

$$\frac{\rho(o)^3}{\rho^3}\left(\frac{u(o)}{u}\right)^2\left(\frac{(\Delta\rho)}{(\Delta\rho)\ (o)}\right)^2 = f(\eta) \tag{72}$$

$$\frac{\rho(o)}{\rho}\left(\frac{u(o)}{u}\right)^2\left(\frac{(\Delta\rho)/\rho}{(\Delta\rho)\ (o)/\rho(o)}\right)^2 = f(\eta) \tag{73}$$

$$\frac{\rho(o)}{\rho}\left(\frac{u(o)}{u}\right)^2\left(\frac{\Delta T/T}{\Delta T(o)/T(o)}\right)^2 = f(\eta) \tag{74}$$

Here we note the analogies among Equations (61), (71), and (72). In the same spirit, we inquire about the axial variation of the axis values of the density and temperature fluctuations. In analogy to Equation (59) we obtain

$$\frac{\Delta T(o)}{T(o) - T_\infty} = \left[g(o)\ \frac{\rho_\infty}{\rho(o)}\right]^{1/2} (\gamma - 1)\ M(o)^2\ \frac{w\ (1 + \theta}{\theta\ (1 - w)} \tag{75}$$

where θ is the temperature defect

$$\theta \equiv \frac{T(o) - T_\infty}{T_\infty} \tag{76}$$

and where M(o) is the Mach number of the axis. A more convenient expression can be given using the experimentally determined (Reference 12) relation

$$\theta \equiv (\gamma - 1)\ M_\infty^2\, w\ S \tag{77}$$

where S is a known number on the order of 0.8 related to the turbulent Prandtl number. Then

$$\frac{\Delta T(o)}{T(o) - T_\infty} = \frac{1}{S}\left[g(o)\ \frac{\rho_\infty}{\rho(o)}\right]^{1/2} (1 - w) \tag{78}$$

The ratio of the temperature fluctuations on the axis to the temperature difference across the wake is therefore not constant, as Gibson (Reference 4) found for the sphere wake in water, but closely follows the behavior of

the density and velocity defects. In fact, the density fluctuations given by

$$\frac{\Delta\rho(o)}{\rho_\infty - \rho(o)} = \frac{1}{S}\left[g(o)\frac{\rho(o)}{\rho_\infty}\right]^{1/2}(1 - W) \tag{79}$$

analogous to Equation (78), obvious y increase with axial distance. Both Equations (78) and (79) also predict that at very far distances from the body ($\rho(o) = \rho_\infty$, $w = o$), the temperature and density fluctuations so defined approach the value $(g(o))^{1/2}/S$.

The behavior of the fluctuations as given above carry (concealed) the surmise that the appropriate density scale ρ', is, in fact, given by $\rho' = \rho_\infty$ (see Equation (56)). Furthermore, the constant g(o) is needed in applying these formulas. An interesting relation devoid of these requirements is the ratio

$$\left(\frac{\Delta\rho(o)}{\rho_\infty - \rho(o)}\right) \Big/ \left(\frac{\Delta U(o)}{U_\infty - U(o)}\right) = \frac{(1-r)(1-w)}{S} \tag{80}$$

obtained from Equations (59) and (79). Both sides of Equation (80) have been measured independently in this experiment and a check would be much in order.

4.3 SPATIAL DISTRIBUTION

The velocity, density, and temperature fluctuations are given above in terms of the mean-wake properties and particularly in terms of the defects w, θ, and r. This representation is powerful in that it bypasses an exact knowledge of the mean-property distribution in the wake. Nevertheless, the latter distributions are now well understood for compressible wakes in general and, by the results of Reference 12, for the wake at hand in particular. To describe the functional forms $\Delta U(\eta,\bar{X})$, etc., we will first list the main features of the mean flow field of this wake as given in Reference 12.

The coordinates are defined by

$$\text{Axial coordinate } \bar{X} \equiv \frac{X - X_c}{\sqrt{C_D A}} \tag{81}$$

$$\text{Radial coordinate } \eta \equiv \frac{Y}{L} \tag{82}$$

Here X is the actual distance behind the body base, X_o the X-position of the effective wake origin (found to lie about 8 diameters behind the base), and $(C_D A)^{1/2}$ is the virtual (drag) diameter of the wake; in the present instance*

$$(C_D A)^{1/2} = 0.216 \text{ cm}$$

The wake transverse scale, L, is given by

$$L = \left[\frac{C_D A}{4\pi w}\right]^{1/2} \tag{83}$$

and the velocity defect

$$w \equiv \frac{1}{\pi^{1/3}} \left(\frac{R_T}{6}\right)^{2/3} \frac{1}{\bar{X}^{2/3}} ; \quad R_T = 12.8 \tag{84}$$

It should be noted that the η of Reference 12 was formed by using the Howarth-Dorodnitzyn radius, which was very similar to the physical radius, Y, beginning a very short distance away from the axis.

The density and temperature defects are

$$\theta = (\gamma - 1) M_\infty^2 \, w \, S \tag{85}$$

*The value $(C_D A)^{1/2} = 0.278$ cm given in Reference 12 is an average including measurements in the up-down direction, less accurate than the value 0.216 cm. However, the latter value was used to compute $\bar{X}$ in Reference 12.

and

$$r = \frac{\theta}{\theta + 1} \tag{86}$$

Again, the quantity $\sigma_T^{2/3}$ appearing in place of S in Equation (38) in Reference 12 has been replaced by a more general function, S, of the turbulent Prandtl number, σ_T, which varies from about 0.78 to 0.88 along the wake, tending toward 0.84 far along the wake (see Figure 35, Reference 12).

The radial variation of properties is as follows

$$\tilde{u} \equiv \frac{u_\infty - u}{u_\infty - u(o)} = e^{-0.43\,\eta^2} \tag{87}$$

$$\tilde{T} \equiv \frac{T - T_\infty}{T(o) - T_\infty} = \left(\frac{u_\infty - u}{u_\infty - u(o)}\right)^{\sigma_T}; \quad \sigma_T = 0.785 \tag{88}$$

$$\tilde{\rho} \equiv \frac{\rho_\infty - \rho}{\rho_\infty - \rho(o)} = \tilde{T}\left[\tilde{T}\left(1 - \frac{T_\infty}{T(o)}\right) + \frac{T_\infty}{T(o)}\right]^{-1} \tag{89}$$

The values of w, θ, and r found experimentally in Reference 12 are listed in Table I. It will be noted that they obey the above relations (Equation (64), for example) only after a certain relaxation length behind the transition region. We therefore anticipate that a similar relaxation period will be found in the fluctuations, i.e., that the findings of Paragraphs 4.1.1 and 4.1.2 may, if at all, fit the data only after some distance behind the body. Based on Reference 12, this distance was a minimum of 40 in $\bar{X}$, contrasted with the distance $\bar{X} \simeq 90$ covered by the measurements.

By combining the equations of Paragraphs 4.1.1 and 4.1.2 with those of Paragraphs 4.1.3, the behavior of the fluctuations along the wake can be predicted. For brevity, these combinations are outlined in Table II. At intermediate $\bar{X}$'s the similarity behavior of the compressible wake differs distinctly from that of the incompressible wake because of density factors such as the ratio $\rho(o)/\rho_\infty$ and the defect, r. This intermediate region

TABLE I

MEAN-WAKE PROPERTIES ON WAKE AXIS (FROM REFERENCE 12)

X-Station	$\bar{X}$	w	θ	r
0	14.71	0.276	0.754	0.433
1	20.60	0.222	0.622	0.379
2	26.50	0.181	0.522	0.334
3	32.39	0.150	0.435	0.303
4	38.28	0.137	0.327	0.253
5	44.17	0.107	0.313	0.246
6	50.07	0.0951	0.283	0.225
7	55.96	0.0731	0.231	0.186
8	61.85	0.0688	0.211	0.167
9	67.75	0.0615	0.181	0.165
10	73.64	0.0595	0.171	0.168
11	79.53	0.0564	0.173	0.133
12	85.42	0.0559	0.168	0.116
13	91.32	0.0490	0.149	0.138

should not be confused with the relaxation region mentioned previously; we do still expect similarity behavior with radial distance in the former but not in the latter. Again, note that $\Delta u/(u_\infty - u(o))$ and $\Delta\rho/(\rho_\infty - \rho(o))$ change with $\bar{X}$ and the former decreases toward its asymptotic limit $\sqrt{g(o)}$, whereas the latter increases toward its limit $\sqrt{g(o)}/S$--limits which will, incidentally, be identical if the Prandtl number (and thus also S) is unity. The velocity fluctuation decay obeys incompressible rules* only in the limit of very large $\bar{X}$.

It remains to evaluate g(o) which, in view of our committment to the dynamic equilibrium hypothesis, should be similar to the incompressible values. Unfortunately, the axi-symmetric experiments of References 2, 3, and 5

*These include the so-called "final period" of the wake.

TABLE II

TURBULENT FLUCTUATIONS IN WAKES

Fluctuation	Form	Behavior	
		At Moderate $\bar{X}$	At Large $\bar{X}$
$\Delta u(o)/(u_\infty - u(o))$	$[g(o)\,\rho_\infty/\rho(o)]^{1/2}$	Decreases as $[\rho_\infty/\rho(o)]^{1/2}$	$g(o)^{1/2}$
$[\Delta u(o)/u(o)]^2$	$g(o)\,w^2/(1 - r)(1 - w)^{1/2}$	Decreases rapidly	0
$(\Delta u(o)/u_\infty)^2$	$g(o)\,w^2/(1 - r)$	Decreases rapidly	0
$\Delta T(o)/(T(o) - T_\infty)$	$[g(o)\,\rho_\infty/\rho(o)]^{1/2}(1 - w)/S$	Changes with $\bar{X}$	$g(o)^{1/2}/S$
$\Delta\rho(o)/(\rho_\infty - \rho(o))$	$[g(o)\,\rho(o)/\rho_\infty]^{1/2}(1 - w)/S$	Increases with $\bar{X}$	$g(o)^{1/2}/S$
$\dfrac{\Delta\rho(o)/(U_\infty - u(o))}{\Delta u(o)/(\rho_\infty - \rho(o))}$	$(1 - r)(1 - w)/S$	Increases with $\bar{X}$	S^{-1}

Note: $g(o)$ = constant $\simeq 0.14$

S = constant $\simeq 0.84$

$r = (\rho_\infty - \rho(o))/\rho_\infty$

$w = (u_\infty - u(o))/u_\infty$

lack the adequacy and clarity of data from which g(o), which seems to tend towards unity near the body, can be obtained at large $\bar{X}$. It is interesting, however, that Townsend (Reference 1, Page 135) obtained the value g^2 (o) = 0.136 in the two-dimensional wake.

We close this discussion with the remark that the $\bar{X}$ dependencies of the velocity defect, the transverse scale L, etc., as shown above, have the exact form exhibited at low speeds, including the numerical values of the coefficients (R_T for example). Furthermore, these expressions have been validated in the compressible wake by the experimental results of Reference 12 and thus add to the expectation that the predictions of the DEH will also be validated for the fluctuation.

4.4 CORRELATIONS, SPECTRA, AND SCALES

There are some definite, although semiqualitative, predictions the DEH makes concerning the local velocity-temperature correlation (cross-correlation) as well as the fluctuation spectral density. If our picture of large-eddy equilibration is correct, then we expect Equation (51) to hold, and principally so for the large eddies (low frequencies); the rationale is that large eddies, unaffected as they are by internal mixing, best represent the extreme conditions across shear zones. In fact, velocity-temperature correlation measurements (References 10, 15, and 17) show that these two quantities are usually strongly (although not perfectly) anti-correlated. By the same token, one expects, in the absence of ΔT_o fluctuations, Equation (50) for the temperature-velocity fluctuation ratio to perform best at the lower frequencies. Both these phenomena are illustrated by Morkovin (Reference 10) for the boundary layer.

The integral scale of turbulence (i.e., the autocorrelation macroscale) should be expected to scale with the transverse scale of the wake mean flow

$$\Lambda \sim L$$

with the constant of proportionality to be determined by the experiment. The microscales of the autocorrelation functions will be discussed in a later report.

SECTION 5

RESULTS OF MODAL ANALYSIS

The experimental results are summarized in the form of the axis values in Table III. In this section we shall present the results of the modal analysis of the wake turbulence (the frequency-integrated fluctuation intensities) beginning with the wire-sensible variables, i.e., the fluctuations in the mass-flow-flux ρu and the total temperature T_o, along with their cross-correlation coefficient. These results, put out by the WEB-IV program (Appendix D) derive from the solution of Equation (28) (Paragraph 2.6.2) with the inputs of the latter deriving from the experiment.

Figure 15 shows the variation of the rms mass-flux and total temperature fluctuations along the axis, where the fluctuations are normalized by the local (axis) mean values. Note that the total temperature fluctuations are in fact quite small, attaining a maximum value of 7 percent in the region studied and decaying to about 1 percent at 100 diameters downstream of transition. This is considerably below all other fluctuation levels and especially, as will be seen below, the fluctuations in the static temperature. We already see an indication that Morkovin's strong Reynolds analogy (Reference 10) for adiabatic flows, which implies the criterion of Equation (49), is at work. The correlation coefficient r_{mt} between mass flux

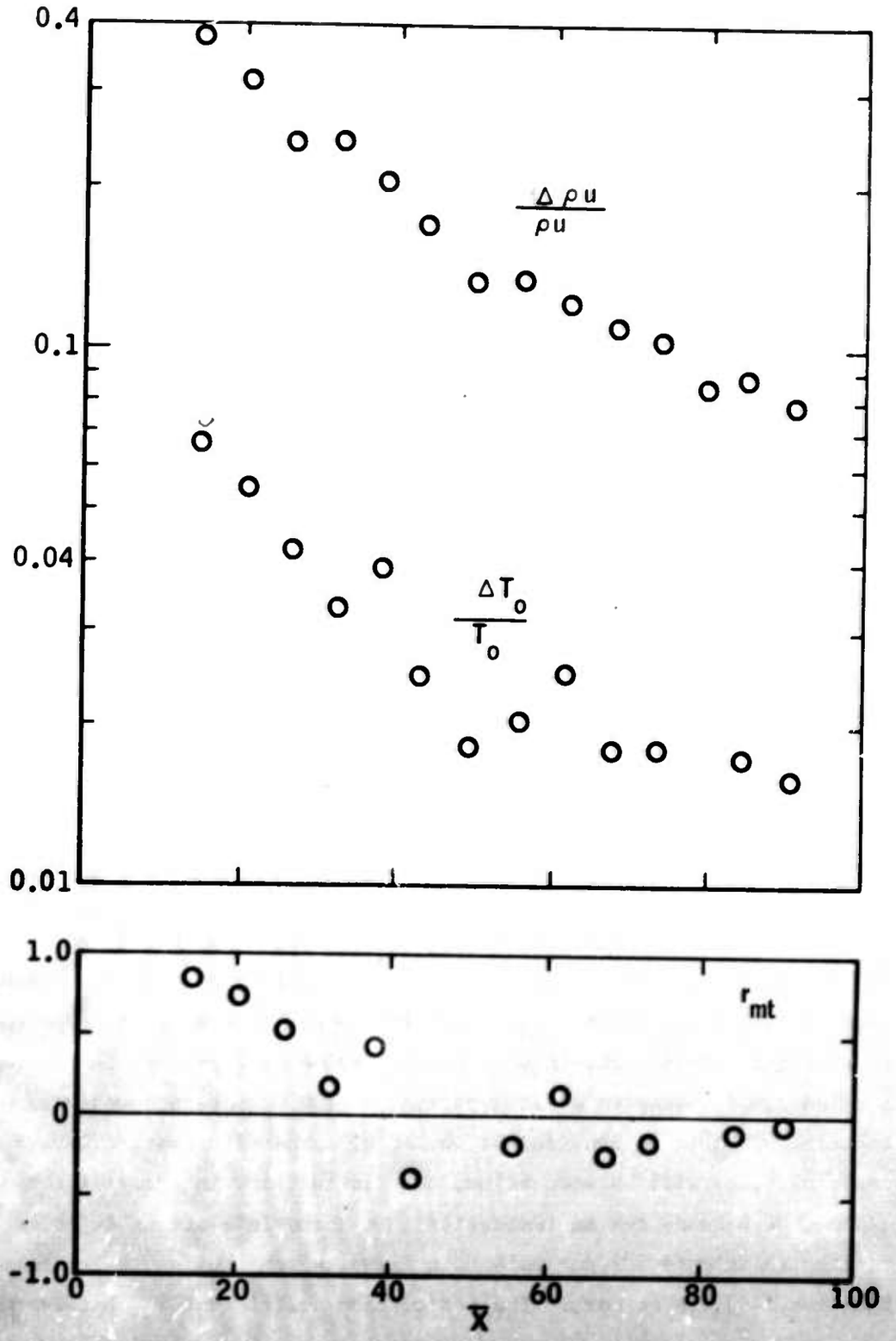

FIGURE 15. AXIAL DEPENDENCE OF THE AXIS VALUES OF THE RMS NORMALIZED MASS-FLUX AND TOTAL TEMPERATURE FLUCTUATIONS AND THEIR CROSS-CORRELATION COEFFICIENT.

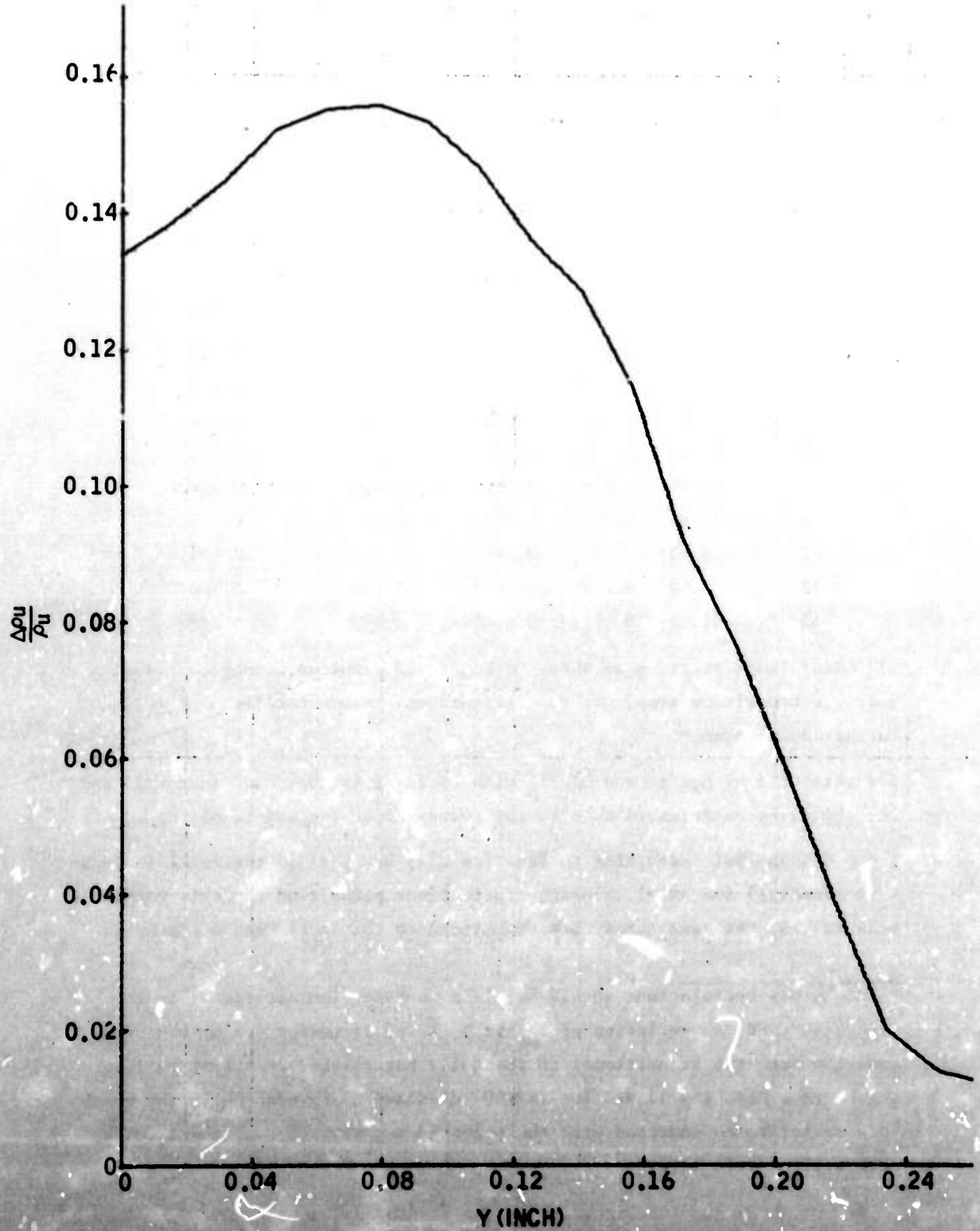

FIGURE 16. TYPICAL RADIAL VARIATION OF THE RMS MASS-FLUX FLUCTUATION NORMALIZED WITH THE LOCAL MASS FLUX.

TABLE III

TURBULENCE PROPERTIES ON WAKE AXIS

X-Station	$\bar{X}$	$\Delta u/u$	$\Delta \rho/\rho$	$\Delta u/(u_\infty - u(0))$	$\Delta \rho/(\rho_\infty - \rho(0))$
0	14.71	0.210	0.142	0.549	0.186
1	20.60	0.156	0.148	0.548	0.243
2	26.50	0.113	0.136	0.511	0.27?
3	32.39	0.0937	0.154	0.532	0.356
4	38.28	0.0793	0.125	0.501	0.369
5	44.17	0.0531	0.114	0.442	0.350
6	50.07	0.0230	0.100	0.220	0.344
7	55.96	0.0361	0.0993	0.458	0.434
8	61.85	0.0350	0.0852	0.473	0.424
9	67.75	0.0280	0.080	0.430	0.420
10	73.64	0.0252	0.0781	0.399	0.389
11	79.53	-	0.0649	-	0.423
12	85.42	0.0224	0.0658	0.378	0.500
13	91.32	0.0192	0.0591	0.373	0.368

and total temperature, also shown in Figure 15, implies strong correlation near the transition zone, but the fluctuations become totally uncorrelated further downstream.*

The variation of $\Delta\rho u/\rho u$ and $\Delta T_o/T_o$ with radius Y is shown in Figures 16 and 17, typically represented by a radial survey about the middle of the wake.

The modal analysis according to Equation (31) has yielded the local temperature (density) and axial velocity fluctuations normalized to their respective mean values, the same quantities normalized to the local mean differences

*Since cross-correlations should be ±1 in unsteady laminar flows, it is suggested that the variation of r_{mt} in $0 \leq \bar{X} \leq 40$ is indicative of the progression from the transitional to the fully established turbulent regime; this agrees with the relaxation ($\bar{X} \cong 40$) distance of Reference 12. However, this is not to be confused with the expected behavior of $r_{\sigma T}$, about which more will be said later.

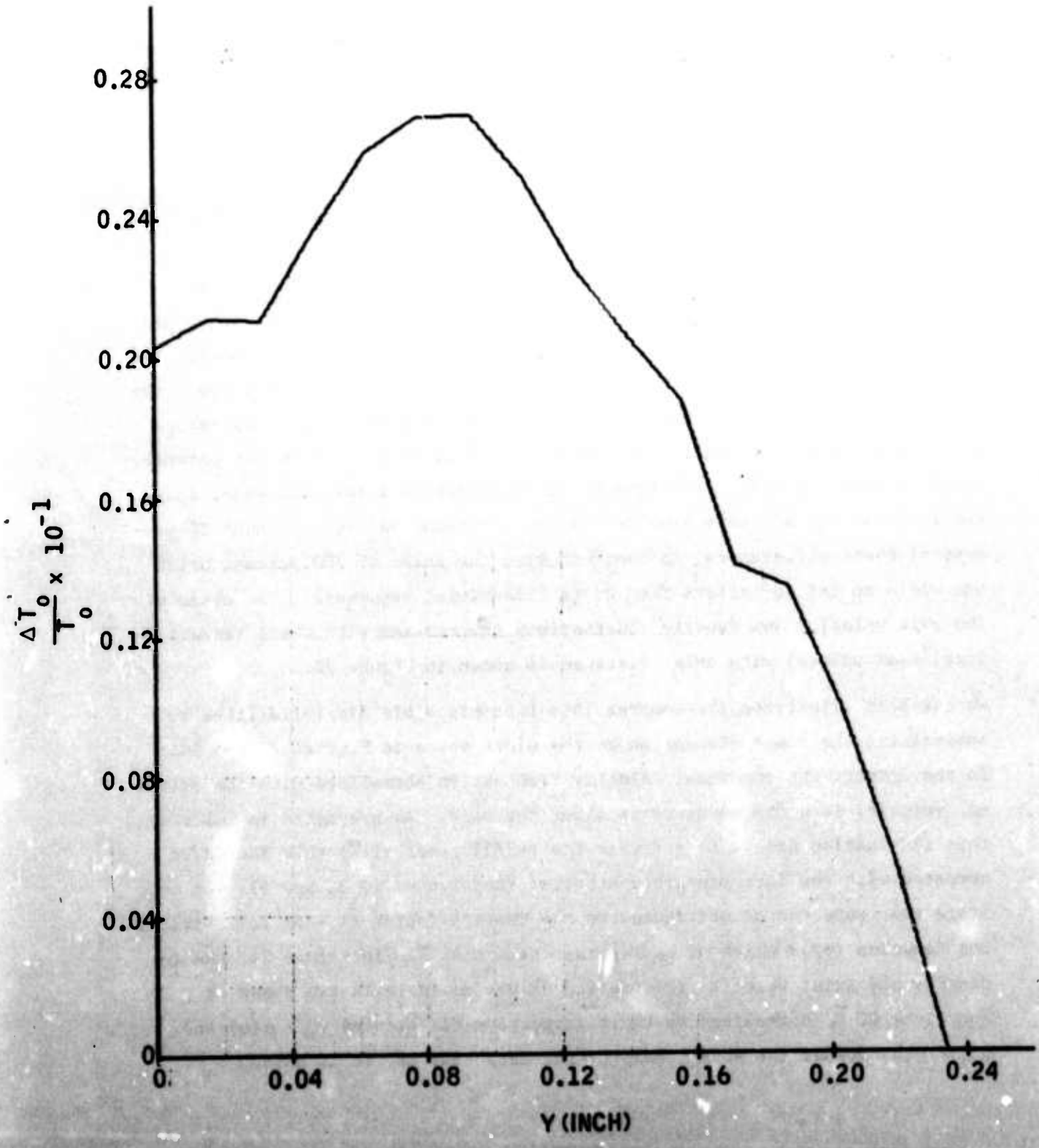

FIGURE 17. TYPICAL RADIAL VARIATION OF THE RMS TOTAL TEMPERATURE FLUCTUATION NORMALIZED WITH THE LOCAL TOTAL TEMPERATURE. COMPARE MAGNITUDES WITH FIGURE 16.

across the wake, and the velocity-temperature correlation coefficient which is, of course, equal in magnitude but opposite in sign to the velocity-density correlation. These quantities are available at the computer output plotted versus the physical radius Y in inches as well as the normalized radial distance $\eta = Y/L$ where L is the transverse wake scale available from the mean measurements of the WEB-V computer output (Reference 12).

These turbulence data will be discussed first, as plotted, without regard to the DEH and its extension to compressible flows. We note, first, the representative plots of Figures 18, 19, 20, and 21. Both modes peak at some distance off the axis, with the peak in the density fluctuations higher and farther out from the axis. In terms of their local values, the velocity fluctuations are considerably lower than the density fluctuations; since the Mach number in the wake ranges between 1.5 and 3 and the total temperature fluctuations are very small, this behavior immediately confirms the general trend of Equation (49). In terms of the differences across the wake, these two fluctuations are very similar and their maximum values are about 50 percent of these differences, in contrast with the value of 100 percent which one would be led to believe from rough dimensional arguments. The decay of the axis velocity and density fluctuations (normalized with their respective local mean values) with axial distance is shown in Figure 22.

We can best illustrate the compressible-incompressible dissimilarities by summarizing the above discussion by the plots shown in Figures 23 and 24. In the former, the rms axial velocity fluctuation normalized with the external velocity is shown to decrease along the axis. As predicted in Table II, this fluctuation decays faster than the (-2/3) power of $\bar{X}$; this should be compared with the incompressible behavior (References 2, 3, and 5). At this stage the cause can be attributed to the density factor $(1 - r)$ (cf. Table II and Equation (67)) which of course increases with $\bar{X}$. In Figure 24, the rms density and axial velocity fluctuation values on the axis are shown as functions of $\bar{X}$, normalized to their respective differences $\rho_\infty - \rho(o)$ and $u_\infty - u(o)$ across the wake. Despite the data scatter, it is quite

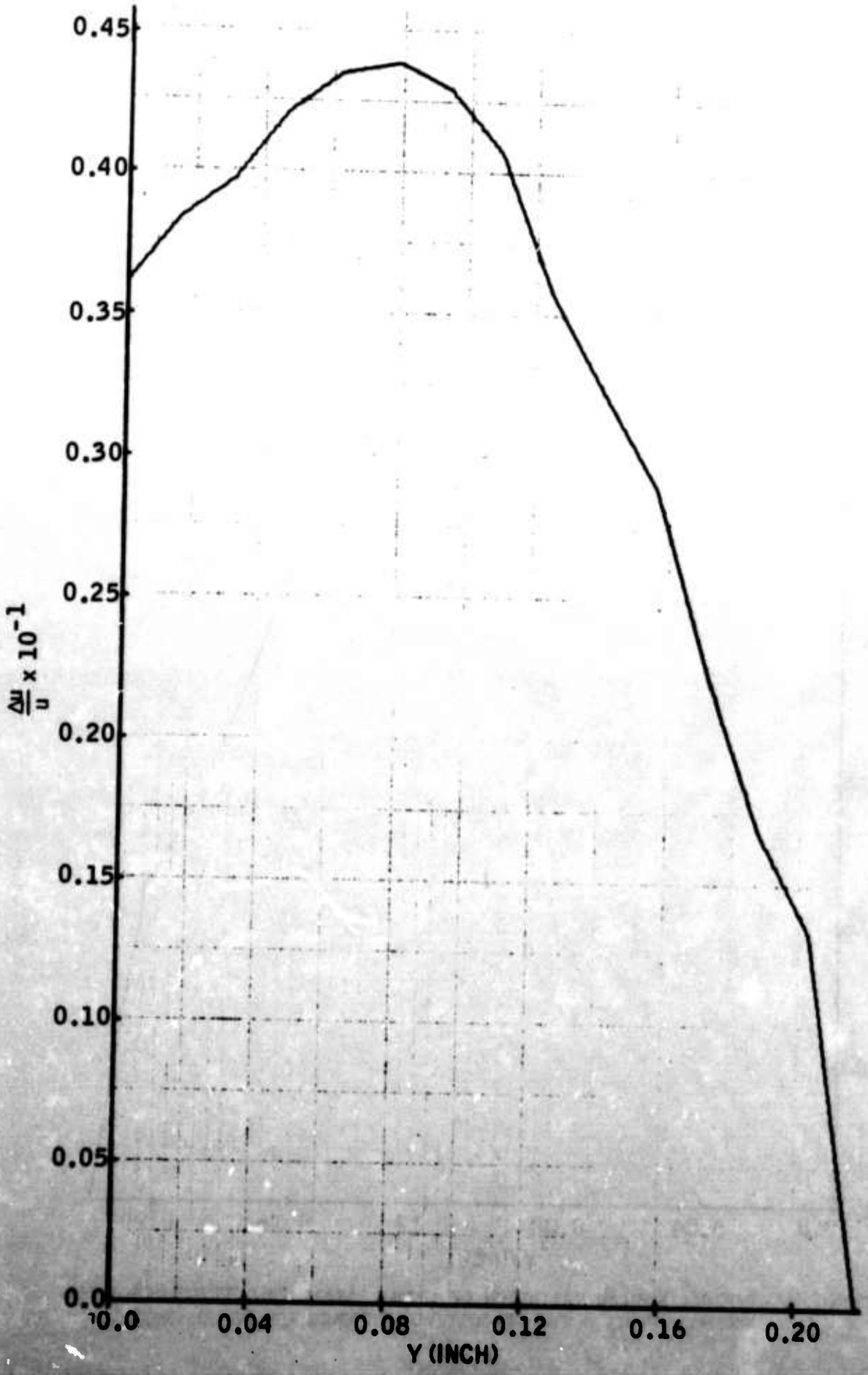

FIGURE 18. TYPICAL RADIAL VARIATION OF RMS AXIAL VELOCITY FLUCTUATION NORMALIZED WITH THE LOCAL VELOCITY.

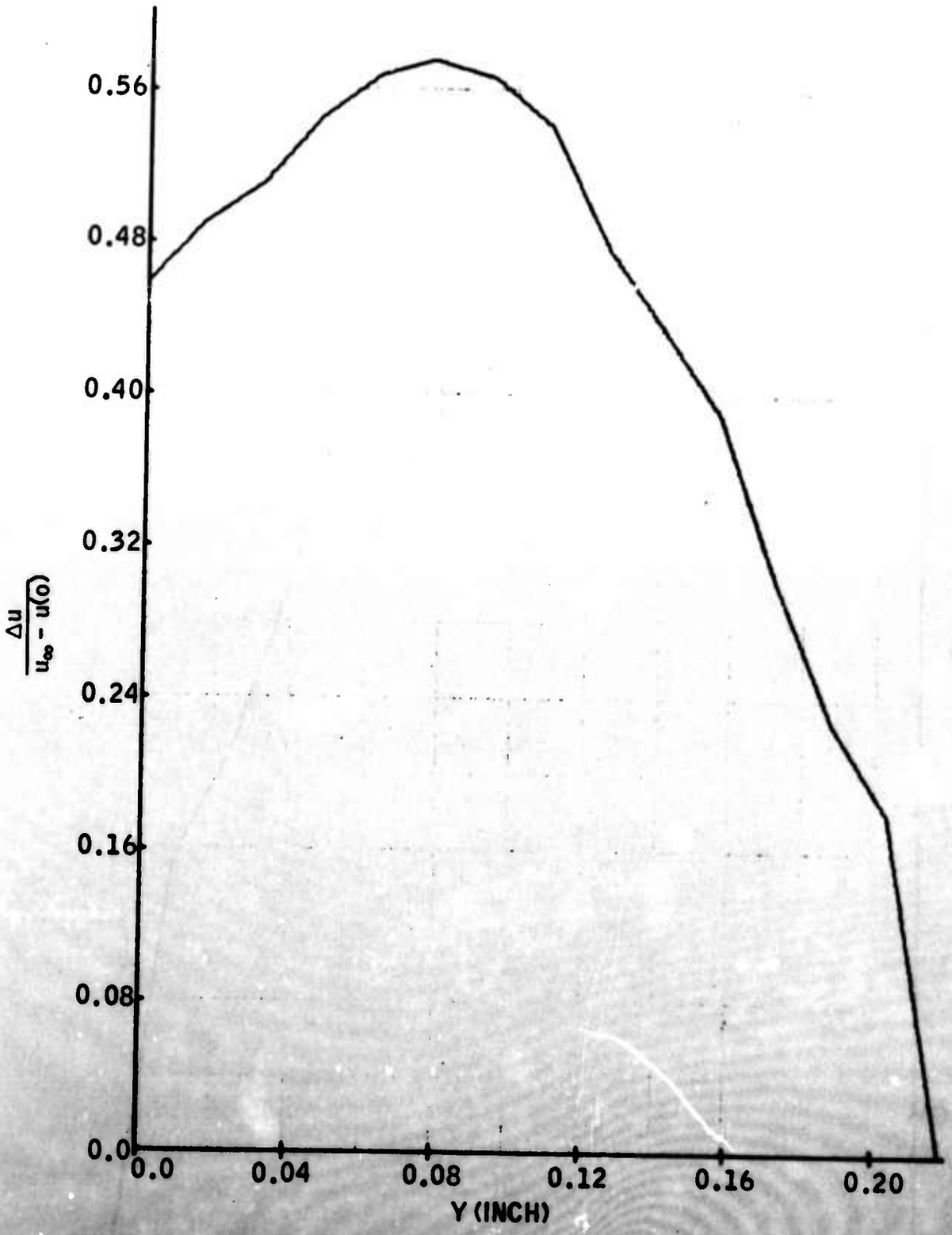

FIGURE 19. TYPICAL RADIAL VARIATION OF RMS AXIAL VELOCITY FLUCTUATION NORMALIZED WITH THE VELOCITY DIFFERENCE ACROSS THE WAKE.

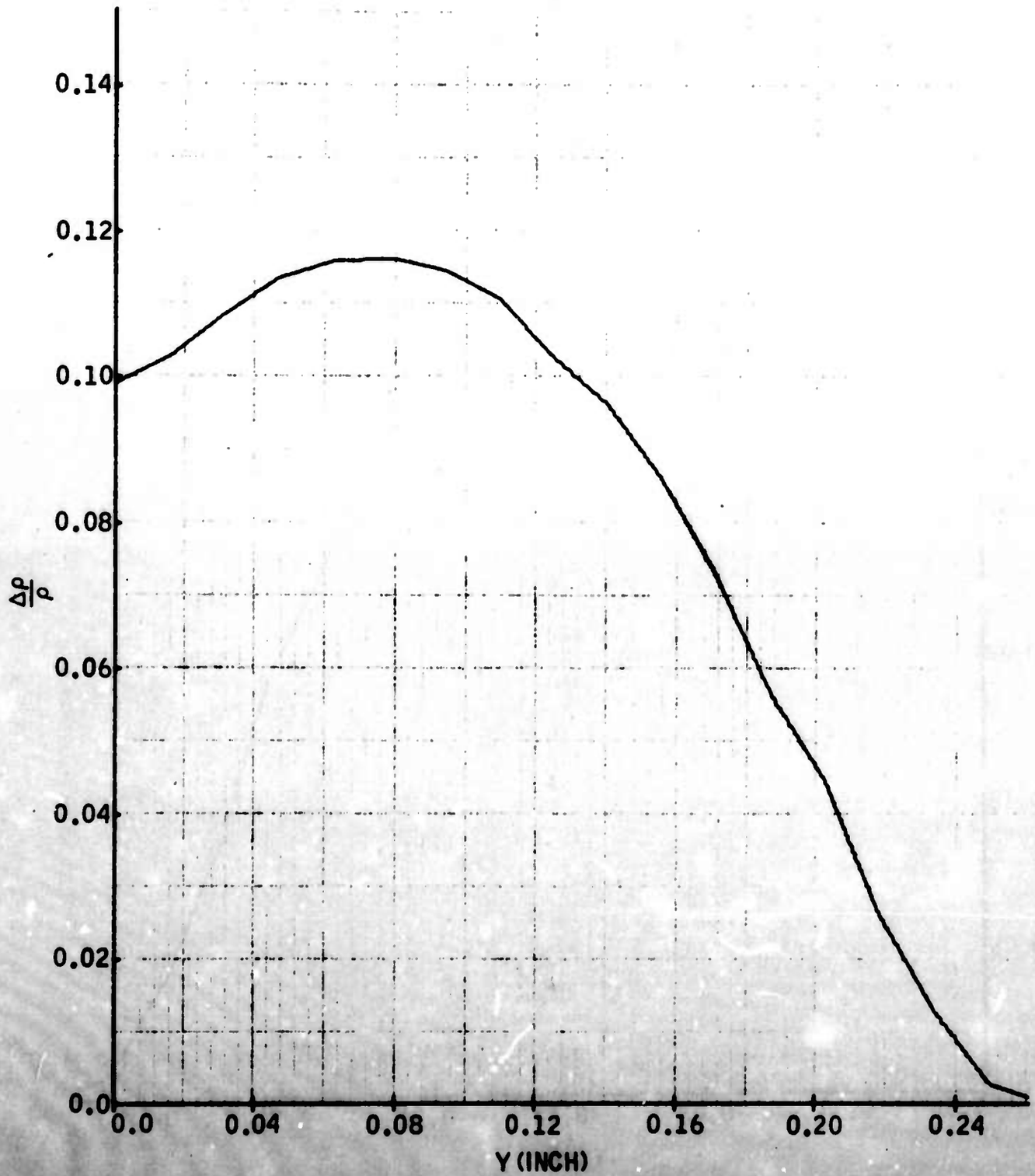

FIGURE 20. TYPICAL RADIAL VARIATION OF RMS DENSITY FLUCTUATION NORMALIZED WITH THE LOCAL DENSITY.

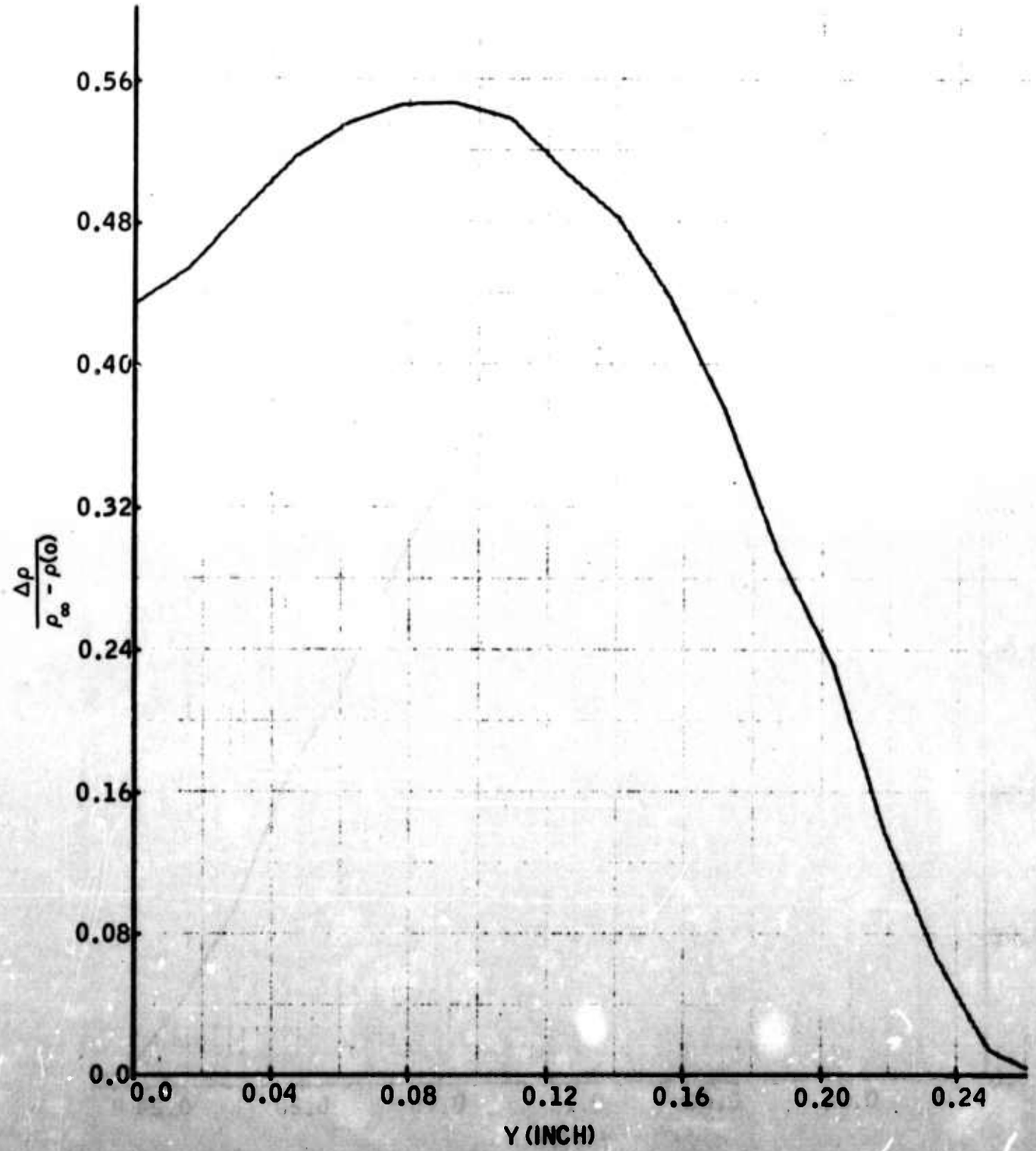

FIGURE 21. TYPICAL AXIAL VARIATION OF RMS DENSITY FLUCTUATION NORMALIZED WITH THE DENSITY DIFFERENCE ACROSS THE WAKE.

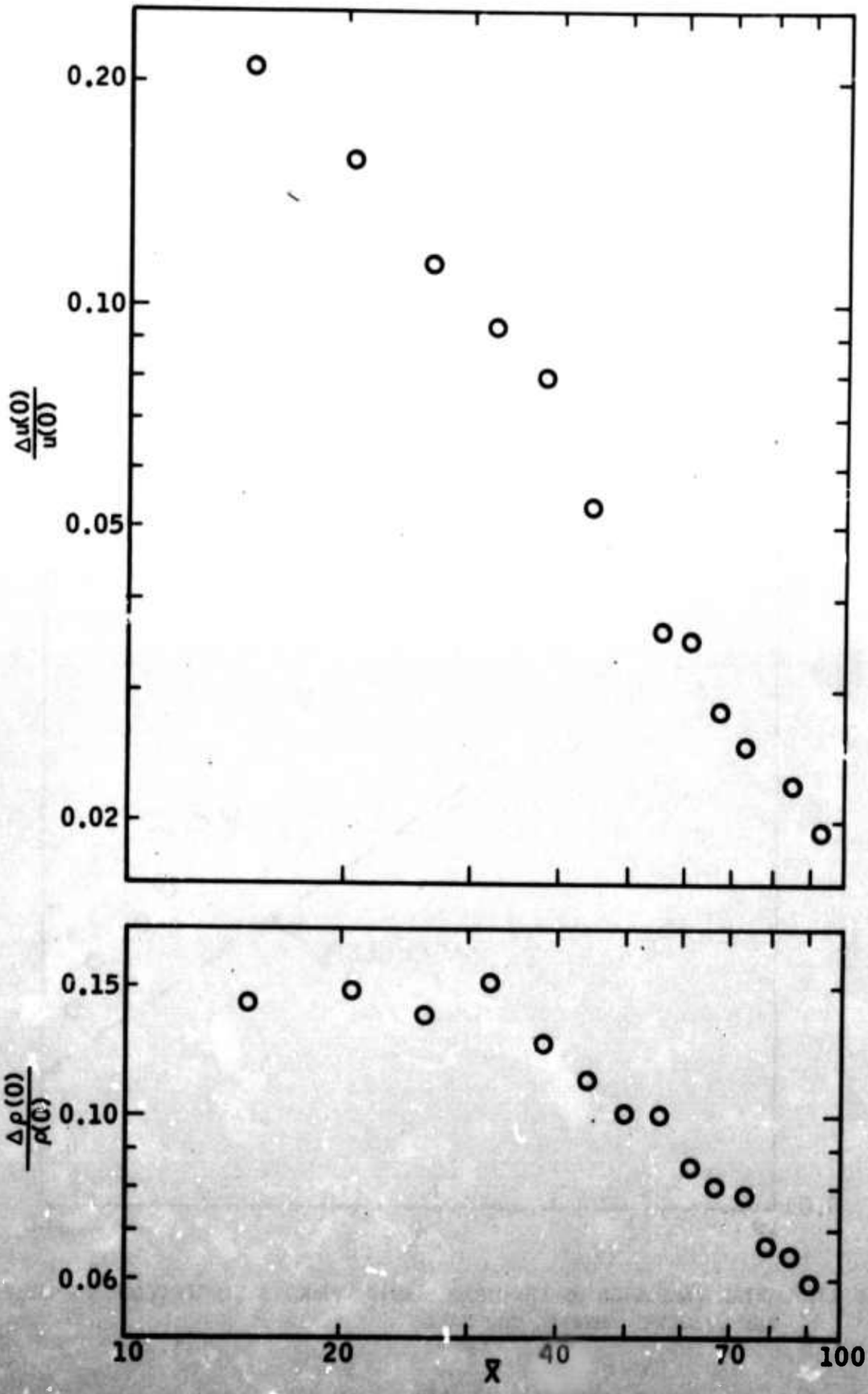

FIGURE 22. AXIAL VARIATION OF THE RMS AXIS VELOCITY (TOP) AND DENSITY (BOTTOM) FLUCTUATION NORMALIZED WITH THEIR RESPECTIVE LOCAL MEAN VALUES.

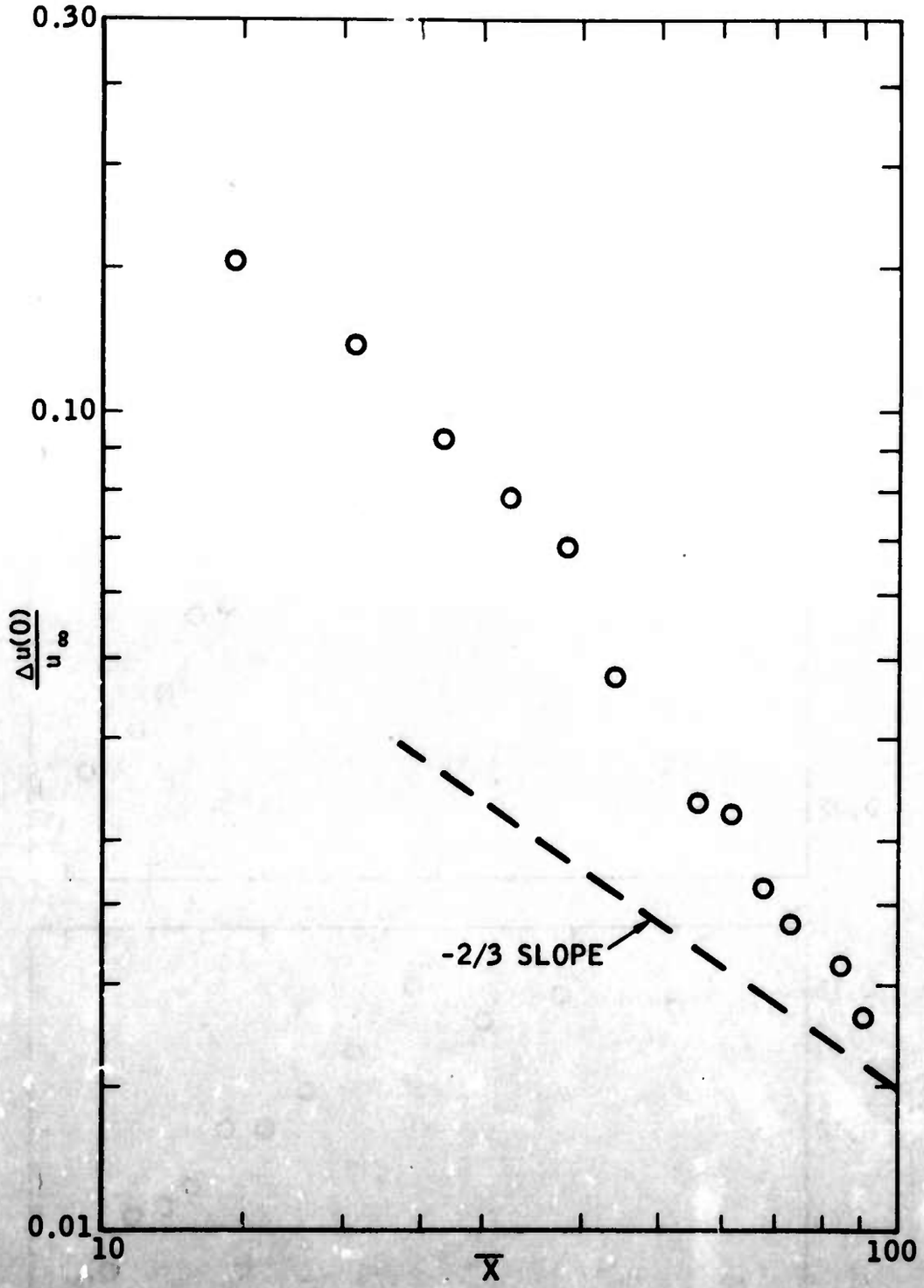

FIGURE 23. AXIAL VARIATION OF THE RMS AXIS VELOCITY FLUCTUATION NORMALIZED WITH THE VELOCITY OUTSIDE THE WAKE.

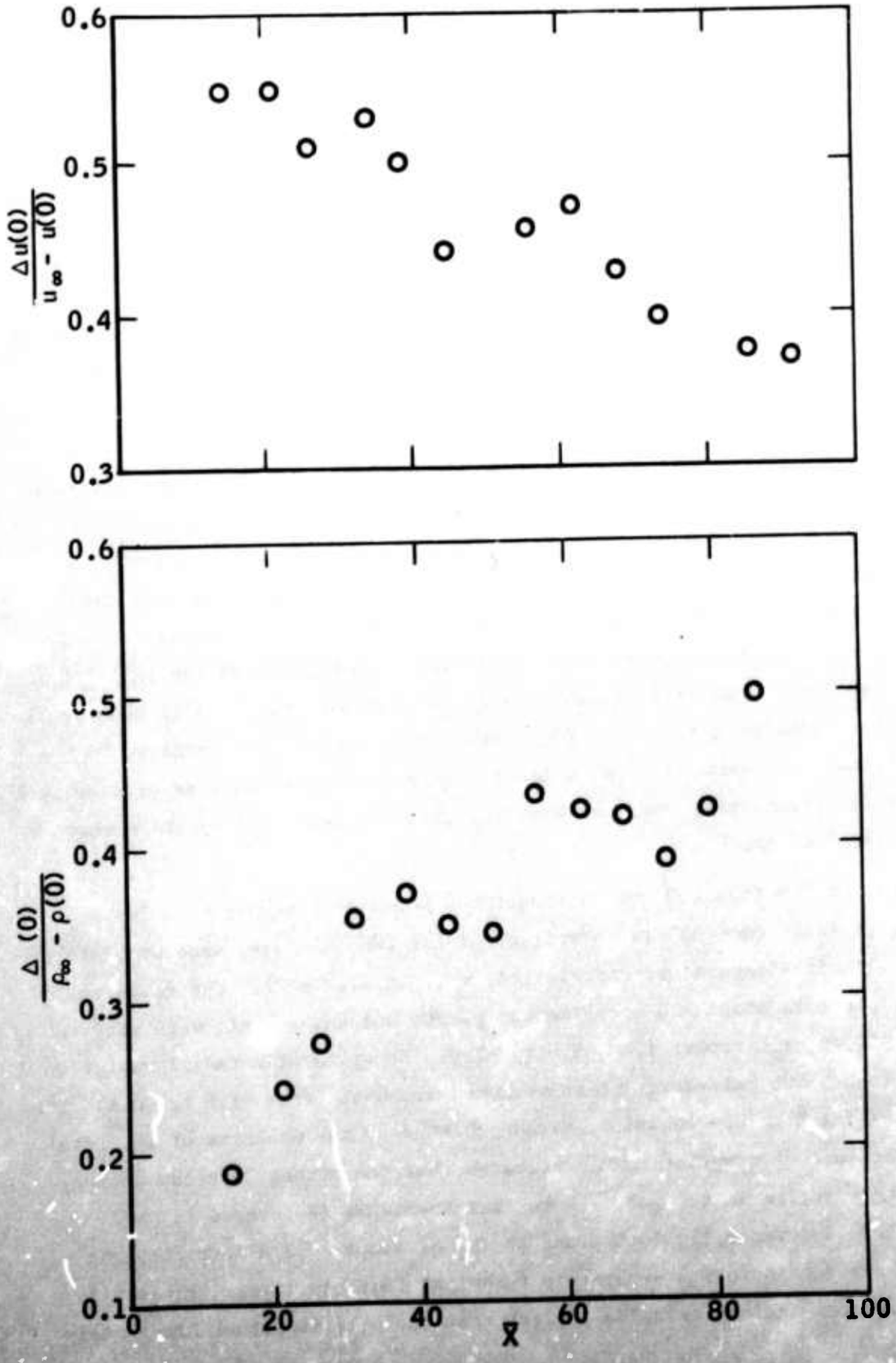

FIGURE 24. AXIAL VARIATION OF THE RMS AXIS VELOCITY (TOP) AND DENSITY (BOTTOM) FLUCTUATIONS NORMALIZED WITH THEIR RESPECTIVE DIFFERENCES ACROSS THE WAKE.

obvious that these quantities are each far from unity and in fact change in opposite directions--the velocity fluctuations decreasing, and the density fluctuations increasing, with increasing $\bar{X}$. A quick look at Table II indicates that this behavior agrees well with the dynamic equilibrium hypothesis.

Still, the central test is the behavior of the rms fluctuations normalized to the axis fluctuation with radial distance; these are plotted against the normalized radius in Figures 25 and 26 for $\bar{X} > 44$. For the velocity fluctuations, the apparent lack of perfect similarity is due largely to experimental scatter. The role of similarity behavior is shown better in the density fluctuations (Figure 26) and here it will be seen that by replotting these points according to Equation (72), their dispersion is considerably decreased. This dispersion is much worse for $\bar{X} < 44$ than Figure 26 indicates; the peak on each curve of $\Delta\rho/\Delta\rho(o)$ exceeds 2.0 nearer the body. A further point worth retaining from Figures 25 and 26 is that the peak in the density fluctuation is farther out (near $\eta = 2$) than it is for the velocity (cf. Figure 25). This difference is too large to be explained by arguments of a "thicker temperature wake" and, as will be seen shortly, practically vanishes when the data are replotted by the method suggested by the DEH.

A test of Equation (50) which enunciates Morkovin's strong Reynolds analogy (Reference 10) (a corrollary of the DEH) was also made by plotting the velocity-temperature correlation, $r_{\sigma T}$, in Figure 27. The $r_{\sigma T}$ versus η plot presents about 250 experimental points and shows that, with very few exceptions, $r_{\sigma T}$ ranges from -0.8 to -1.0. No systematic radial variation was found, but anti-correlation weakened somewhat (from -1.0 to -0.8) with increasing $\bar{X}$. This behavior, already hinted by the weakness of the total temperature fluctuations ΔT_o, indicates that the strong Reynolds analogy was very active in the wake. Note that Kovasznay (Reference 15) and Kistler (Reference 17) both found an $r_{\sigma T}$ of about -0.7 almost constant with distance across a supersonic turbulent boundary layer. Physically interpreted anti-correlation implies that the wire is struck alternately

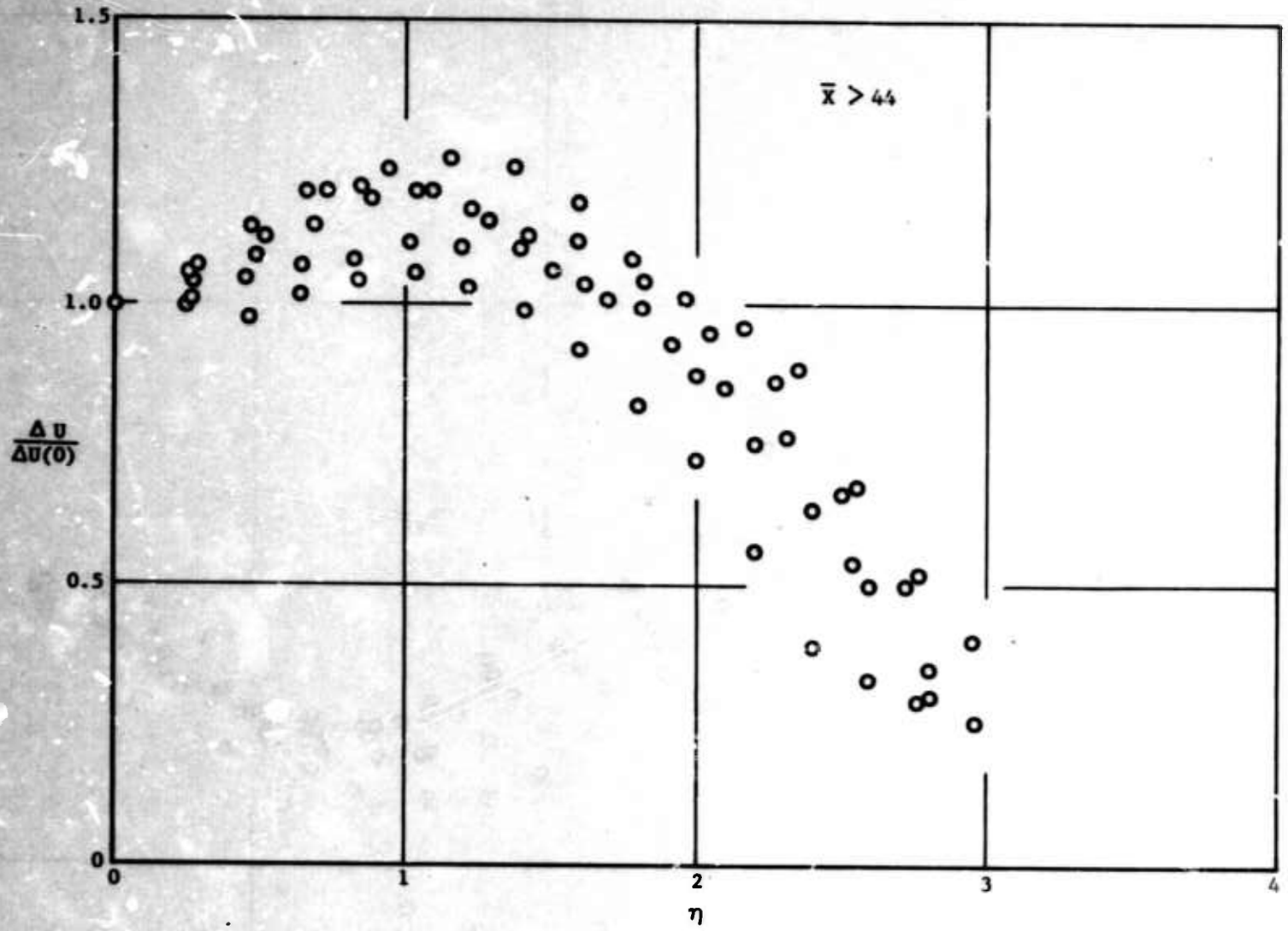

FIGURE 25. RADIAL DISTRIBUTION OF THE RMS AXIAL VELOCITY FLUCTUATIONS NORMALIZED WITH THE AXIS VALUE, FAR IN THE WAKE.

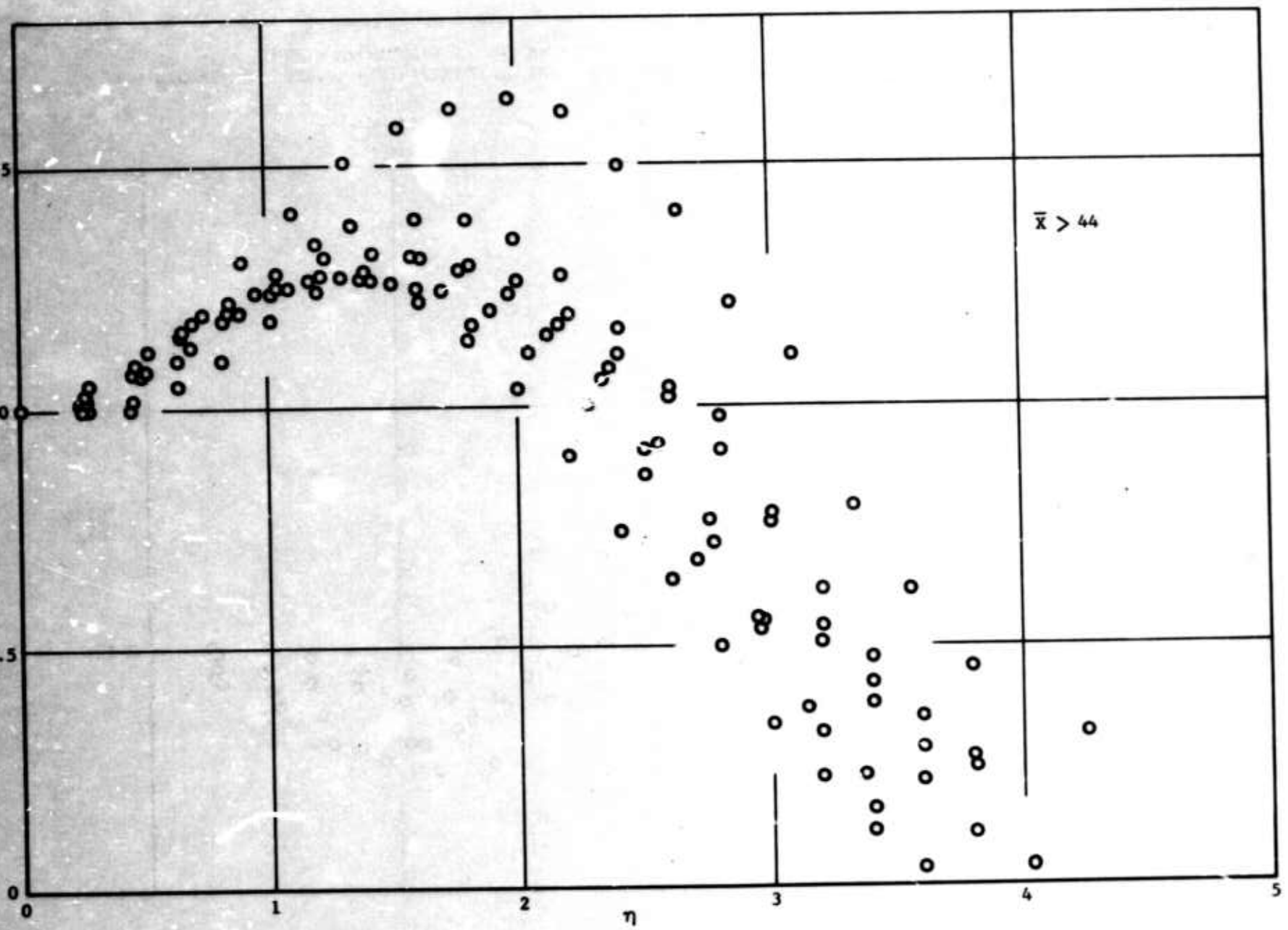

FIGURE 26. RADIAL DISTRIBUTION OF THE RMS DENSITY FLUCTUATIONS NORMALIZED WITH THE AXIS VALUE, FAR IN THE WAKE.

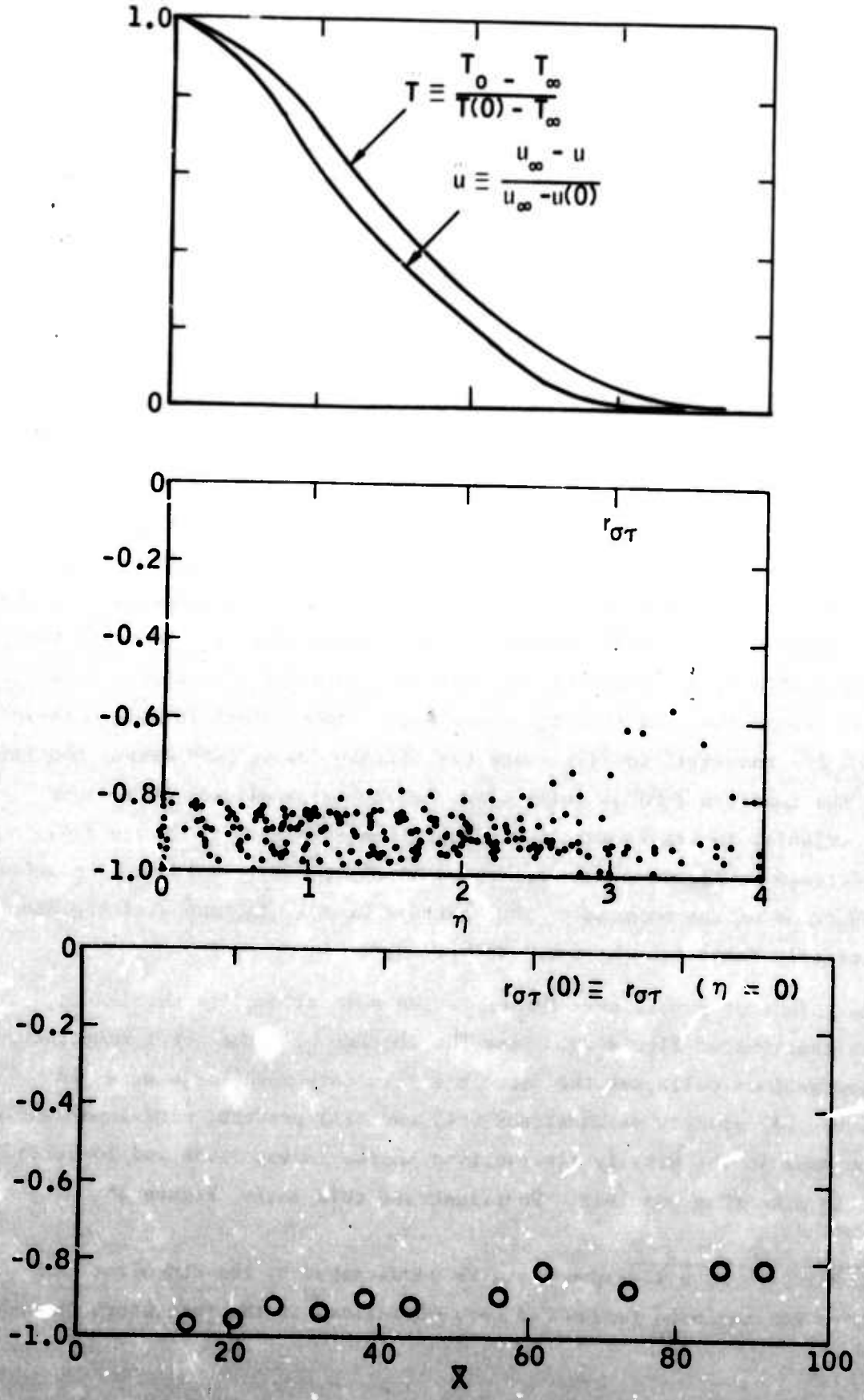

FIGURE 27. AXIAL AND RADIAL VARIATIONS OF THE VELOCITY-TEMPERATURE CROSS-CORRELATION COEFFICIENT. THE MEAN PROPERTY VARIATIONS ARE SHOWN AT THE TOP FOR COMPARISON.

by cold and fast or hot and slow moving fluid, illustrating the rather rapid transfer across the shear zone and the long reach of the large eddies.

So far, the data have been purposefully presented and discussed in a manner showing the inadequacy of low-speed arguments to cover the behavior of the compressible turbulent wake. If these arguments are indeed special cases of the DEH in the constant-density limit, then better engineering correlations can be achieved by regrouping the present data as indicated by the formulas of Paragraph 4.1.1. We shall present these correlations below.

First, we look for similarity in the radial profiles of velocity and density fluctuations. In Figure 28, the velocity fluctuations are plotted as per Equation (61), and this plot should be compared with that of Figure 25. There is obviously little difference between these two illustrations, which can be attributed to both the unavoidable data scatter and the fact that the density gradients extant in this measurement are too small to illuminate the difference. In any event, the form of the function $f(\eta)$ is quite clear and is, as expected, very close numerically to its form at low speeds (see Reference 1, Figure 7.4, Reference 3, Figure 9, and Reference 5, Figure 17), including the location and value of the maximum.* This forms a strong argument that the DEH correctly describes the compressible wake.

The effect of proper correlation is the more evident in the density fluctuations of Figure 29. Here the absence of large total temperature fluctuations collapses the data to a form very much the same as in Figure 28, exactly as Equations (61) and (71) predict; more importantly, the peak in the density fluctuations shifts in magnitude and location so as to make that possible. To illustrate this shift, Figure 30 has been

*Comparison with low-speed data is handicapped by the nonuniform manner by which the wake radius has been normalized in the references quoted.

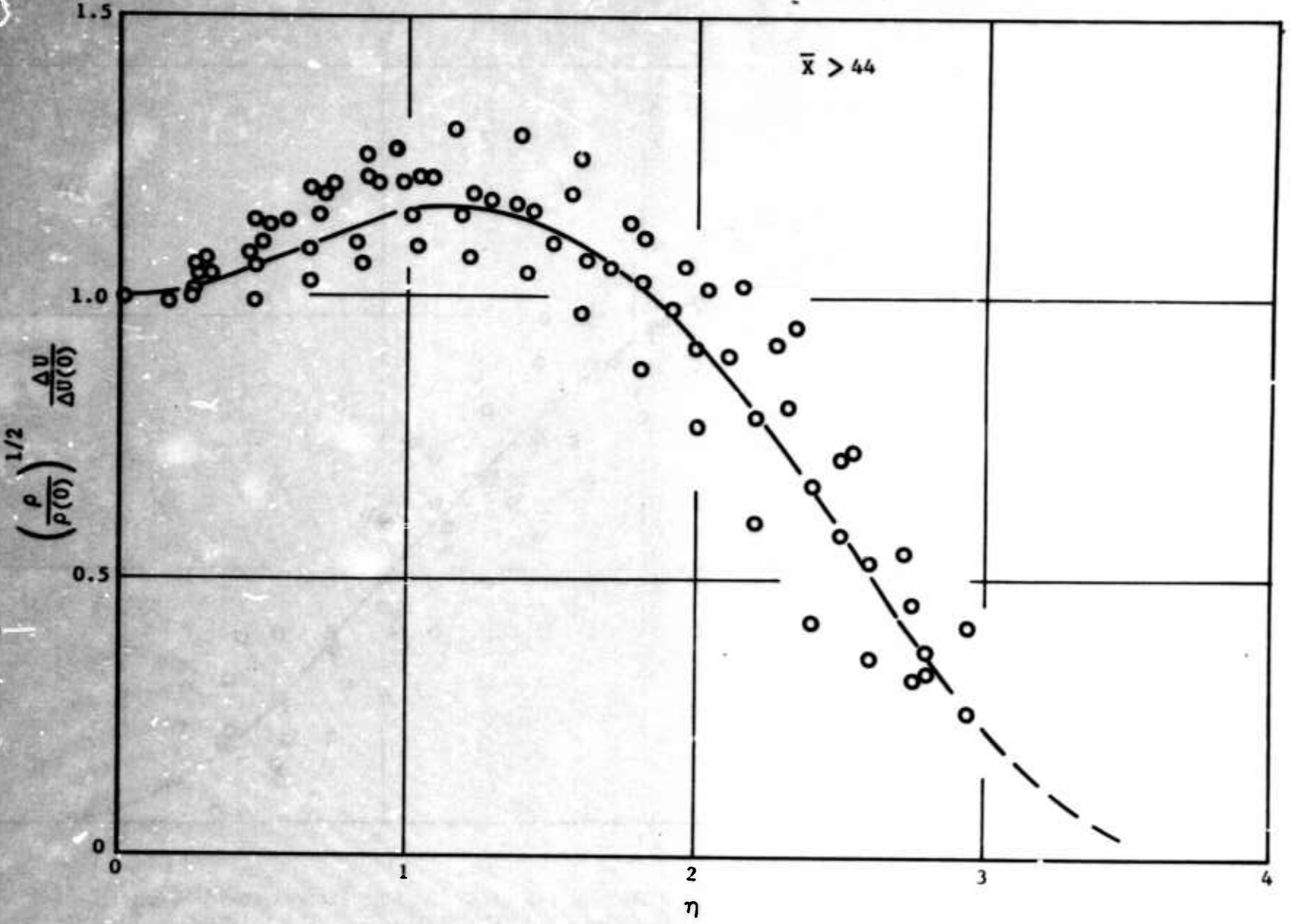

FIGURE 28. APPARENT SELF-PRESERVING FORM OF THE RMS AXIAL VELOCITY FLUCTUATIONS NORMALIZED ACCORDING TO THE DYNAMIC EQUILIBRIUM HYPOTHESIS.

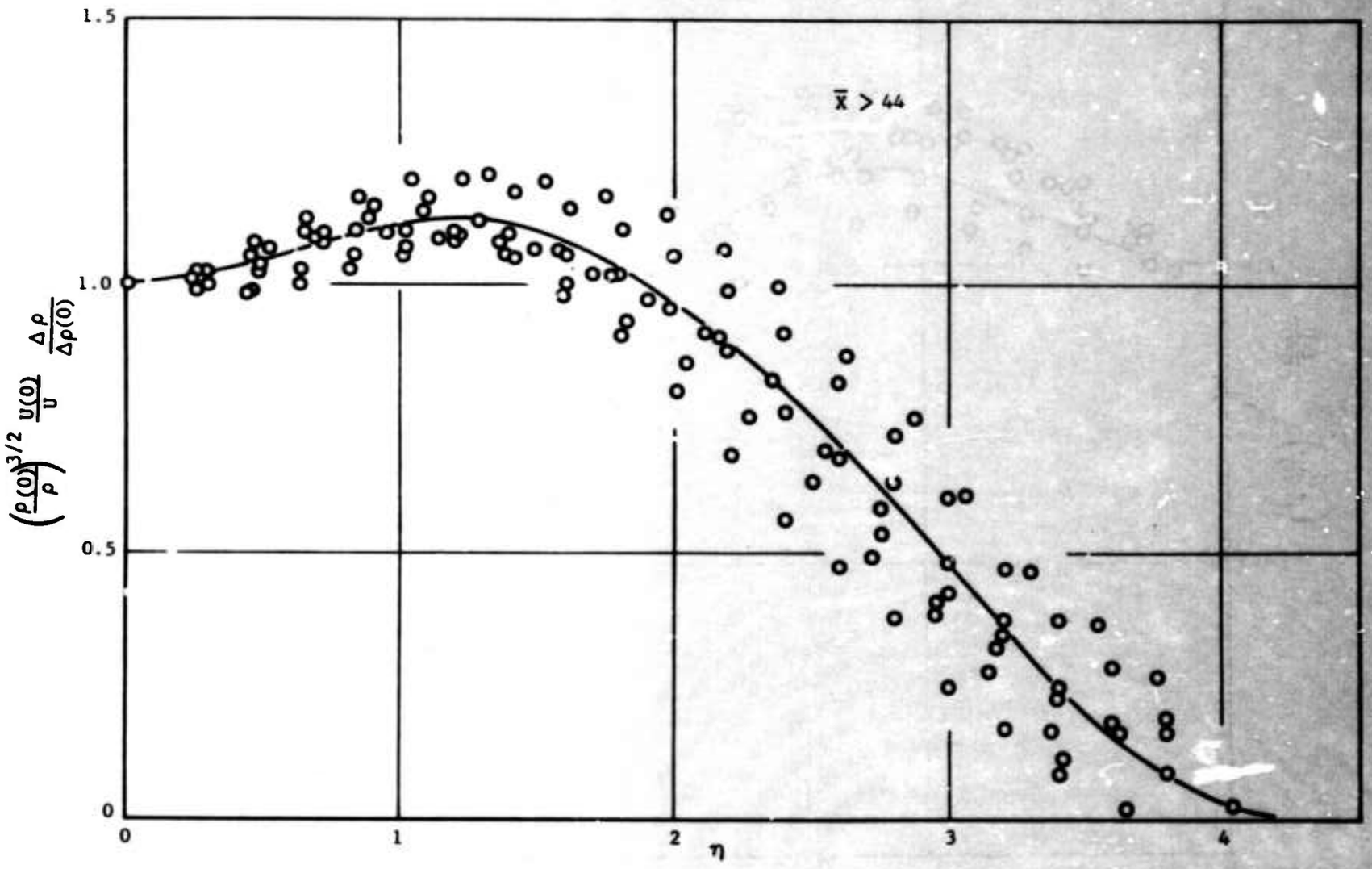

FIGURE 29. APPARENT SELF-PRESERVING FORM OF THE RMS DENSITY FLUCTUATIONS NORMALIZED ACCORDING TO THE DYNAMIC EQUILIBRIUM HYPOTHESIS.

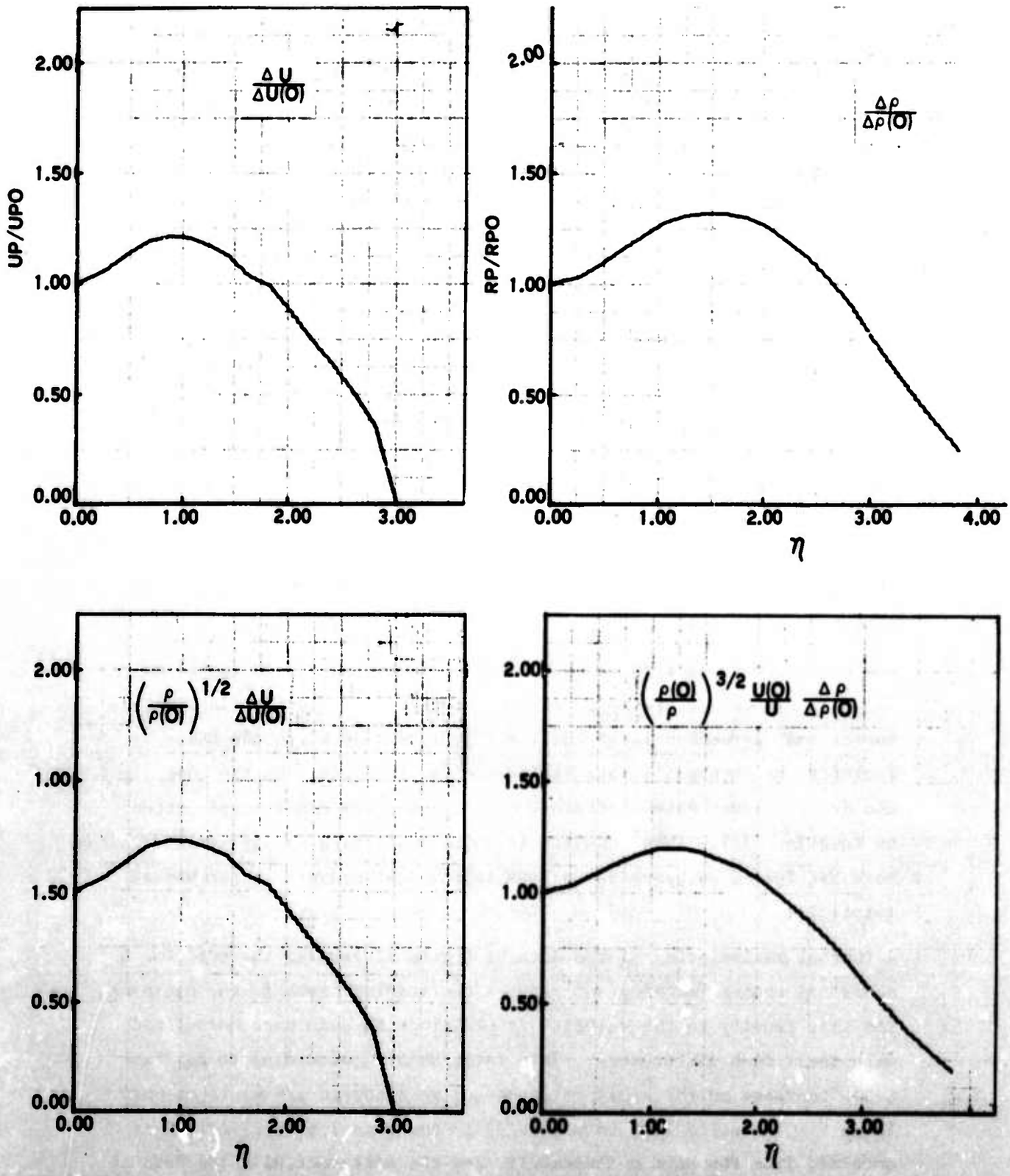

FIGURE 30. EFFECT OF PROPER COORDINATE TRANSFORMATION ON THE RADIAL FLUCTUATION DISTRIBUTION AT A TYPICAL AXIAL POSITION. IN THE TRANSFORMATION SUGGESTED BY THE DEH (BOTTOM) THE DISTRIBUTION MAXIMA IN THE VELOCITY AND DENSITY COME CLOSER IN MAGNITUDE AND POSITION.

plotted. Here the velocity and density fluctuations have been again plotted as in Figures 25, 26, 28, and 29; the shift in the peak is clear. In Figure 30, as in the previous illustrations, it is also clear that at higher η (near the wake edge), the distribution f differs between the velocity and density fluctuations. This is attributable to the effect of the intermittency.

According to Equation (67), the axis rms velocity fluctuations, normalized by the free-stream velocity u_∞ should decay as the (-2/3) power of $\bar{X}$ only if multiplied by the density factor $(1-r)^{1/2}$; such a plot is shown in Figure 31. The agreement with the predicted decay law is unsatisfactory; with the possible exception of the last few experimental points, the data decay faster than the (-2/3) power of $\bar{X}$, although, in fairness to the DEH, not as fast as the $\Delta u^{(o)}/u_\infty$ plot of Figure 23 indicates.

Better agreement obtains when the form of Equation (59) is tested as shown in Figure 32. In spite of the scatter, the velocity fluctuations normalized approach clearly the limit $\sqrt{g(o)} = 0.38$ which the DEH, fortified by Townsend's data (Reference 1), indicate. On the same figure, the density fluctuations attain the same numerical limit as predicted by Equation (79). This behavior is quite gratifying because the ordinates here are formed by grouping various independent measured experimental quantities.

A further manipulation of the data of Figure 32 removes the need for a numerical choice for g(o) and reduces the scatter: such is the ratio of the axis density to the velocity fluctuations in each case normalized with their mean differences. This ratio should, according to Equation (80), increase in the similar region and tend toward $1/S \simeq 1.18$ at very large $\bar{X}$. The solid line in Figure 33 is the quantity $(1-r)(1-w)/S$ as obtained from the mean measurements, and the agreement with the data is very good.

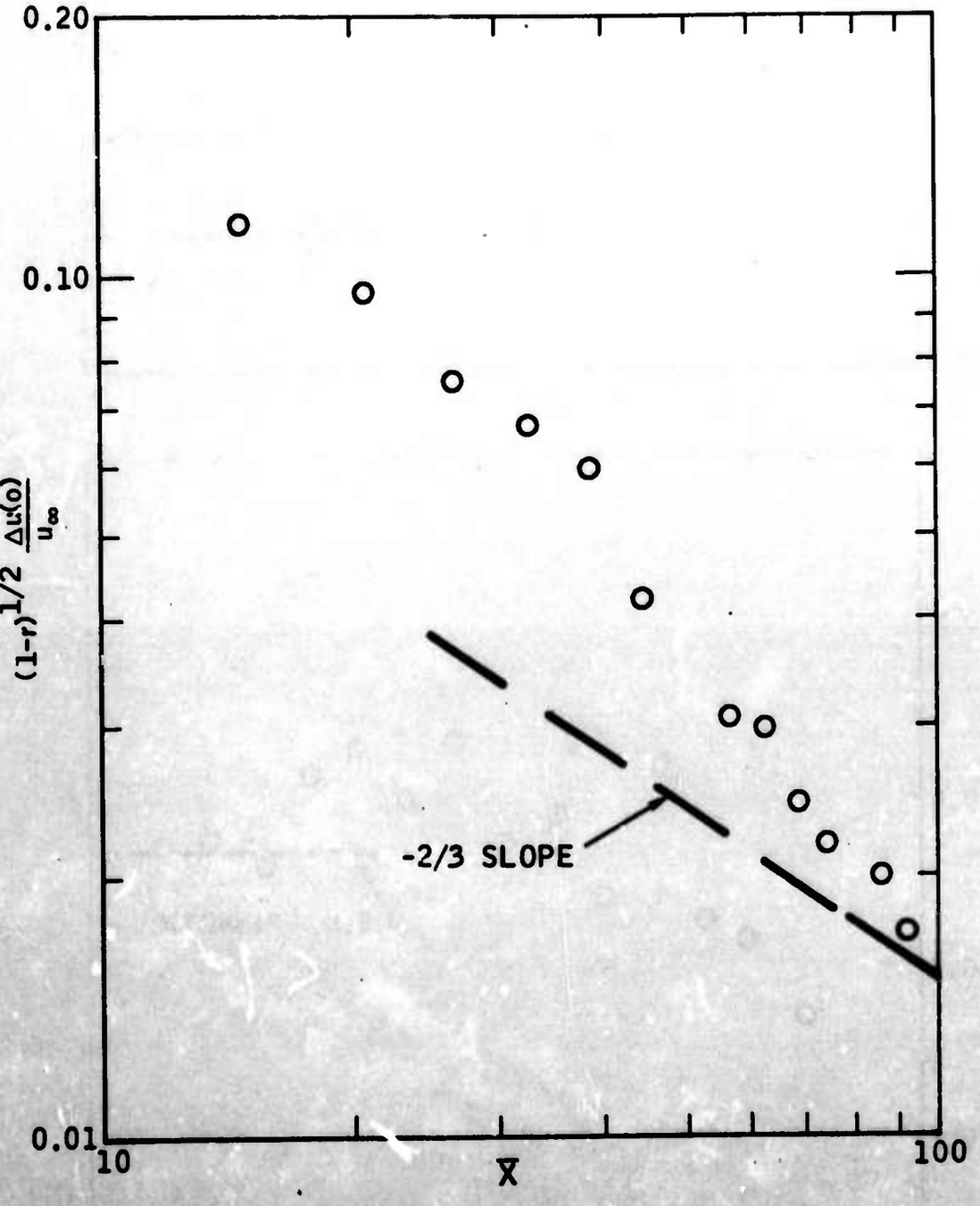

FIGURE 31. AXIAL VARIATION OF RMS AXIS VELOCITY FLUCTUATION NORMALIZED WITH THE EXTERNAL VELOCITY ACCORDING TO THE DYNAMIC EQUILIBRIUM HYPOTHESIS.

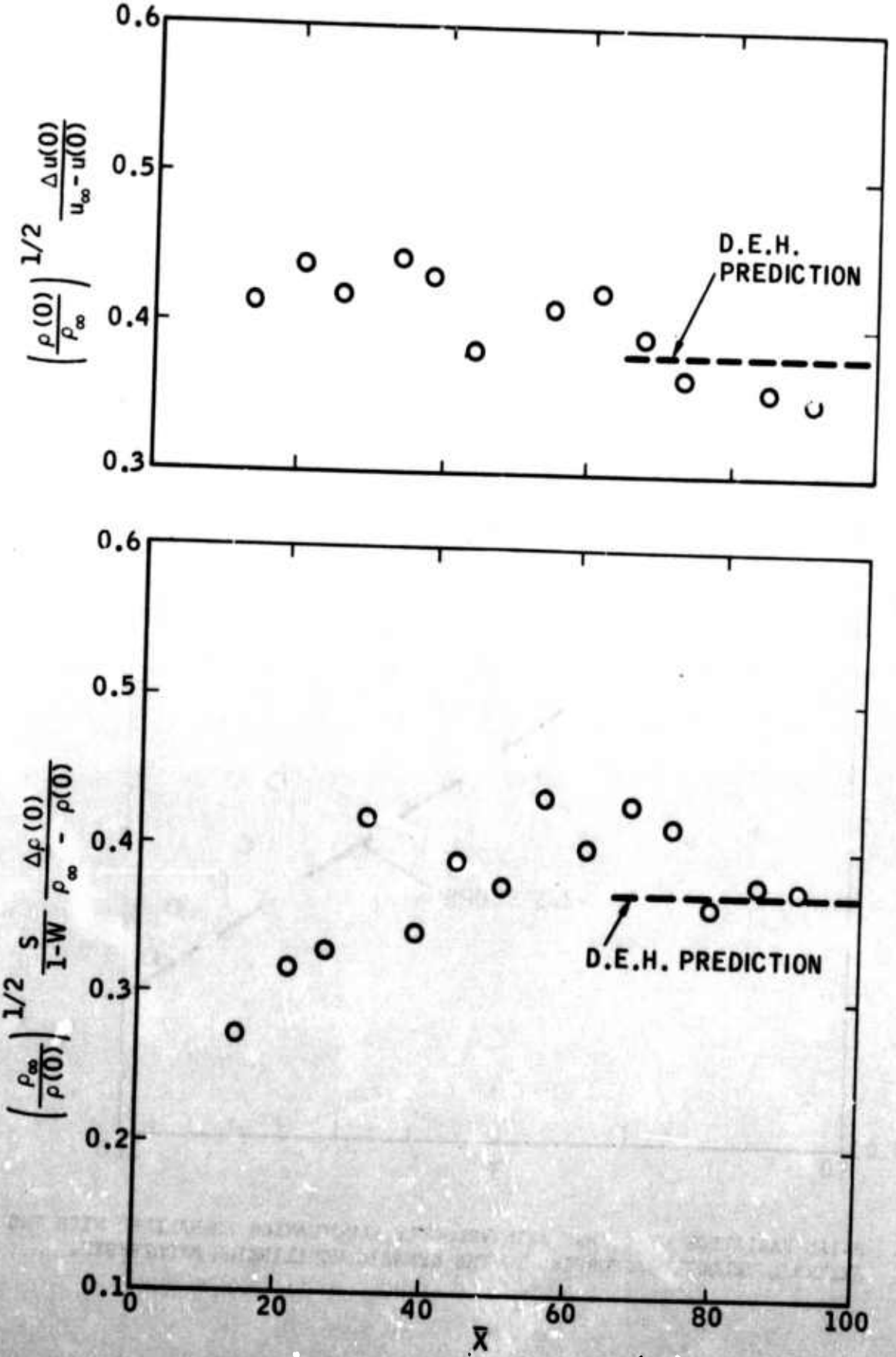

FIGURE 32. AXIAL VARIATION OF THE RMS AXIS VELOCITY (TOP) AND DENSITY (BOTTOM) FLUCTUATION NORMALIZED WITH THEIR RESPECTIVE DIFFERENCES ACROSS THE WAKE, ACCORDING TO THE DYNAMIC EQUILIBRIUM HYPOTHESIS.

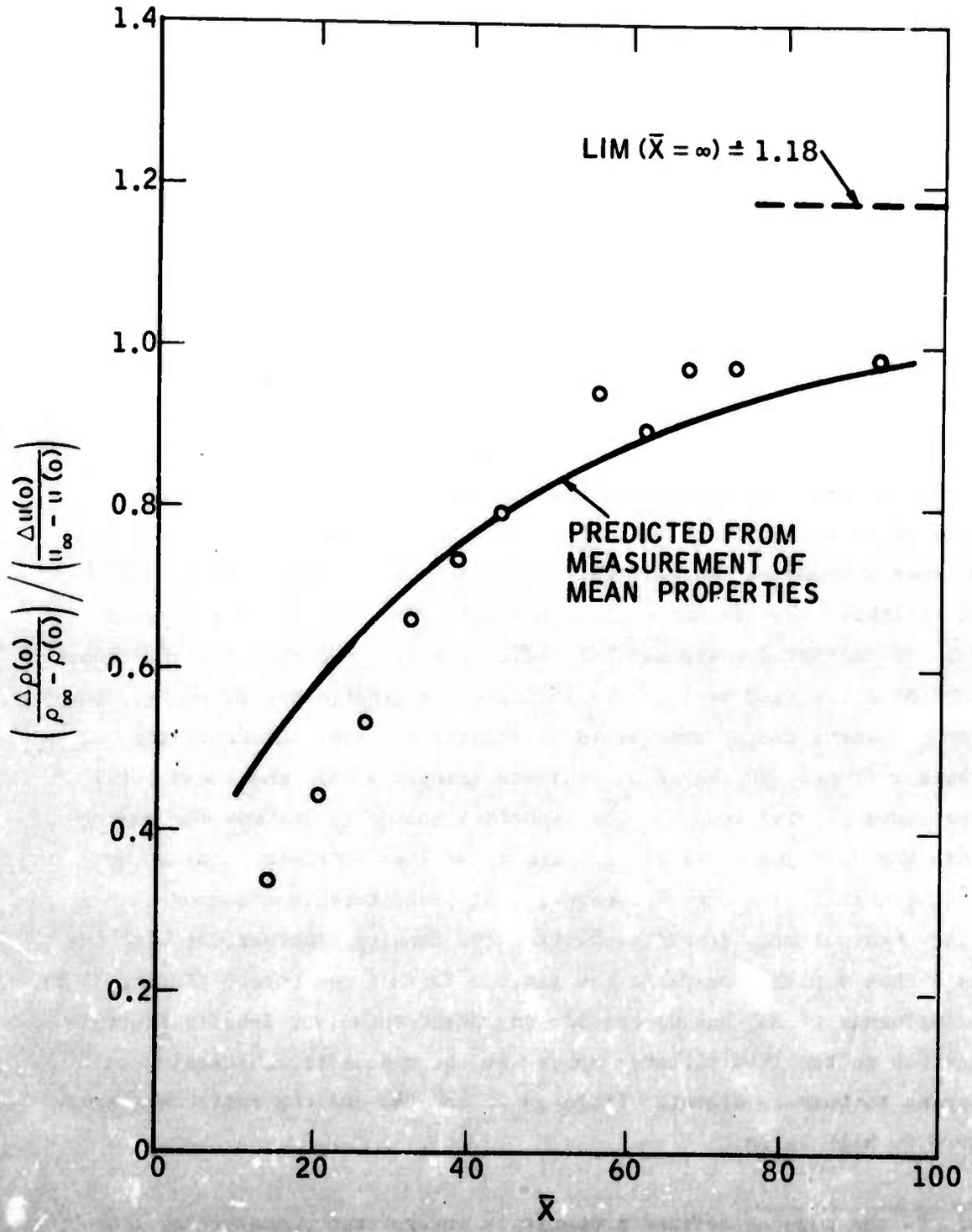

FIGURE 33. AXIAL VARIATION OF THE RATIO OF RMS AXIS DENSITY TO RMS AXIS VELOCITY FLUCTUATIONS.

The decay of the wake temperature fluctuation analogous to the velocity fluctuation decay of Figure 22 has been predicted on the basis of the strong Reynolds analogy (Equation (50)) and the relevant ratio is plotted versus $\bar{X}$ in Figure 34. Consistent with the small total temperature fluctuations found, this ratio tends toward unit (i.e., toward the verification of the analogy and of Equation (50)) at large values of $\bar{X}$. Note that in this and several previous illustrations, a relaxation distance of about 40 wake (drag) diameters is found, consistent with the mean-flow results (Reference 12). Other forms of the temperature fluctuation have not been plotted because the conversion of, say, $\Delta T(o)/T(o)$ to $\Delta T(o)/T_\infty$ is a simple matter.

In order to test the analogy in the radial direction, the ratio of Figure 34 is also plotted versus η in Figure 35. There are, in fact, two general types of behavior this ratio follows: nearer the base it peaks slightly towards unity about one-half the wake radius away from the axis; farther downstream, the ratio is very close to unity throughout except near the wake edge, where it increases greatly beyond unity. Both these pehnomena can be attributed to the intermittent nature of the turbulent front. In the first instance (Figure 35-a), the local total temperature fluctuations ΔT_o are important enough to destroy the analogy within the turbulence itself, and the ratio lies sensibly below unity. Near the actual wake edge,* however, that pseudoturbulent component due to the intermittency itself emphasizes the density fluctuations with the result that a peak appears in the ratio. Farther downstream (Figure 35-b), the influence of ΔT_o has decreased, but pseudoturbulent density fluctuations due to the intermittency appear at the wake edge, thickening the apparent turbulence diameter (Figures 28 and 29) and the ratio is thereby driven to high value.

*This is the edge as defined properly by intermittency measurements, which will be described in a later report.

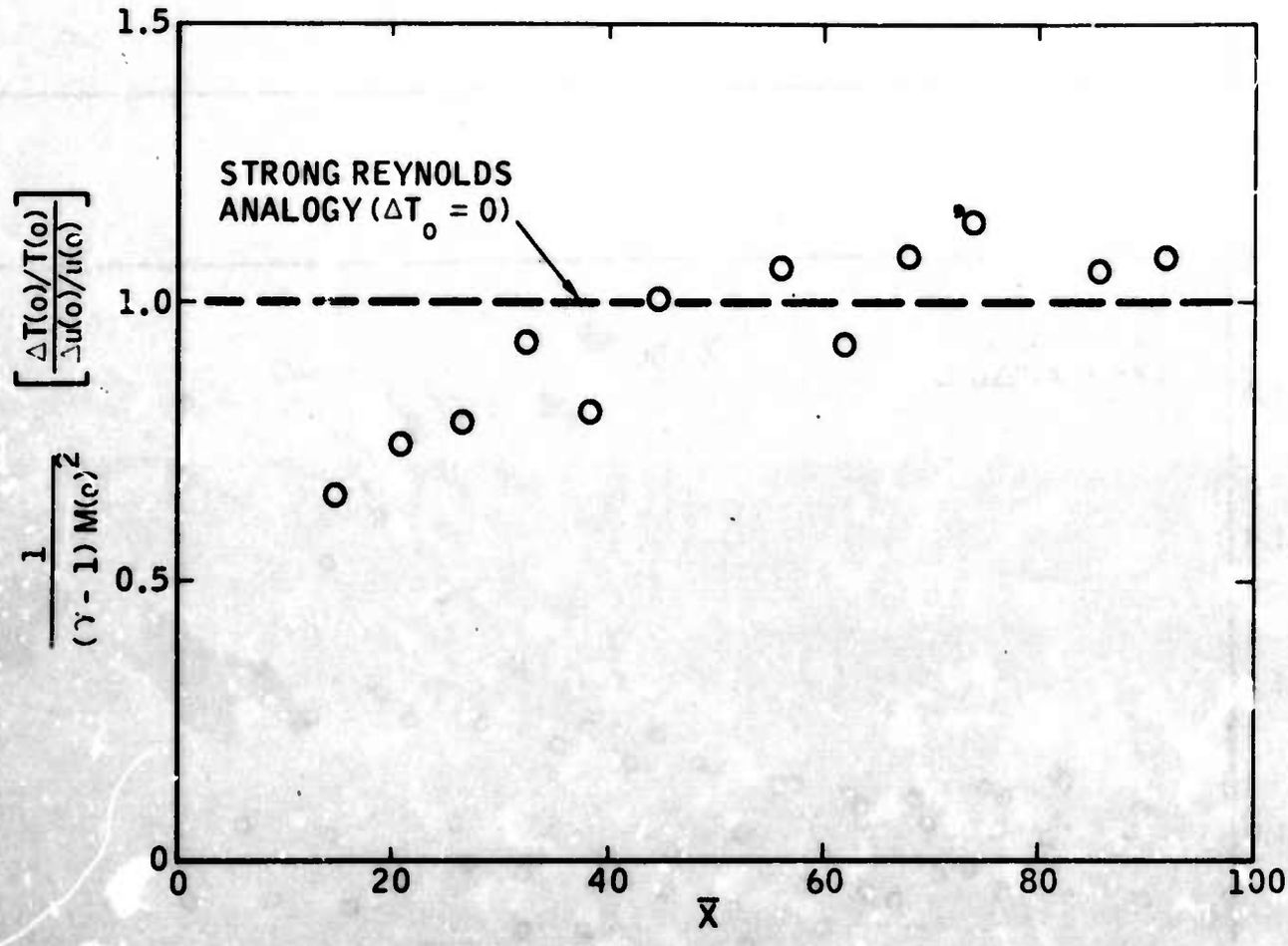

FIGURE 34. AXIAL VARIATION OF THE RATIO OF RMS AXIS TEMPERATURE TO RMS AXIS VELOCITY FLUCTUATIONS.

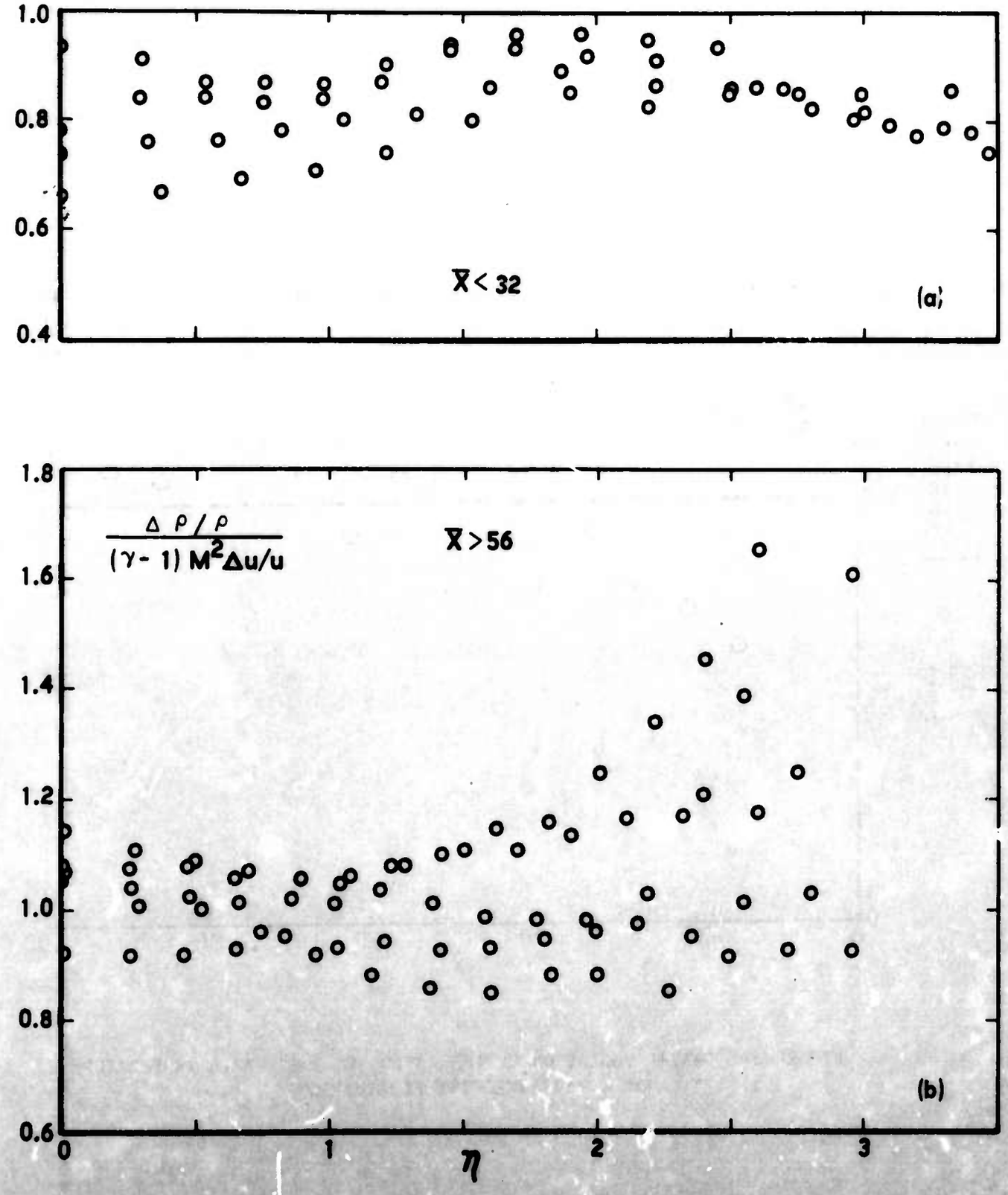

FIGURE 35. TEST OF THE "STRONG REYNOLDS ANALOGY" FOR THE RELAXING (TOP) AND THE SELF-PRESERVING WAKE (BOTTOM).

SECTION 6

INTEGRAL SCALES

The integral scales of axial velocity and temperature (density) were computed by the WEB-VII program (Appendix E) as a function of position, according to the scheme of Equations (47) and (48). The results are shown in Figures 36 through 39. As already discussed in Paragraph 4.1, there are intuitive arguments that the integral scales (i.e., the autocorrelation macroscales) should be locally proportional to the characteristic length, L, of the wake and thus grow with the 1/3 power of axial distance. To date, however, no information has existed on the numerical differences between the density (temperature) macroscale, Λ_S, and the axial velocity macroscale, Λ_T or their radial variation.

Figure 36 shows the variation of the axis values of the Λ_S normalized alternately with $\sqrt{C_D A}$ and with L. There is little doubt that on the axis the ratio Λ_S/L is constant in the similar region of the wake,

$$\frac{\Lambda_S}{L} \quad (\eta = 0) \quad = \quad 0.48$$

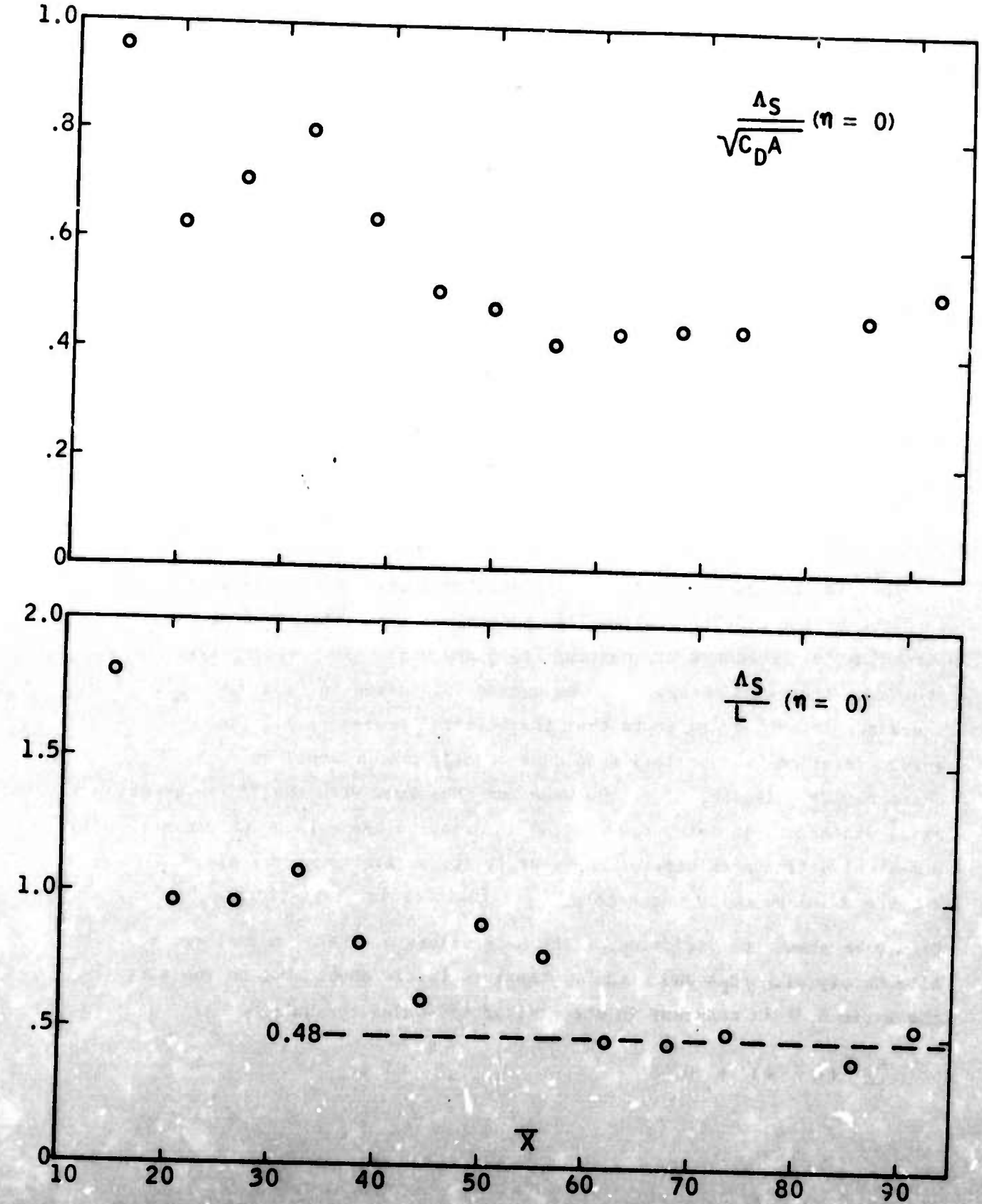

FIGURE 36. AXIAL VARIATION OF LONGITUDINAL DENSITY FLUCTUATION INTEGRAL AUTOCORRELATION SCALE ON THE AXIS NORMALIZED WITH THE VIRTUAL WAKE DIAMETER (TOP) AND THE TRANSVERSE WAKE SCALE (BOTTOM).

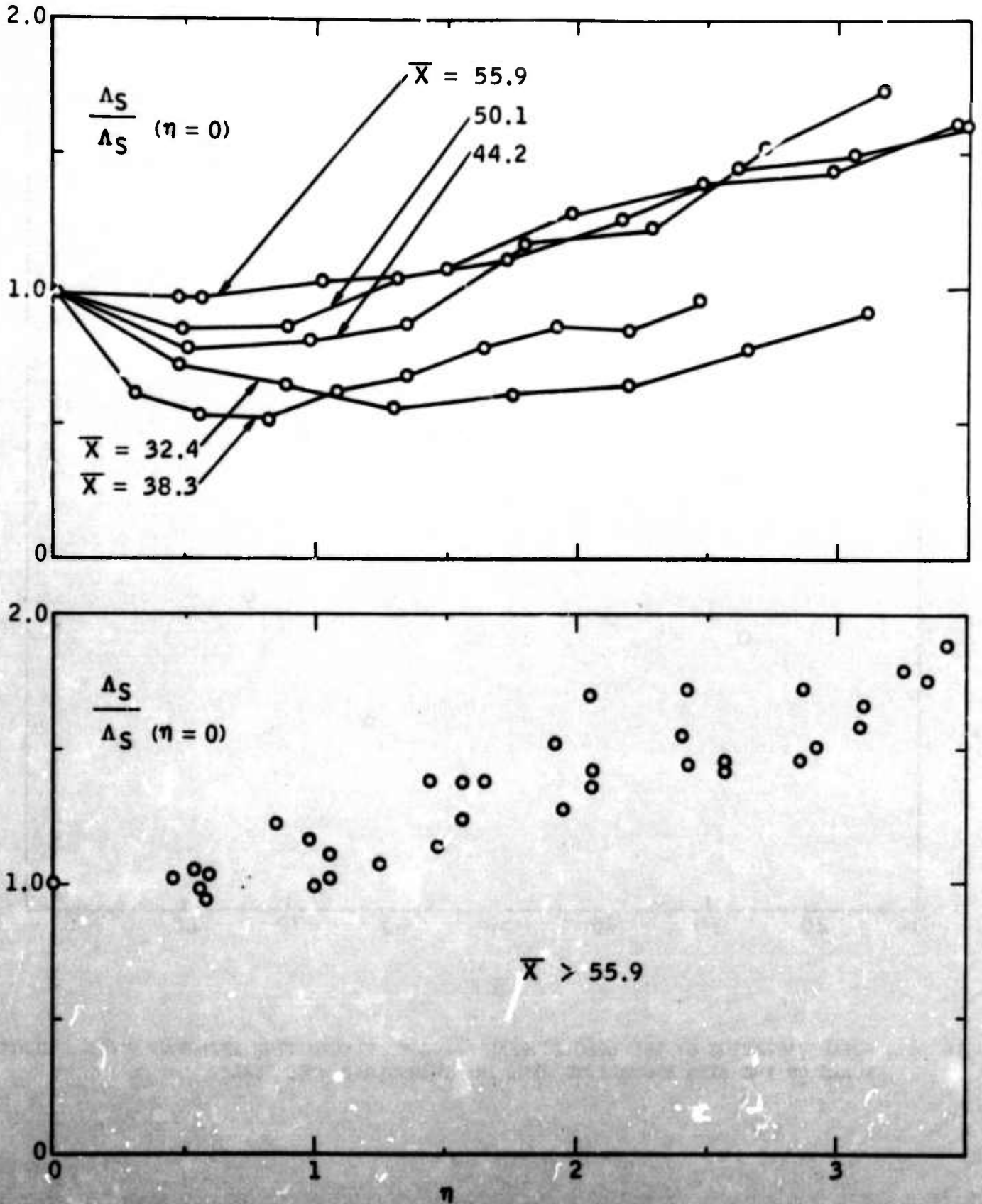

FIGURE 37. RADIAL VARIATION OF THE LONGITUDINAL DENSITY FLUCTUATION INTEGRAL AUTOCORRELATION SCALE, NORMALIZED WITH THE AXIS VALUE IN THE RELAXING (TOP) AND THE SELF-PRESERVING WAKE (BOTTOM).

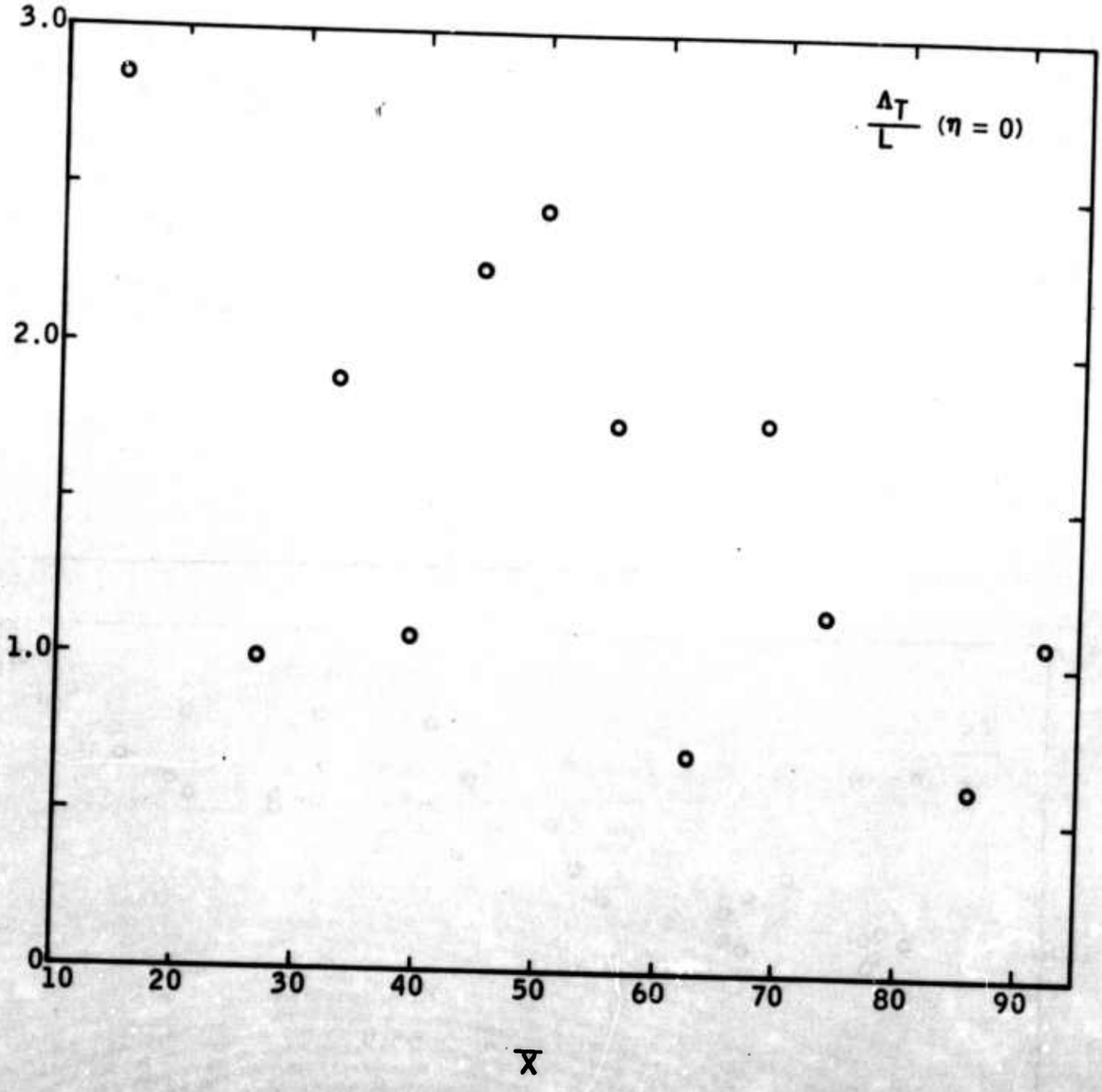

FIGURE 38. AXIAL VARIATION OF THE LONGITUDINAL VELOCITY FLUCTUATION INTEGRAL AUTOCORRELATION SCALE ON THE AXIS NORMALIZED WITH THE TRANSVERSE WAKE SCALE.

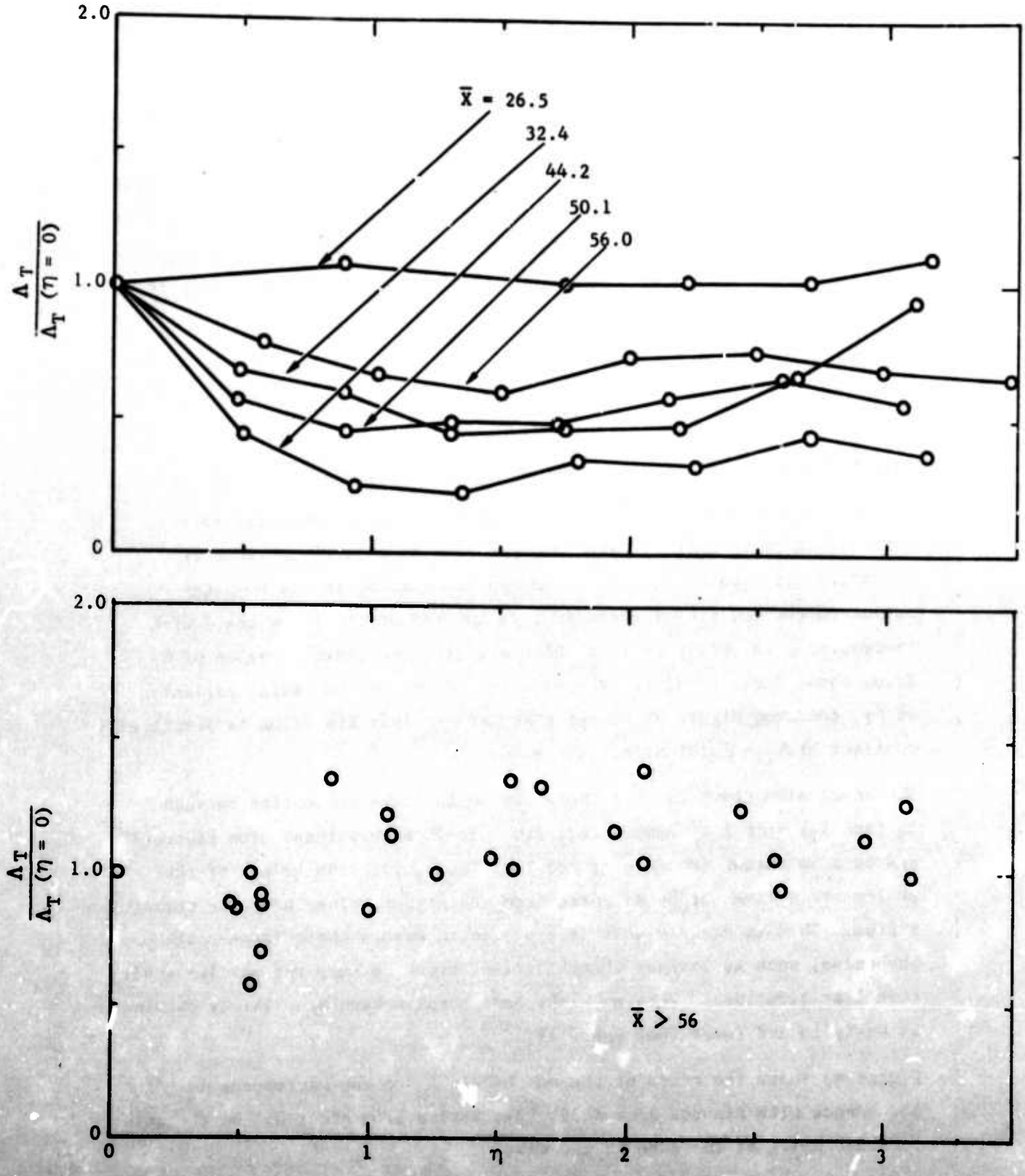

FIGURE 39. RADIAL VARIATION OF THE LONGITUDINAL VELOCITY FLUCTUATION INTEGRAL AUTOCORRELATION SCALE, NORMALIZED WITH THE AXIS VALUE IN THE RELAXING (TOP) AND THE SELF-PRESERVING WAKE (BOTTOM).

The radial variation of Λ_s is shown in Figure 37. Immediately downstream of the transition zone, the density macroscale decreases to a minimum off the axis and, in fact, attains a value as small as $0.5\Lambda(\eta = o)$. Beyond that the scale increases systematically with distance, and in the similar portion ($\overline{X} > 55.9$) it increases linearly from the axis to the apparent edge of the wake where $\Lambda_S = 2\Lambda_S(\eta = o)$. In terms of the transverse scale, L, this implies

$$\Lambda_S(\eta = o) = 0.5\ L$$

$$\Lambda_S(\eta = 3.5) = L$$

with a linear variation in between.

As seen in Figure 38, the axis variation of the axial velocity auto-correlation macroscale Λ_T cannot be pictured effectively because of excessive data scatter due in large part to scatter in the computer output in the velocity spectra at very low frequencies; the trend with increasing $\overline{X}$ is fairly obvious, however, with the limiting value of Λ_T lying between 0.5 L and L. There is less doubt on the radial variation of Λ_T, and from Figure 39 we see that here in fact its value is practically constant at $\Lambda_T = \Lambda_T(o)$ across the wake.

The conclusion drawn is that the expected intimate connection between Λ_S (and Λ_T) with L is indeed verified. It is also evident from Figure 36, and to some extent from Figure 38) that the equilibrium values of the scales are arrived at by decrease from the higher values near the transition region. This is exactly what is expected in events where large-scale phenomena, such as laminar instabilities, break up into the smaller scale turbulent structure. Very much the same results have been lately obtained by Gaviglio and Favre (Reference 19).

Figure 40 shows the ratio of the macroscale Λ_S to the macroscale Λ_T. In accordance with Figures 37 and 39, this varies from about 0.5 on the axis to about unity at the edge of the wake.

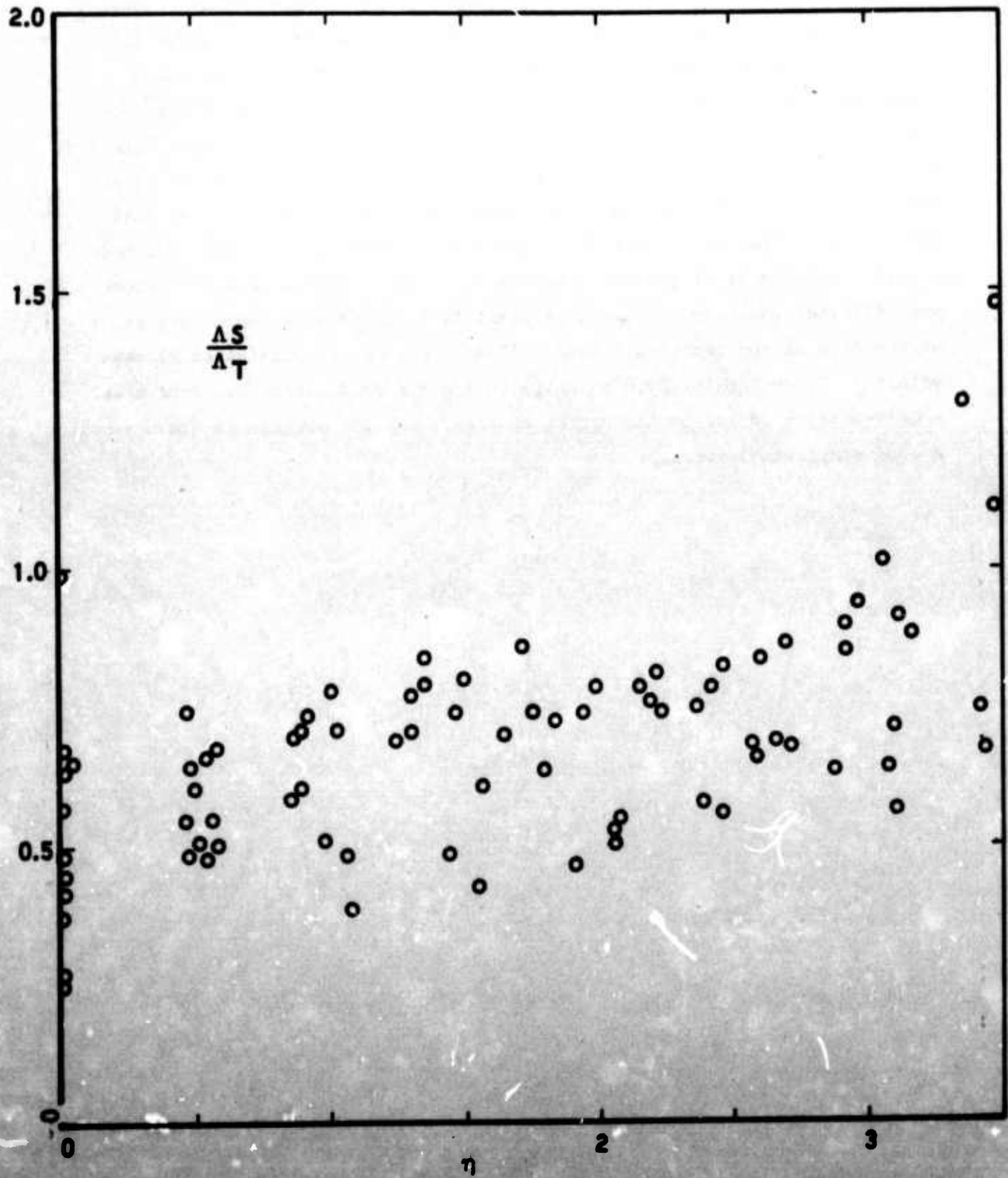

FIGURE 40. RADIAL VARIATION OF THE RATIO OF THE DENSITY TO THE VELOCITY SCALE

An important byproduct of the scale measurement is the reassurance that the experimental conditions are capable of producing valid statistical averages. The validity condition obviously is that the hot-wire samples a sufficiently large number of macroscale-size eddies during its exposure to the local turbulent flow. In this experiment, such local conditions are (for expediency) measured by traversing the wire radially across the wake (cf. Figure 7) and then by processing the data once all the necessary traverses are taken. The question therefore arises as to whether the traverse speed is so fast that the wire does not remain at any particular point in the wake to sample a sufficient number of eddies. Each traverse lasts approximately 10 seconds, implying that the wire remains approximately 1 second in a radial segment of the size of the macroscale (about 1 mm). For the prevailing axial mean velocity of, typically, 50,000 centimeters per second, there are thus about a half-million eddies in the aggregate from which the average is drawn -- a good statistical average.

SECTION 7

SPECTRAL-MODAL ANALYSIS

We shall now present the results of the spectral-modal analysis wherein the distribution of fluctuation intensities will be further expanded into its Fourier contributions. Before discussing these results, we will utilize the typical datum from the WEB-VII program output, shown in Figure 41, in order to define terms, dimensions and units.

There are three main representations of interest for each mode and at each point in the wake. First, we want to know how much of the total hot-wire signal is due to density and how much is due to axial velocity fluctuations. Thus, within a 1-kilocycle-per-second passband around each frequency, we define by $\sigma(f)$ the root-mean-square density fluctuation contribution (normalized with the local mean density) and by $\tau(f)$ the corresponding contribution of the velocity fluctuation. Referring to Figure 41, these results are shown on the second and third columns as a function of the frequency, shown in the first column. The units of these quantities are $(\text{kcps})^{-1}$; to convert these to $(\text{cps})^{-1}$, i.e., seconds, one divides by 1000, and this has been done in the illustrations plotting these quantities. The fourth column lists the spectrally resolved cross-correlation coefficient of density and velocity, which is of course nondimensional.

WEB-7 OUTPUT

WAKE STATISTICS

A. DEMETRIADES

X STATION 4.2982 UPRIME(0) 0.500600+000 RHOPRIME(0) 0.369035+000 Y STATION 0.900000-001 ETA 0.413269+000

LAMBDA T 0.850921-001 LAMBDA S 0.702652-001 SUM SIGMA2 0.467273-001 SUM TAU2 0.933589-002 [illegible] 0.545543+000

LAMBDA S1 0.415770+000 LAMBDA S2 0.325306+000 LAMBDA T1 0.503503+000 LAMBDA T2 0.393945+000

F(CpS)	TAU*	SIGMA*	RSTAU*	TAU*/ SIGMA*	TAU*2/ SUM TAU2	SIGMA*2/ SUM SIGMA2	S2/ S2(0)	T2/ T2(0)	[illegible]T	MS
7000.	0.7367-002	0.1490-001-0.9403+000		0.4919+000	0.5813-002	0.4808-002	0.1000+001	0.1000+001	0.1017-001	0.8400-002
14000.	0.7940-002	0.1606-001-0.9452+000		0.4945+000	0.6753-002	0.5517-002	0.1149+001	0.1162+001	0.2035-001	0.1680-001
21000.	0.8170-002	0.1684-001-0.9467+000		0.4850+000	0.7149-002	0.6072-002	0.1265+001	0.1230+001	0.3052-001	0.2520-001
28000.	0.8690-002	0.1792-001-0.9493+000		0.4848+000	0.8088-002	0.6876-002	0.1432+001	0.1391+001	0.4069-001	0.3360-001
35000.	0.9263-002	0.1903-001-0.9508+000		0.4867+000	0.9190-002	0.7751-002	0.1615+001	0.1561+001	0.5086-001	0.4200-001
42000.	0.9918-002	0.2018-001-0.9523+000		0.4912+000	0.1092-001	0.8711-002	0.1815+001	0.1810+001	0.6104-001	0.5040-001
49000.	0.1016-001	0.2078-001-0.9513+000		0.4896+000	0.1105-001	0.9211-002	0.1919+001	0.1902+001	0.7121-001	0.5880-001
56000.	0.9658-002	0.2037-001-0.9487+000		0.4742+000	0.9991-002	0.8877-002	0.1849+001	0.1719+001	0.8138-001	0.6720-001
63000.	0.8902-002	0.1940-001-0.9434+000		0.4589+000	0.8488-002	0.8054-002	0.1678+001	0.1460+001	0.9155-001	0.7560-001
70000.	0.8582-002	0.1866-001-0.9380+000		0.4600+000	0.7888-002	0.7449-002	0.1552+001	0.1357+001	0.1017+000	0.8400-001
77000.	0.7502-002	0.1722-001-0.9341+000		0.4404+000	0.6158-002	0.6343-002	0.1322+001	0.1059+001	0.1119+000	0.9240-001
84000.	0.7016-002	0.1626-001-0.9332+000		0.4315+000	0.5272-002	0.5659-002	0.1179+001	0.9870+000	0.1221+000	0.1008+000
91000.	0.6486-002	0.1508-001-0.9248+000		0.4302+000	0.4506-002	0.4864-002	0.1013+001	0.7751+000	0.1322+000	0.1092+000
98000.	0.6036-002	0.1419-001-0.9204+000		0.4253+000	0.3902-002	0.4309-002	0.8978+000	0.6713+000	0.1424+000	0.1176+000
105000.	0.5431-002	0.1337-001-0.9226+000		0.4064+000	0.3160-002	0.3823-002	0.7965+000	0.5436+000	0.1526+000	0.1260+000
112000.	0.5302-002	0.1289-001-0.9181+000		0.4114+000	0.3011-002	0.3555-002	0.7407+000	0.5180+000	0.1628+000	0.1344+000
119000.	0.4401-002	0.1189-001-0.9263+000		0.3701+000	0.2074-002	0.3025-002	0.6302+000	0.3568+000	0.1729+000	0.1428+000
126000.	0.4760-002	0.1186-001-0.9161+000		0.4014+000	0.2427-002	0.3010-002	0.6270+000	0.4175+000	0.1831+000	0.1512+000
133000.	0.4363-002	0.1138-001-0.9219+000		0.3860+000	0.2039-002	0.2735-002	0.5697+000	0.3508+000	0.1933+000	0.1596+000
140000.	0.4053-002	0.1086-001-0.9302+000		0.3732+000	0.1759-002	0.2524-002	0.5258+000	0.3026+000	0.2035+000	0.1680+000
161000.	0.3934-002	0.9947-002-0.9183+000		0.3955+000	0.1658-002	0.2118-002	0.4412+000	0.2852+000	0.234 +000	0.1932+000
182000.	0.3508-002	0.8845-002-0.9046+000		0.3966+000	0.1318-002	0.1674-002	0.3488+000	0.2267+000	0.2645+000	0.2184+000
210000.	0.3004-002	0.7919-002-0.9359+000		0.3794+000	0.9667-003	0.1342-002	0.2796+000	0.1663+000	0.3052+000	0.2520+000
245000.	0.3098-002	0.6938-002-0.9181+000		0.4465+000	0.1028-002	0.1030-002	0.2146+000	0.1768+000	0.3560+000	0.2940+000
280000.	0.2361-002	0.5788-002-0.9390+000		0.4080+000	0.5973-003	0.7168-003	0.1493+000	0.1027+000	0.4069+000	0.3360+000
315000.	0.1575-002	0.4427-002-0.9754+000		0.3559+000	0.2658-003	0.4194-003	0.8737-001	0.4573-001	0.4578+000	0.3780+000
350000.	0.1184-002	0.3579-002-0.9780+000		0.3304+000	0.1902-003	0.2443-003	0.5090-001	0.2583-001	0.5086+000	0.4200+000
385000.	0.	0.2093-002 0.		0.	0.	0.9378-004	0.1954-001	0.	0.5593+000	0.4620+000
420000.	0.1073-002	0.1996-002-0.9910+000		0.5374+000	0.1232-003	0.8526-004	0.1776-001	0.2120-001	0.6104+000	0.5040+000
490000.	0.	0. 0.		0.	0.	0.	0.	0.	0.7121+000	0.5880+000

FIGURE 41. TYPICAL OUTPUT FROM THE WEB-VII PROGRAM.

A second representation of fundamental importance gives the fraction of the total fluctuation magnitude which is contained in the passband at hand. Thus, $\sigma^2(f)/\sigma^2$ is the ratio of the mean-square density fluctuation magnitude $\sigma^2(f)$ in the 1-kilocycle-per-second passband around the frequency f, to the total (frequency-integrated) mean-square density fluctuation σ^2 at the same point in the wake; note that the connection between $\sigma(f)$ and σ (and also $\tau(f)$ and τ) have been given by Equations (42) through (46). This ratio, and the corresponding ratio $\tau^2(f)/\tau^2$, are found in the sixth and seventh columns of Figure 41. Again, the units here are in $(kcps)^{-1}$ or milliseconds.

One can employ the third representation, shown in the eighth and ninth columns, to compare the spectra by the expedient of normalizing the spectral densities by their respective zero-frequency limits. These normalized spectral densities are then dimensionless and are denoted as $\sigma^2(f)/\sigma^2(0)$ and $\tau^2(f)/\tau^2(0)$. In this form the spectra can be compared with the customary one-dimensional spectral density descriptions such as shown in Reference 18. To this end, the last two columns of Figure 41 also show appropriate nondimensionalizations of the frequency into the forms

$$n_T = \frac{f\Lambda_T}{u} \tag{90}$$

$$n_S = \frac{f\Lambda_S}{u} \tag{91}$$

where Λ_T and Λ_S are the respective integral scales and u is the local mean velocity.

With this introduction, the numerous illustrations shown of spectral densities are self-explanatory. In drawing comparisons and conclusions it should be noted that, in the axial direction, we should normally look for an evolutionary adjustment of the spectra within the relaxation zone ($\bar{X} \leq 40$) and perhaps an invariant behavior in the region of self-preservation. In the radial direction, we draw guidelines from the results of the modal analysis and the unpublished results of the intermittency measurements. Thus we are interested in the following regions: (1) the wake axis (η=0), where the

fluid is fully turbulent, (2) the region of maximum shear (η = 1.1) which coincides with, and obviously gives rise to, the maxima in the fluctuation magnitudes (compare Figures 28 and 29), (3) the location, in the statistical sense, of the wake front (η = 2.11), and (4) the wake edge which can be conveniently defined as the point at which the mean velocity distribution $\tilde{u}$ is 1 percent of its axis value (i.e., 0.01) and which is thus located (Reference 12) at η = 3.28.

A good first look of the distribution of spectral densities is given by Figures 42 and 43. These serve to bring out the unusual feature of a fluctuation concentration (peak) at a scale which, from Figure 42, is about 6 times and, from Figure 43, about 12 times the integral scales. In Figure 42, drawn from the relaxation zone ($\bar{X}$ = 26.5) and in Figure 43, taken from the self-preserving region ($\bar{X}$ = 56.0), this peak is generally absent from the axis and the wake edge and seems to become most intense in the region $1 < \eta < 2$, i.e., between the maximum shear and the front location. We shall return to the discussion of this feature in the comments which follow.

Turning to the spectra on the axis, Figure 44 shows that, initially, the wire signal is predominated by velocity fluctuations uniformly greater than the density fluctuations at all frequencies; farther downstream, of course, the situation is reversed (as the modal analysis has already shown), although at $\bar{X}$ = 61.9 the preponderance of the density fluctuations is mainly due to the larger eddies. In the same vein, consider the results at $\bar{X}$ = 26.5 of Figure 45. Here $\sigma \simeq T$, but the velocity predominates at the lower frequencies, with the density taking over a range of higher frequencies. Figure 46 shows that the density fluctuation density (in terms of fraction of the total local density fluctuation) is distributed with frequency in a way independent of axial position, and this similarity becomes quite remarkable, in fact, when the spectra are normalized in the manner of Figure 47. By contrast to the latter, which presents data beyond $\bar{X}$ = 56, consider that the density spectral shape is much more scattered in the

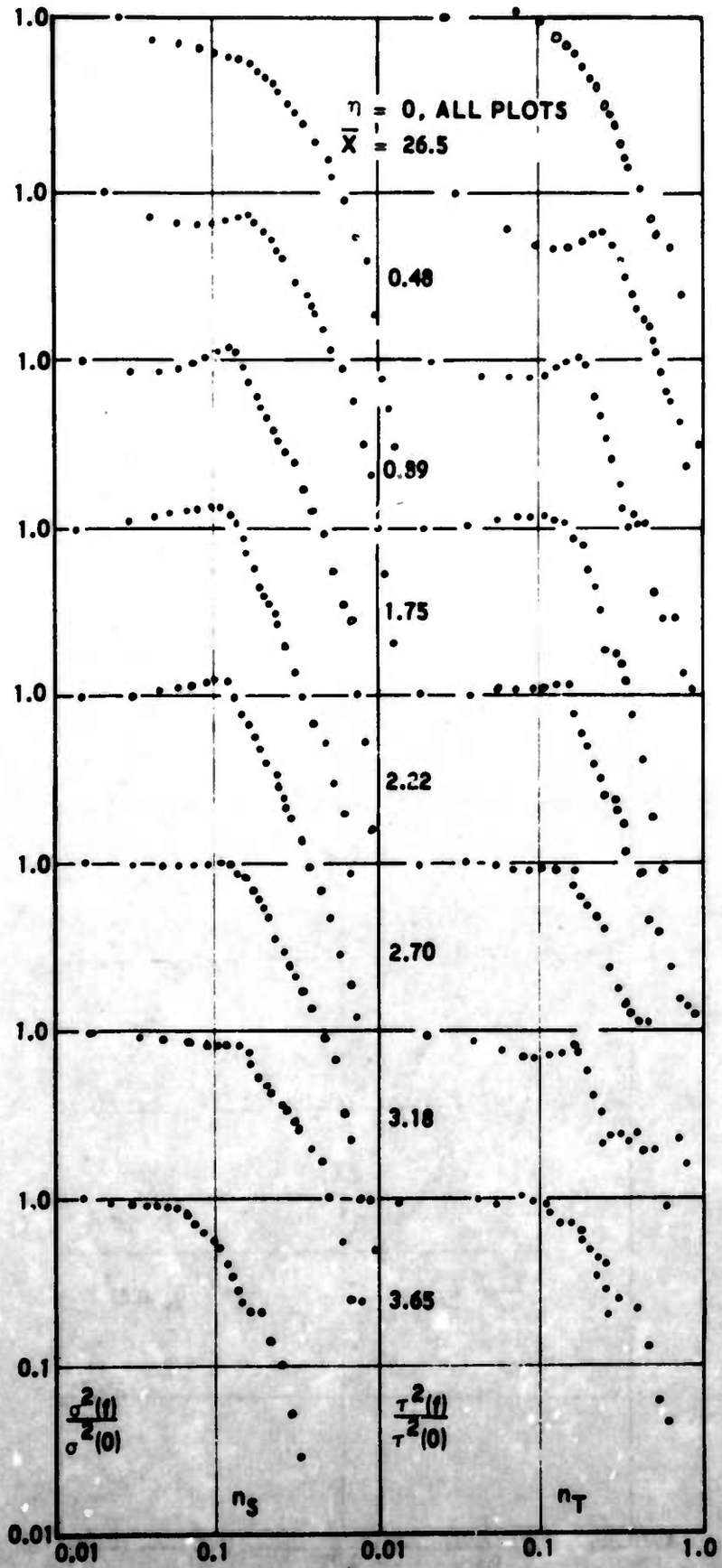

FIGURE 42. RADIAL VARIATION OF THE LONGITUDINAL SPECTRA OF MEAN-SQUARE DENSITY (LEFT) AND VELOCITY (RIGHT) FLUCTUATIONS (NORMALIZED AT ZERO FREQUENCY) SOON AFTER TRANSITION TO TURBULENCE.

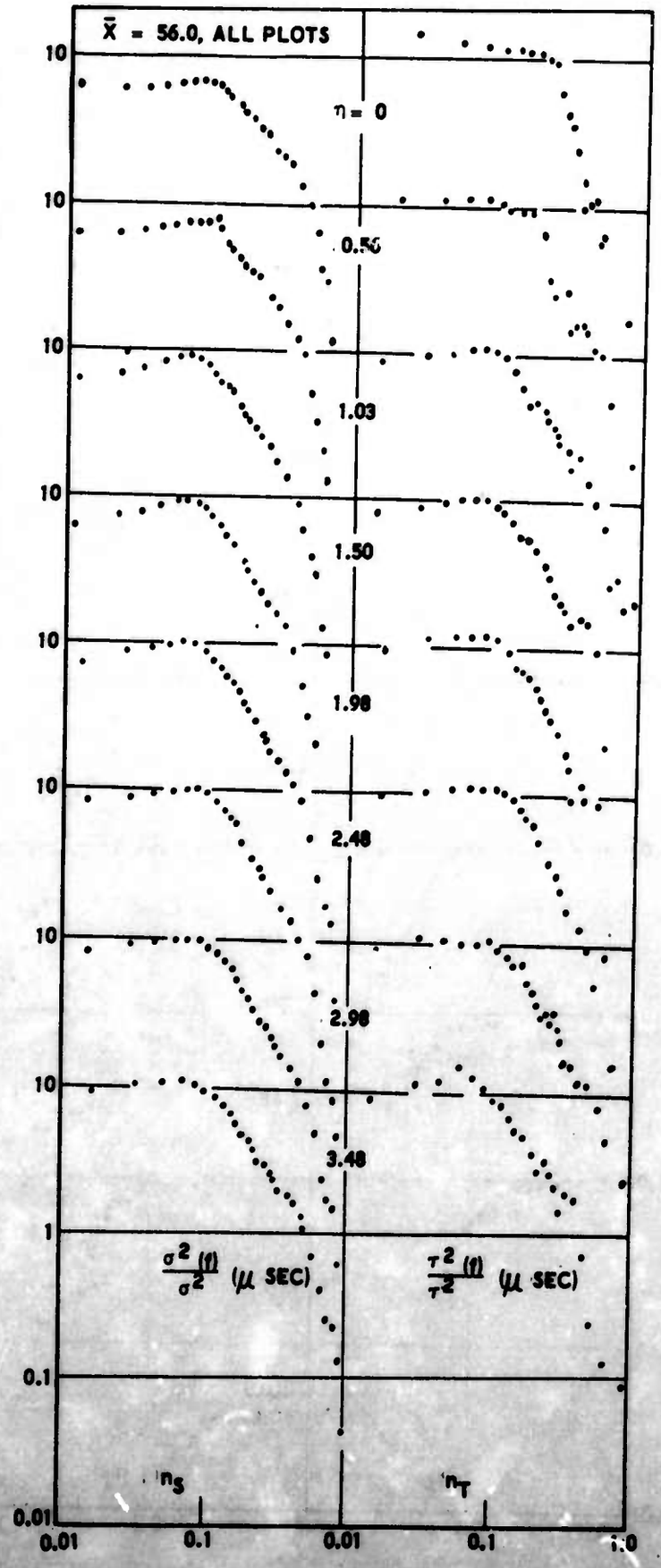

FIGURE 43. RADIAL VARIATION OF THE LONGITUDINAL SPECTRA OF MEAN-SQUARE DENSITY (LEFT) AND VELOCITY (RIGHT) FLUCTUATIONS (NORMALIZED WITH THE INTEGRATED FLUCTUATIONS) IN THE SELF-PRESERVING WAKE.

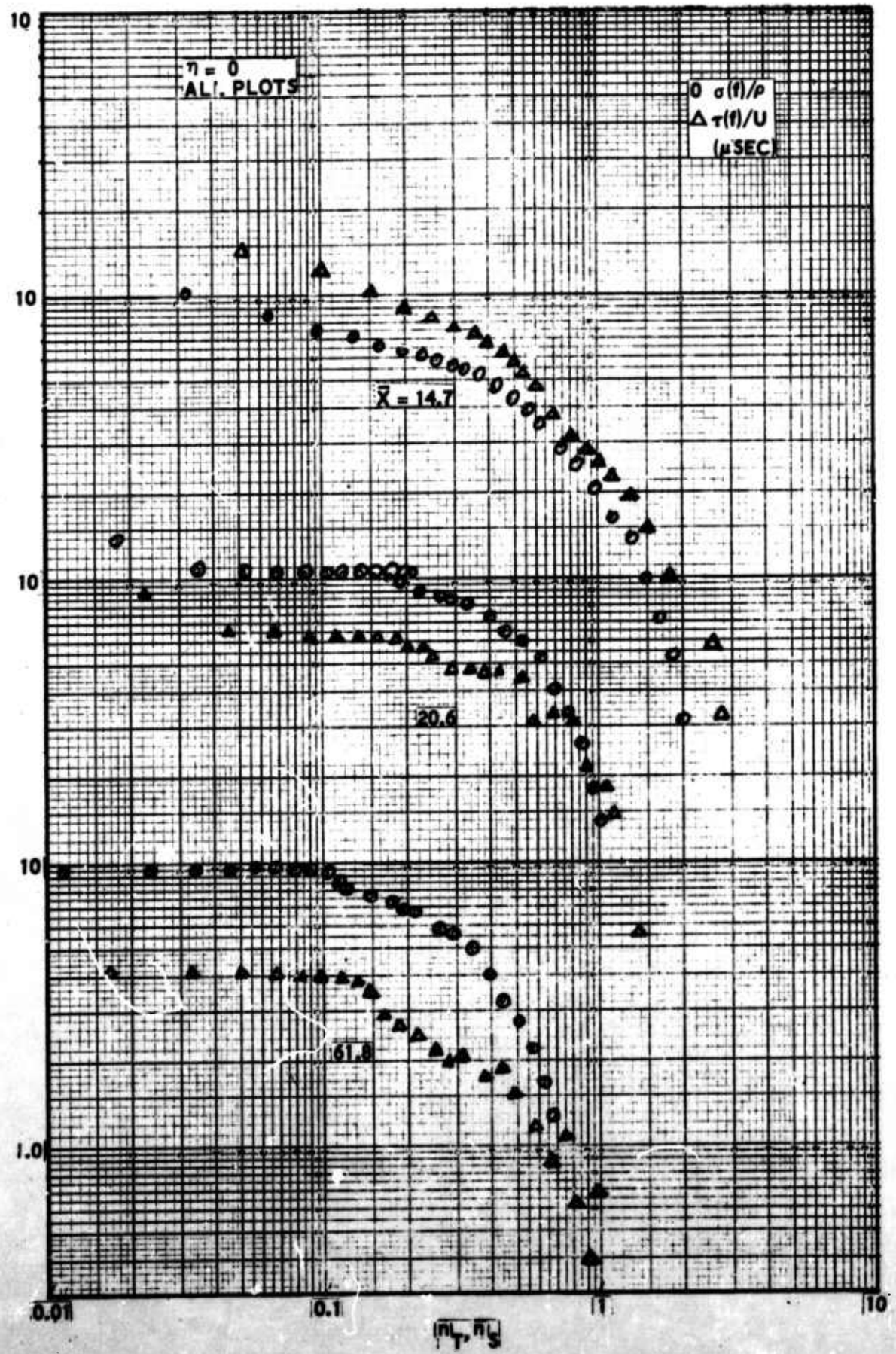

FIGURE 44. AXIAL EVOLUTION OF THE LONGITUDINAL SPECTRA OF RMS DENSITY AND VELOCITY FLUCTUATIONS (NORMALIZED WITH THE LOCAL MEAN VALUES) ON THE WAKE AXIS.

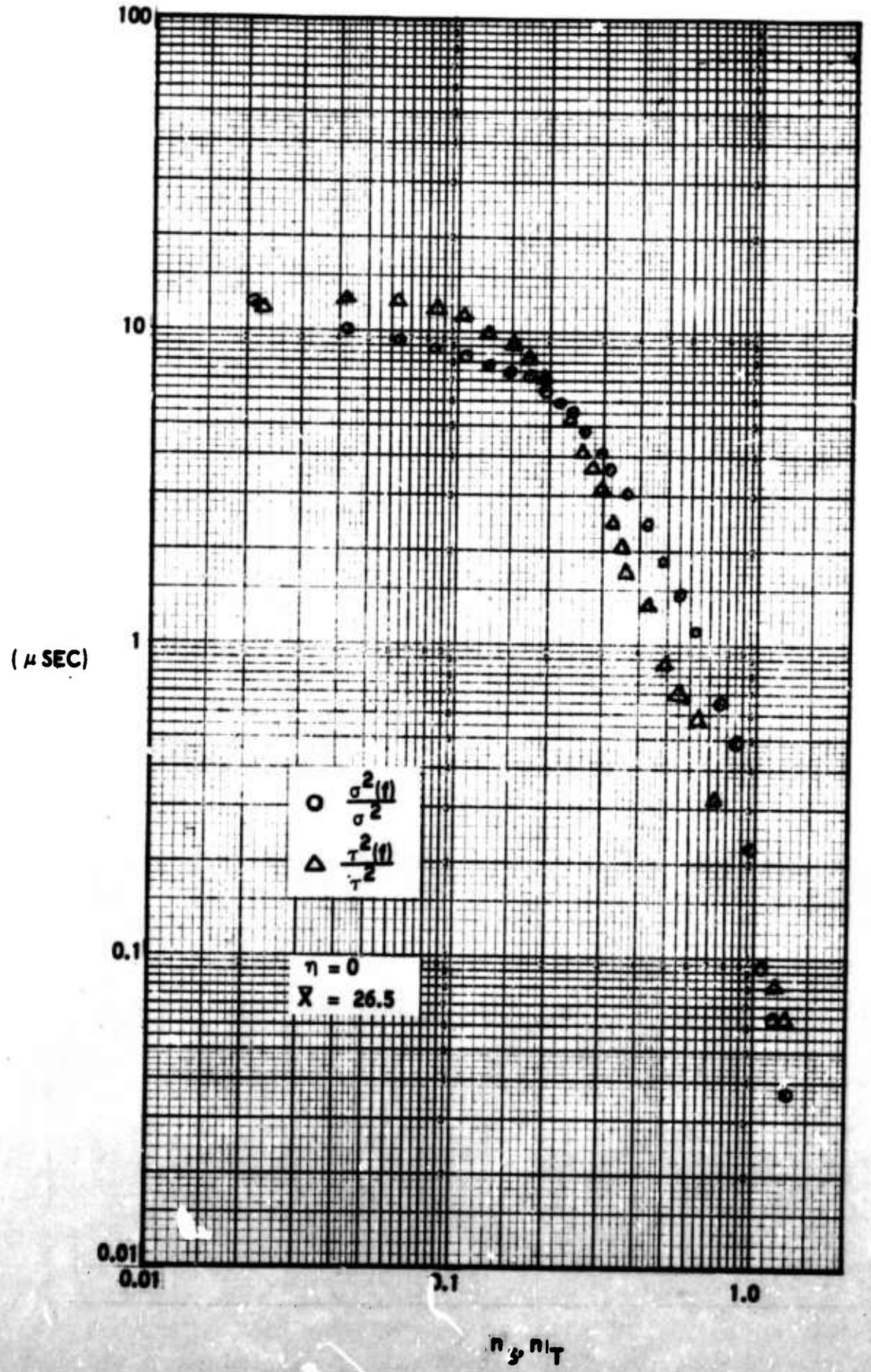

FIGURE 45. TYPICAL DIFFERENCES BETWEEN THE LONGITUDINAL SPECTRA OF MEAN-SQUARE DENSITY AND MEAN-SQUARE VELOCITY FLUCTUATIONS, NORMALIZED WITH THEIR RESPECTIVE MEAN-SQUARE INTEGRATED FLUCTUATIONS.

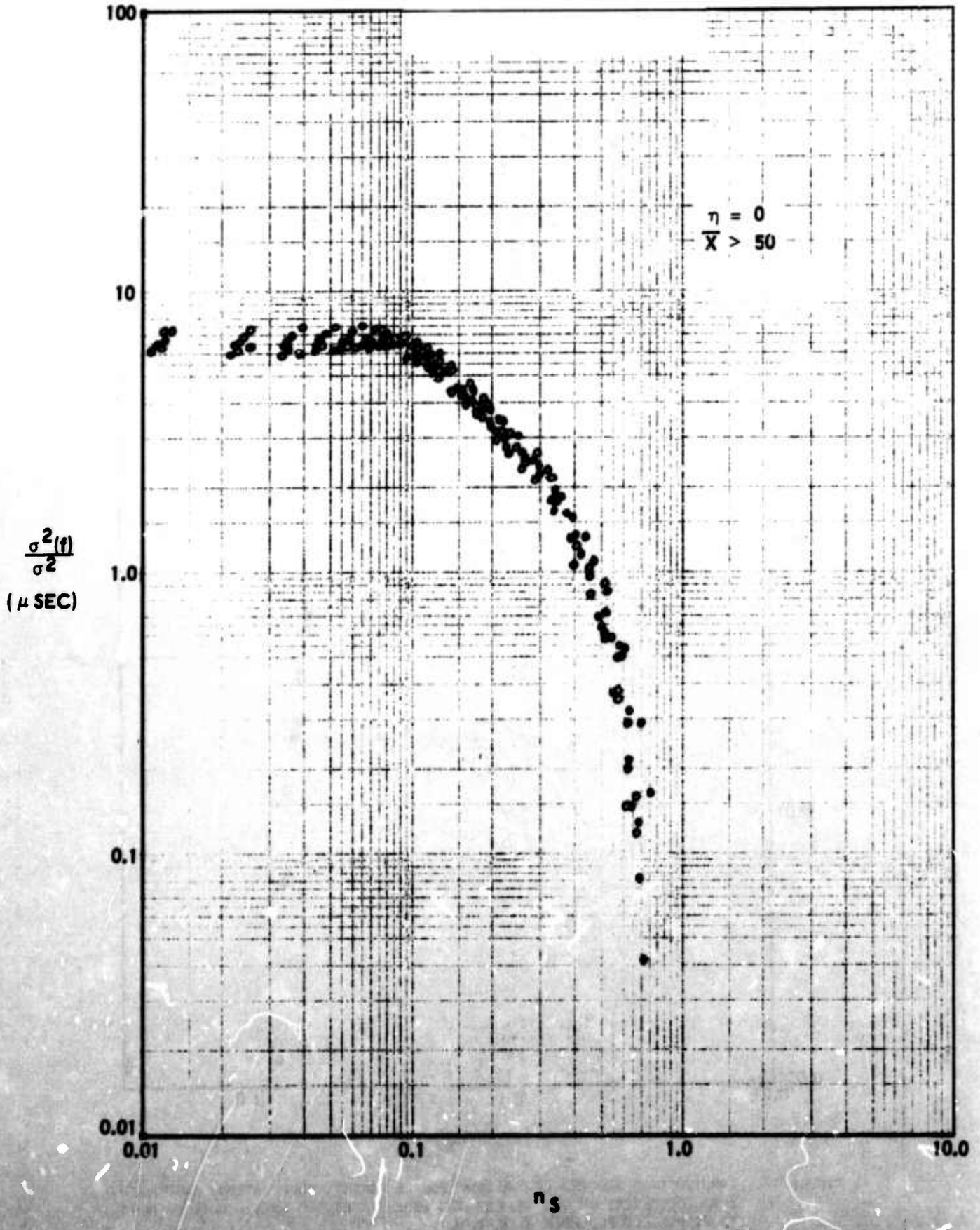

FIGURE 46. LONGITUDINAL SPECTRA OF THE MEAN-SQUARE DENSITY FLUCTUATIONS (NORMALIZED WITH THE INTEGRATED FLUCTUATIONS) ON THE AXIS OF THE SELF-PRESERVING WAKE.

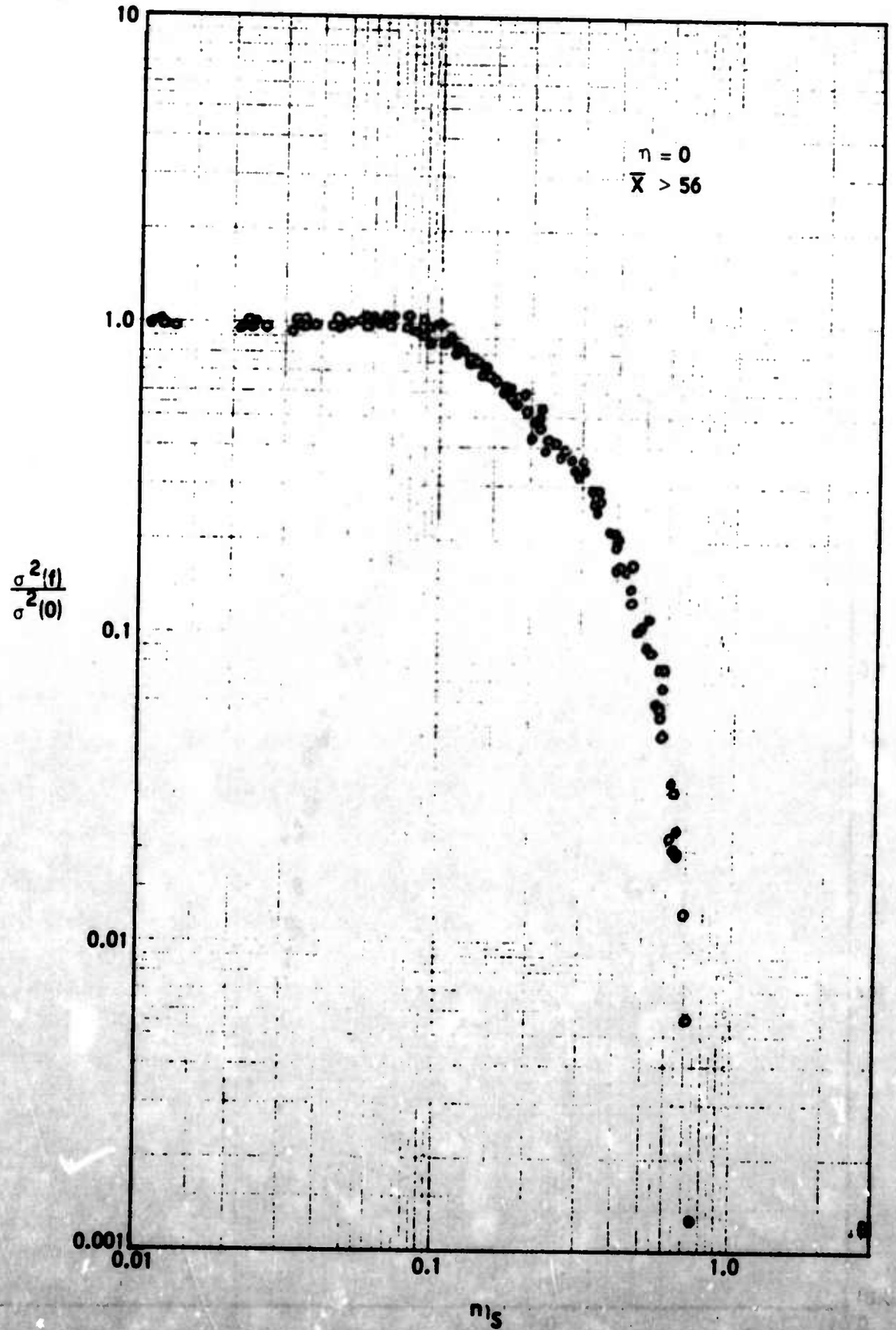

FIGURE 47. LONGITUDINAL SPECTRA OF THE MEAN SQUARE DENSITY FLUCTUATIONS (NORMALIZED AT ZERO FREQUENCY) ON THE AXIS OF THE SELF-PRESERVING WAKE. NOTE EVIDENCE OF FRONT PSEUDOTURBULENCE AT $N_S \approx 0.1$.

relaxing wake, as the data in $14.7 < \bar{X} < 50$ plotted in Figure 48 show. Unfortunately, no such conclusions can be drawn from Figure 49 for the for the velocity fluctuations, due to the large scatter.*

In the region of maximum shear, Figure 50 again reflects the predominance of density fluctuations, whether early ($\bar{X} = 26.5$) or late ($\bar{X} = 85.4$) in the wake. At this radial position in the wake, the observed peak sets in at full strength. In Figure 51, the fractional velocity fluctuation density clearly shows the evolution of the peak at $\bar{X} = 26.5$, 50, and 85.4. Initially, the peak is located at higher frequency ($n_T \simeq 0.2$) and occupies a higher percentage of the total fluctuation; later, it shifts to lower frequencies and decreases in magnitude. A similar result is seen in Figure 52 for the density fluctuations as they develop in the relaxation zone. By contrast, similar results farther along in the wake, shown in Figure 53, show little difference from $\bar{X}$ to $\bar{X}$, and in fact the percentage fluctuation occupied by the peak remains quite constant. On the other hand, the nondimensional plot of Figure 54 destroys this constancy; even so, the peak is well discernible. Figure 53 should be contrasted with Figure 55 which once more points out the unsettled nature of the spectrum during the relaxation process. Inspection of Figure 55 reveals the evolution of the peak itself and also the accompanying variation of the high-frequency components (also shown in Figure 52). It is evident that Fourier contributions of this peak are to be found within a large range of frequencies: as the peak shifts to the left, so do the higher-frequency components. As we turn to Figures 56 and 57, we observe that not only has the scatter in the velocity spectra decreased (compare Figure 49), but the peak behaves differently. Specifically, it seems to disappear completely at the far

*As is easily seen from the spectra, the velocity fluctuation density results are always accompanied by large scatter, partly because these fluctuations, being smaller than those of the density, infringe on the error margin of the measurements.

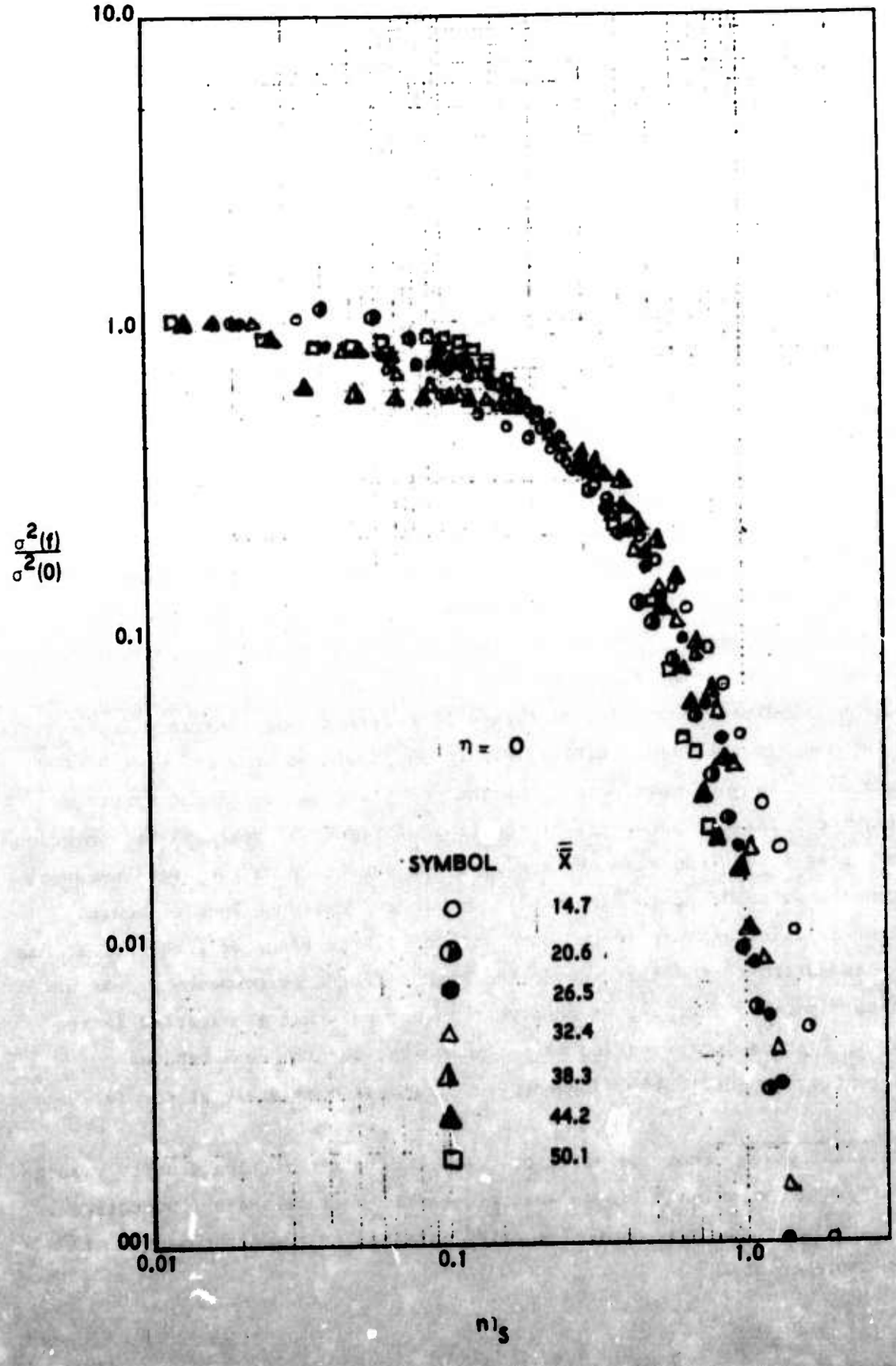

FIGURE 48. EVOLUTION OF THE LONGITUDINAL SPECTRUM OF MEAN-SQUARE DENSITY FLUCTUATIONS NORMALIZED AT ZERO FREQUENCY) ALONG THE AXIS OF THE RELAXING WAKE. COMPARE WITH FIGURE 47.

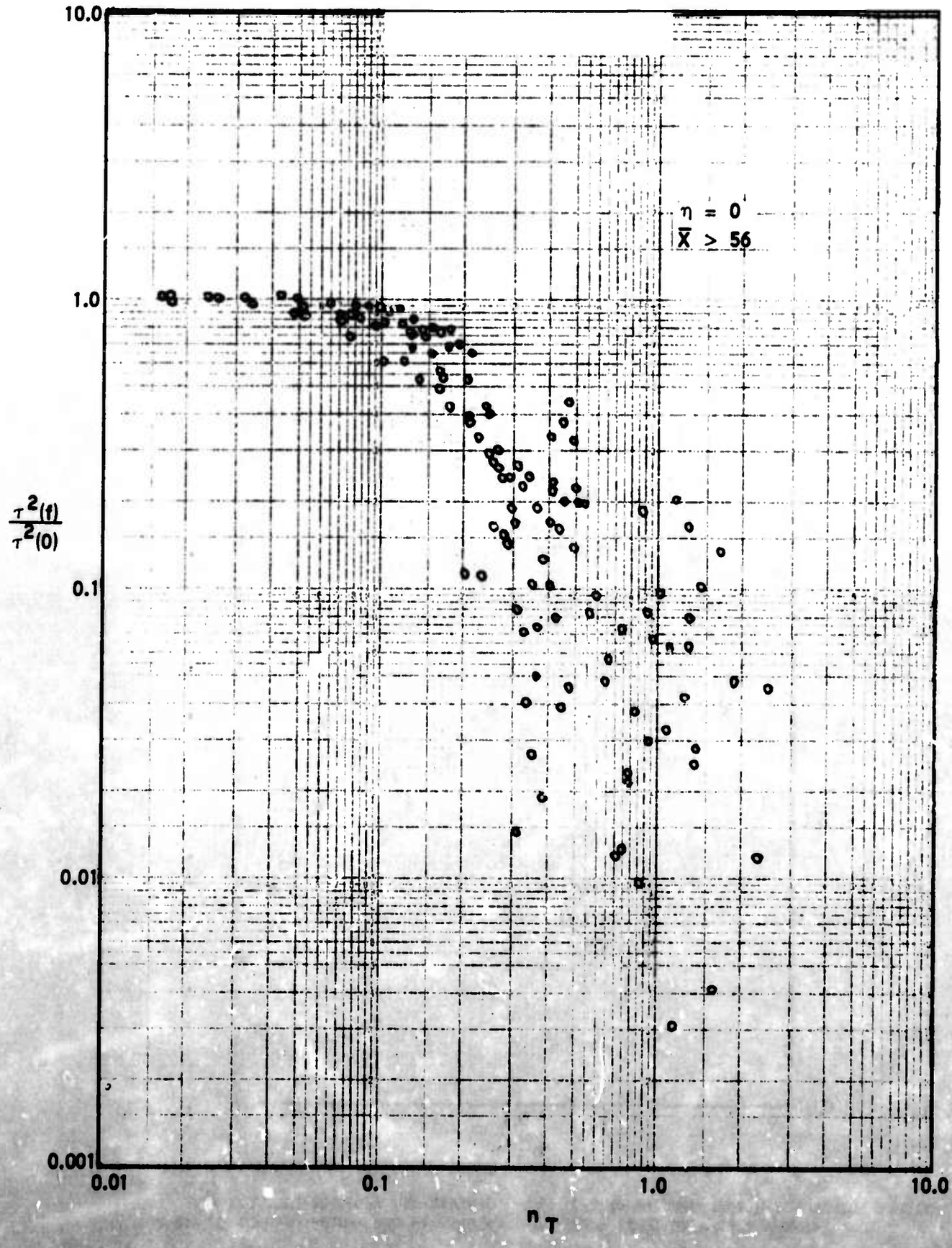

FIGURE 49. LONGITUDINAL SPECTRA OF THE MEAN-SQUARE VELOCITY FLUCTUATIONS (NORMALIZED AT ZERO FREQUENCY) ALONG THE AXIS OF THE SELF-PRESERVING WAKE.

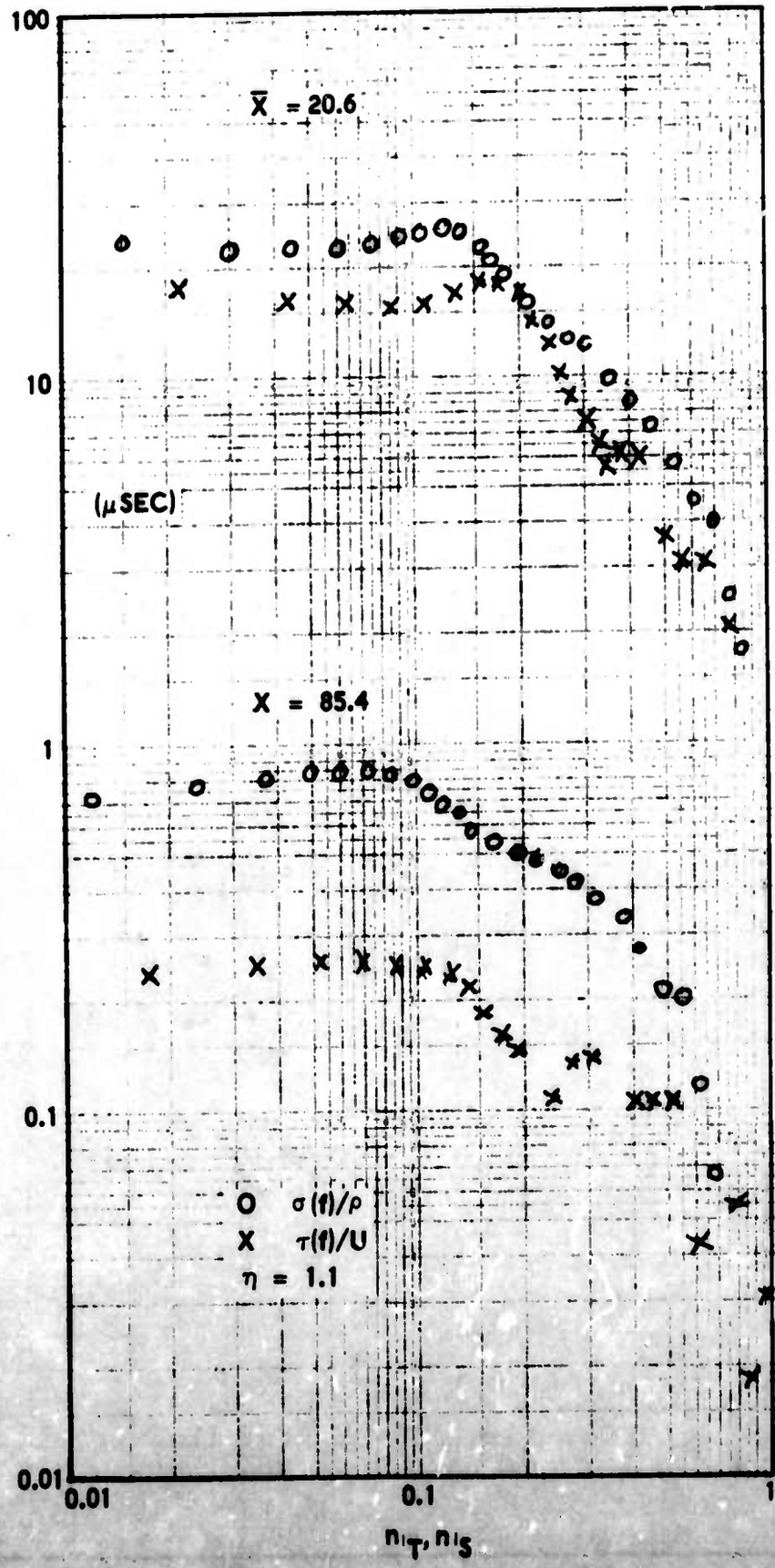

FIGURE 50. LONGITUDINAL SPECTRA OF THE RMS DENSITY AND VELOCITY FLUCTUATIONS (NORMALIZED WITH THEIR LOCAL MEAN VALUES) IN THE REGION OF MAXIMUM SHEAR.

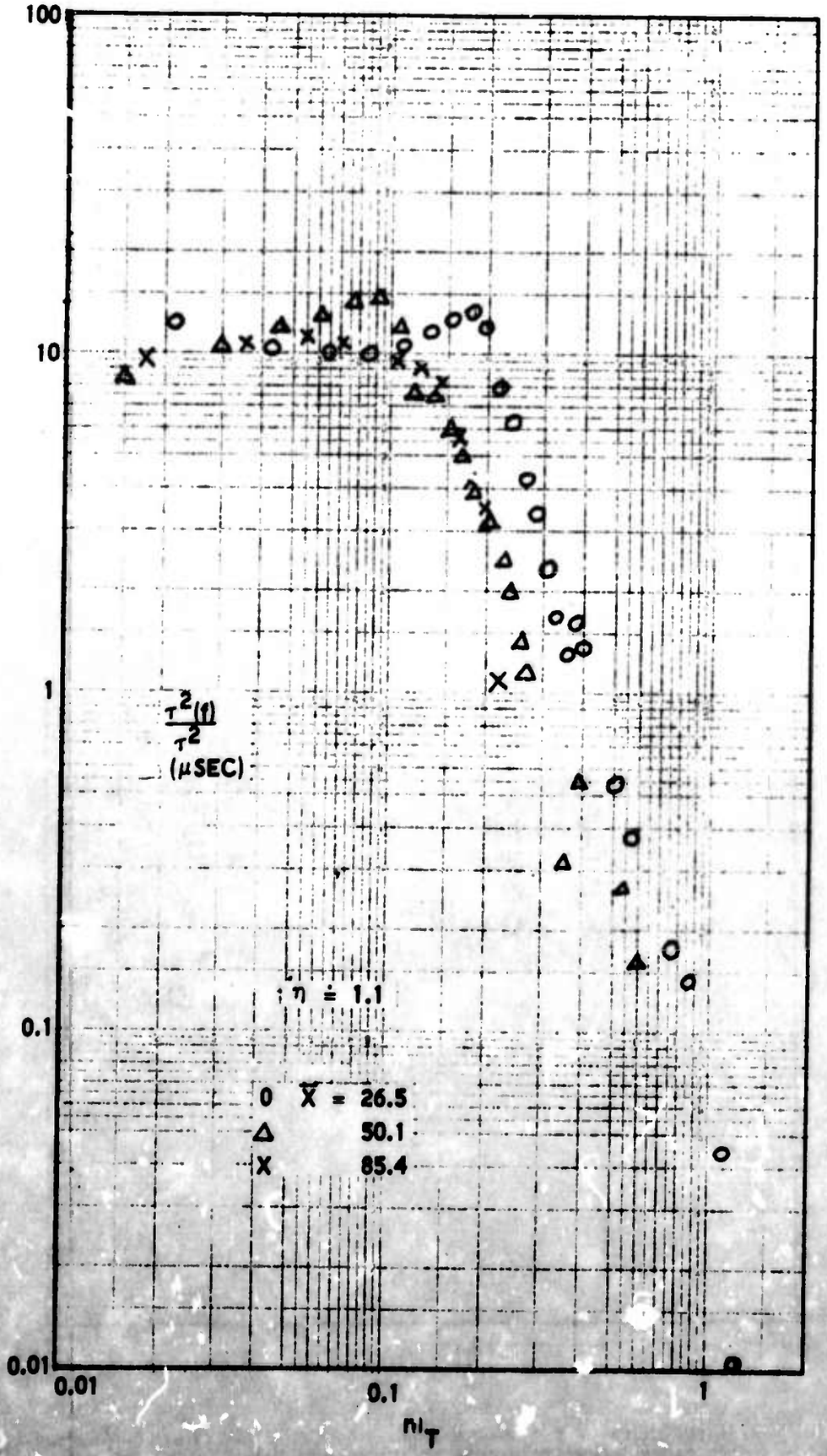

FIGURE 51. AXIAL EVOLUTION OF THE LONGITUDINAL SPECTRUM OF THE MEAN-SQUARE VELOCITY FLUCTUATION (NORMALIZED WITH THE INTEGRATED FLUCTUATION) IN THE REGION OF MAXIMUM SHEAR.

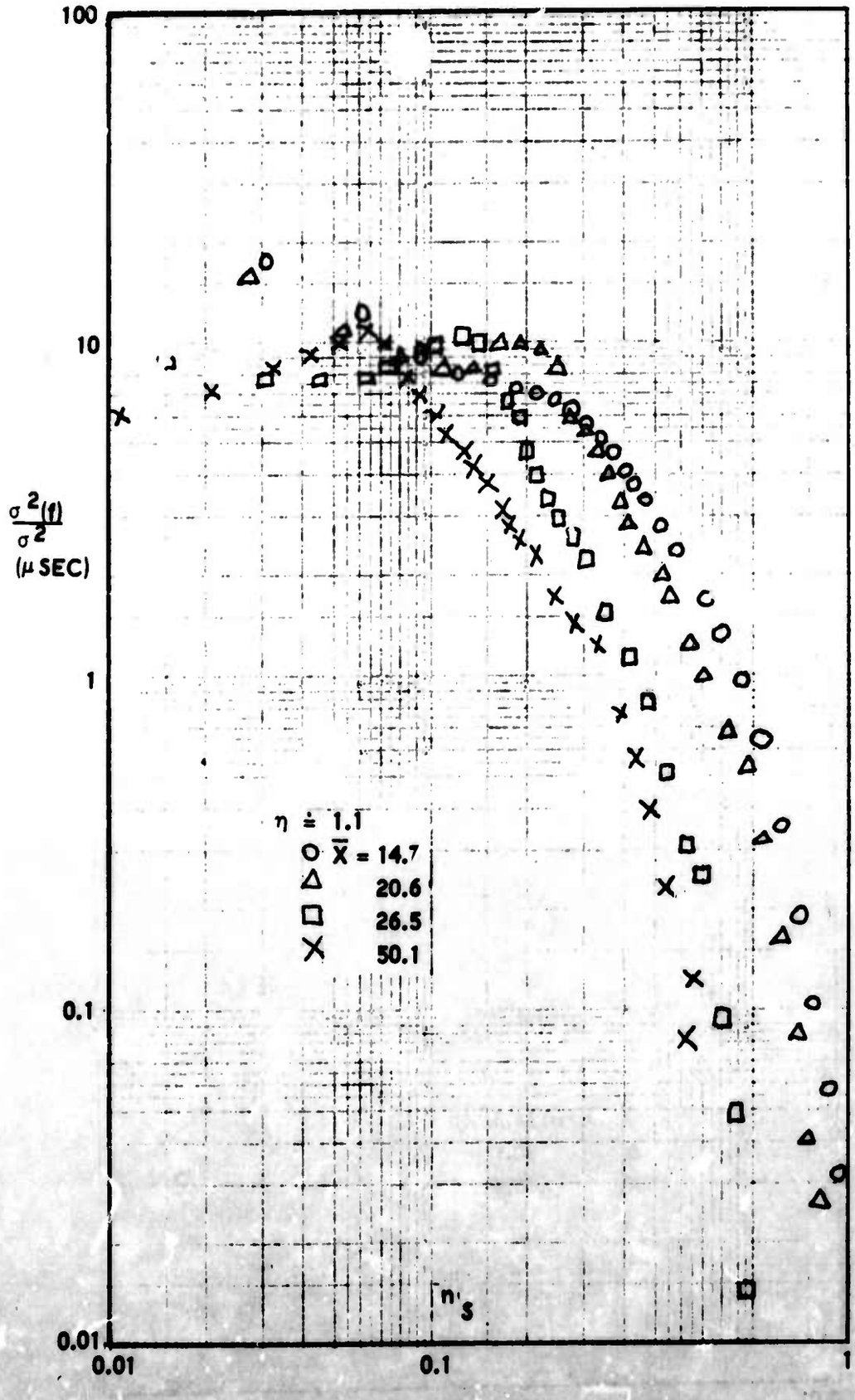

FIGURE 52. AXIAL EVOLUTION OF THE LONGITUDINAL SPECTRUM OF THE MEAN-SQUARE DENSITY FLUCTUATIONS (NORMALIZED WITH THE INTEGRATED FLUCTUATIONS) IN THE REGION OF MAXIMUM SHEAR.

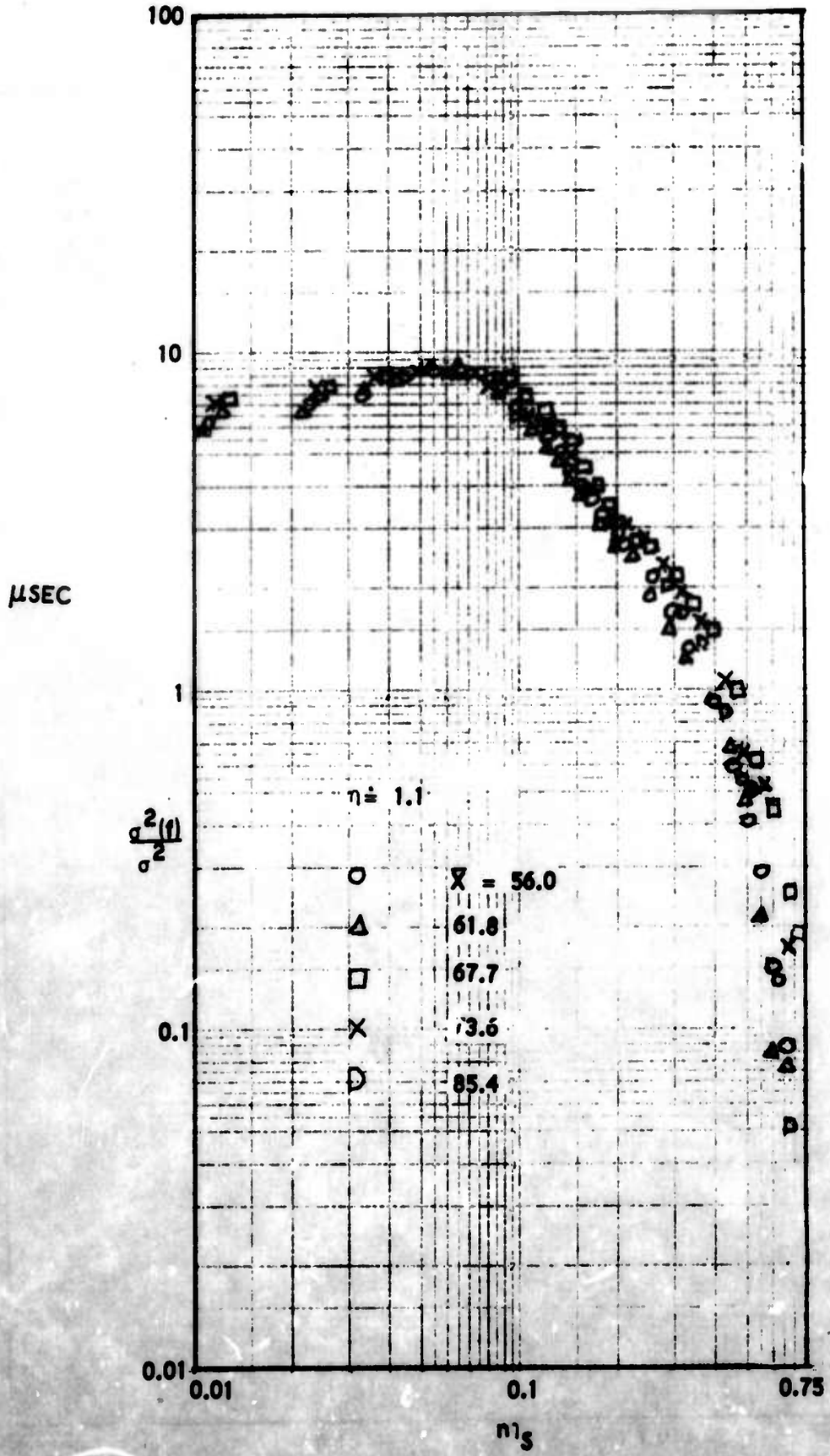

FIGURE 53. THE LONGITUDINAL SPECTRA OF MEAN-SQUARE DENSITY FLUCTUATIONS (NORMALIZED WITH THE INTEGRATED FLUCTUATION) IN THE REGION OF MAXIMUM SHEAR OF THE SELF-PRESERVING WAKE.

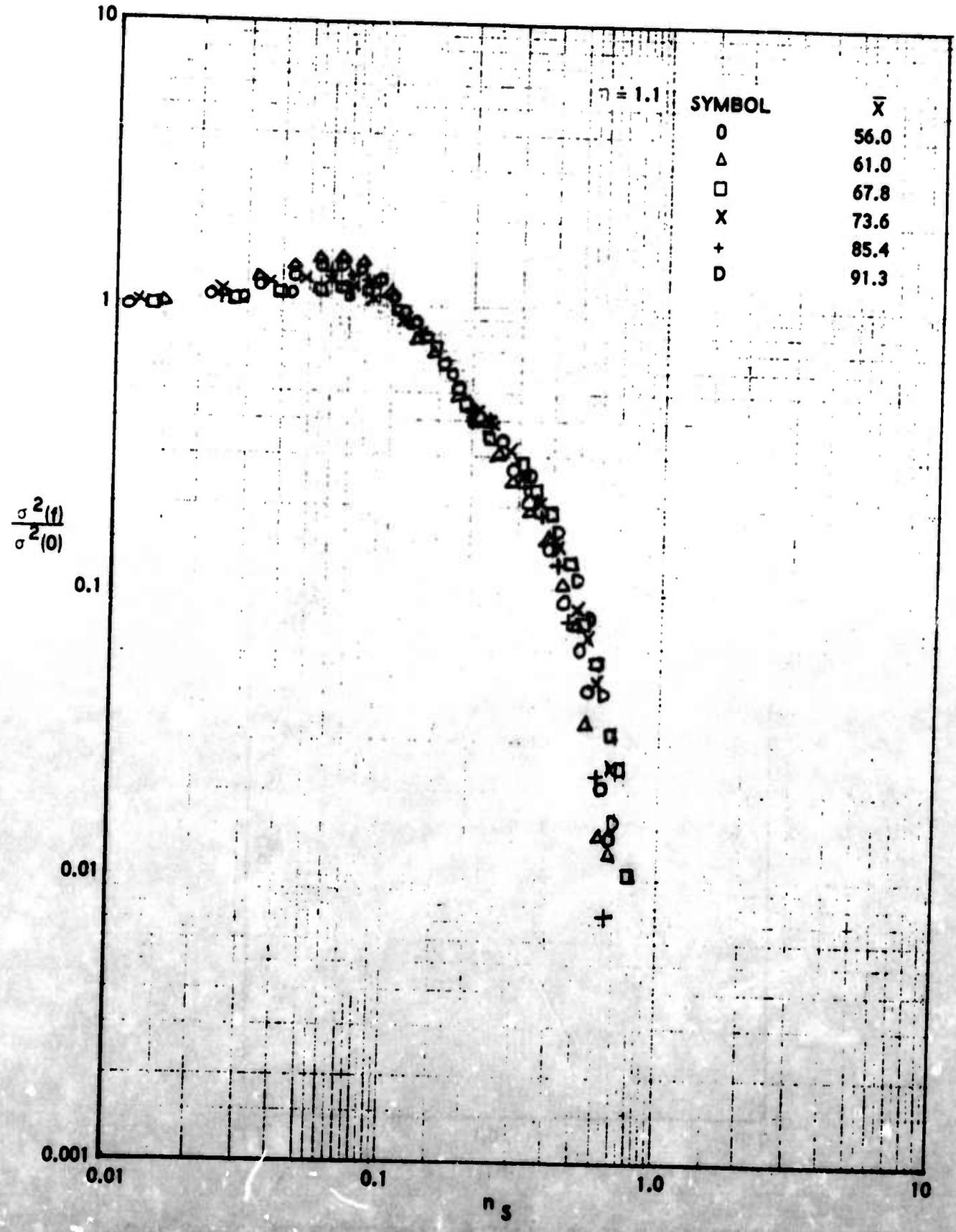

FIGURE 54. THE LONGITUDINAL SPECTRA OF THE MEAN-SQUARE DENSITY FLUCTUATIONS (NORMALIZED AT ZERO FREQUENCY) IN THE MAXIMUM-SHEAR REGION OF THE SELF-PRESERVING WAKE.

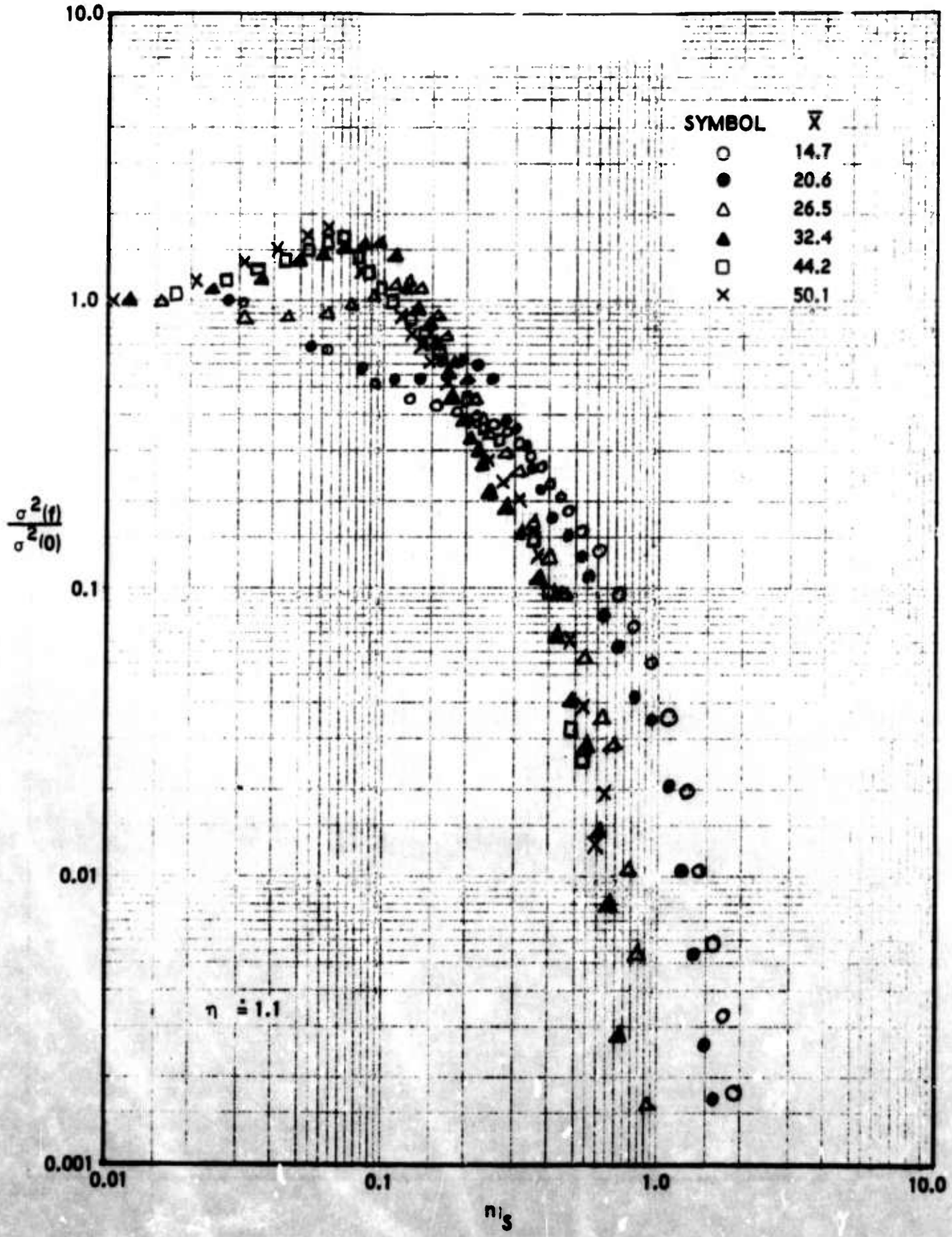

FIGURE 55. THE LONGITUDINAL SPECTRA OF THE MEAN-SQUARE DENSITY FLUCTUATIONS (NORMALIZED AT ZERO FREQUENCY) IN THE MAXIMUM-SHEAR REGION OF THE RELAXING WAKE. NOTE DEVELOPMENT OF PEAK.

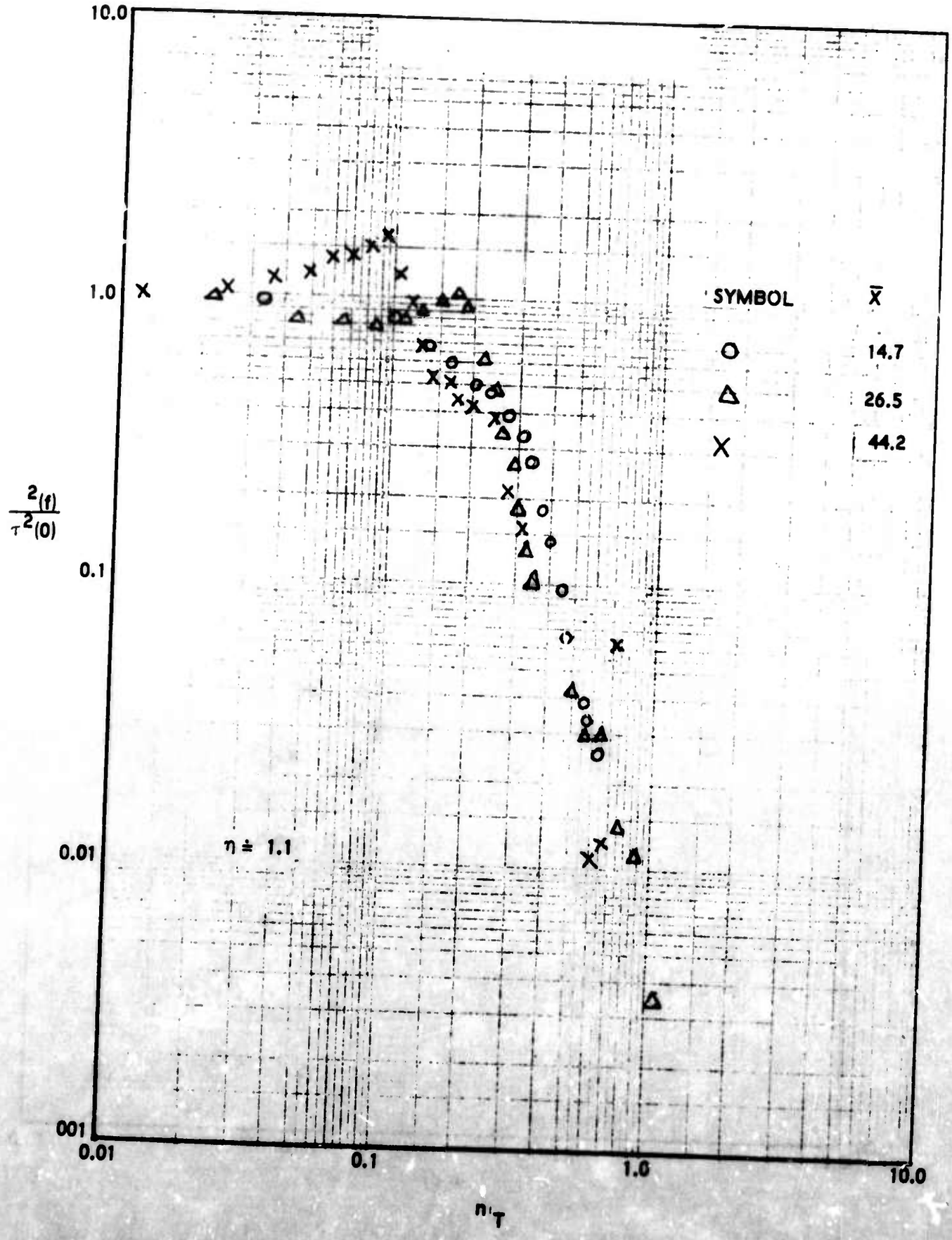

FIGURE 56. THE LONGITUDINAL SPECTRA OF THE MEAN-SQUARE VELOCITY FLUCTUATIONS (NORMALIZED AT ZERO FREQUENCY) IN THE MAXIMUM-SHEAR REGION OF THE RELAXING WAKE.

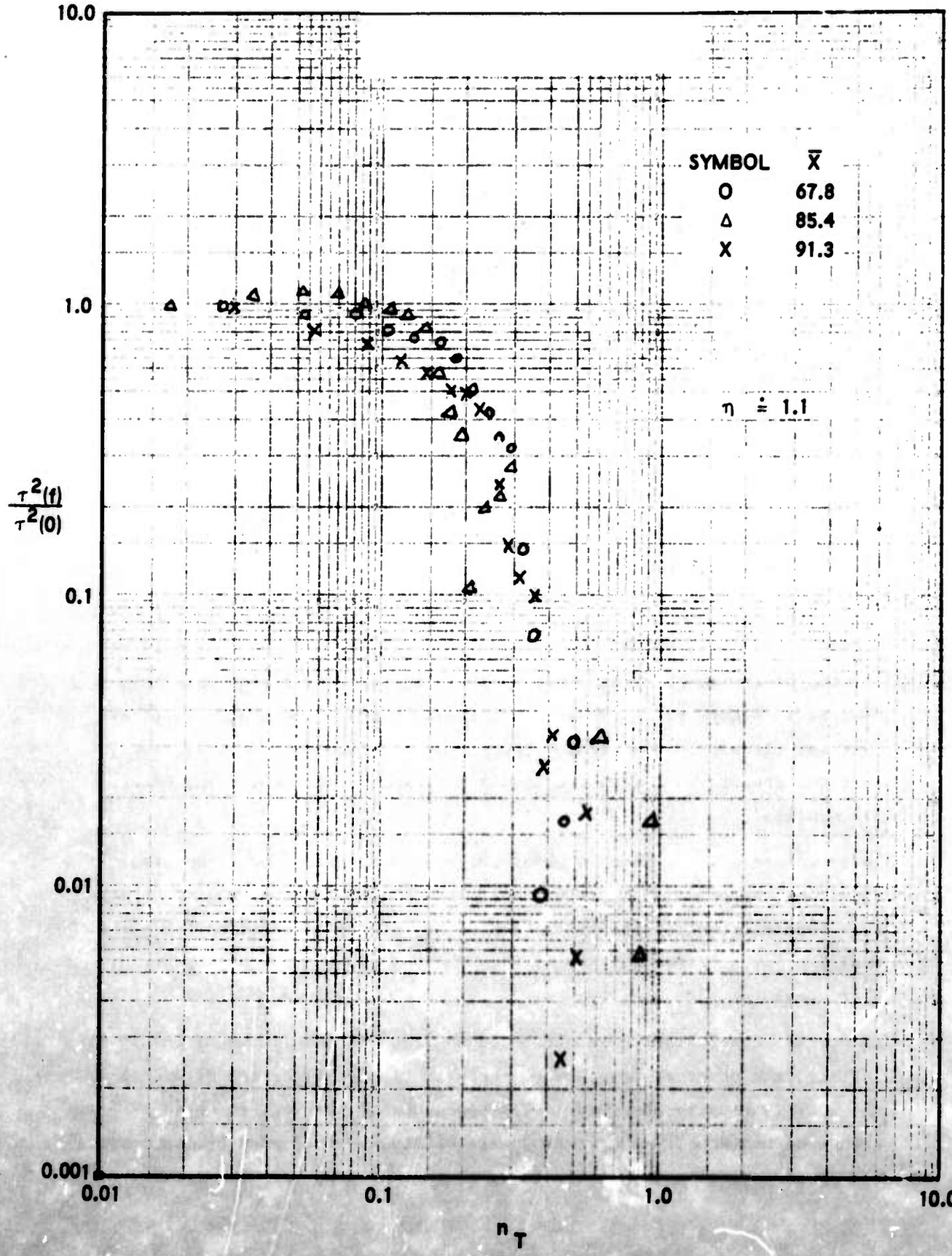

FIGURE 57. THE LONGITUDINAL SPECTRA OF THE MEAN-SQUARE VELOCITY FLUCTUATIONS (NORMALIZED AT ZERO FREQUENCY) IN THE MAXIMUM-SHEAR REGION OF THE SELF-PRESERVING WAKE.

distances ($\bar{X}$ = 67.7, 85.4, 91.3). We therefore conclude that, whatever mechanism is responsible for this peak, it operates mainly through the density rather than the velocity.

A generally identical sort of behavior of the spectral densities can be found along the turbulent front (η = 2.1), as can be seen from the following group of illustrations. Of these, Figure 58 shows the well-established decreases of the densities in terms of fractions of the local mean values, and the tendency of this decrease to occur primarily in the larger eddies. Figures 59, 60, and 61 use the alternate spectral representations to illuminate the evolution of the spectra with axial distance. Again, the shift of the peak to lower frequencies and its decrease with distance are perfectly clear. It is furthermore obvious that, as noticed previously, the density fluctuation density retains the evidence of this peak for a perceptibly longer axial distance.

As a final region of interest, consider the wake edge which, in view of our previous findings, can be thought as lying around η = 3.3. The nondimensional spectra of the density fluctuations for this radial position have been plotted in Figure 62 in the self-preserving region. This plot verifies what was already indicated, to some extent, by Figures 42 and 43, i.e., that the spectra have returned to a normal shape, the peak being hardly discernible.

To formalize what is learned about the radial distribution of spectral densities, we present Figure 63, where the nondimensional density spectra have been plotted for all radial positions, at the farthest downstream position investigated (at $\bar{X}$ = 91.3). The appearance of the peak here is quite weak.

An overall conclusion which can be drawn from the inspection of the spectra is that, the observed peak aside, there is little difference between them and what is usually observed in low-speed turbulent flows in which a certain amount of homogeneity and isotropy are obtained. In Figure 64, we compare the present results (typically those shown in Figure 63) with spectra

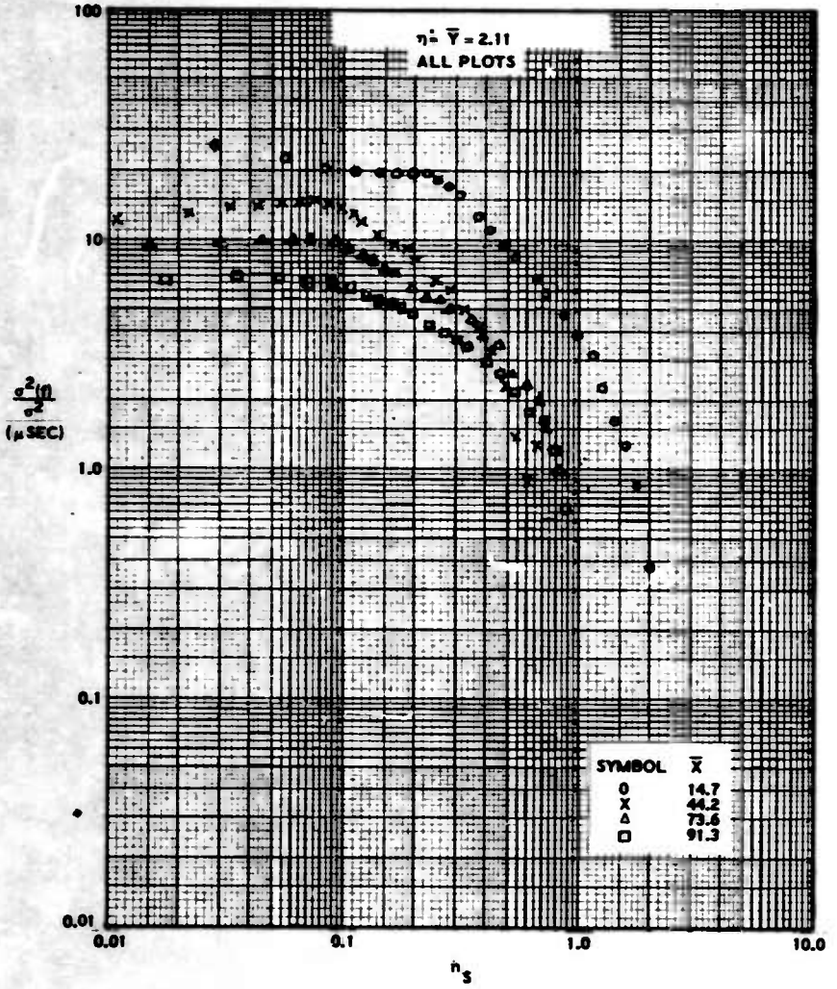

FIGURE 58a. AXIAL EVOLUTION OF THE LONGITUDINAL MEAN-SQUARE SPECTRUM OF THE DENSITY FLUCTUATION (NORMALIZED WITH THE INTEGRATED FLUCTUATIONS) AS THE WAKE FRONT.

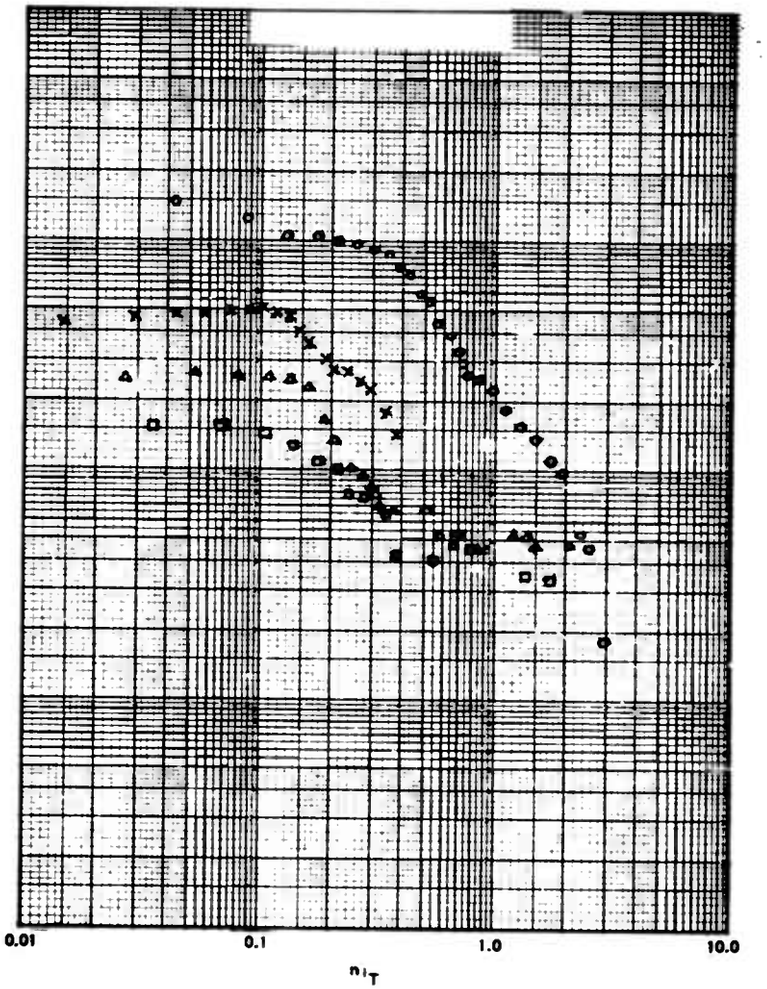

FIGURE 58b. AS IN FIGURE 58a, FOR THE VELOCITY SPECTRUM.

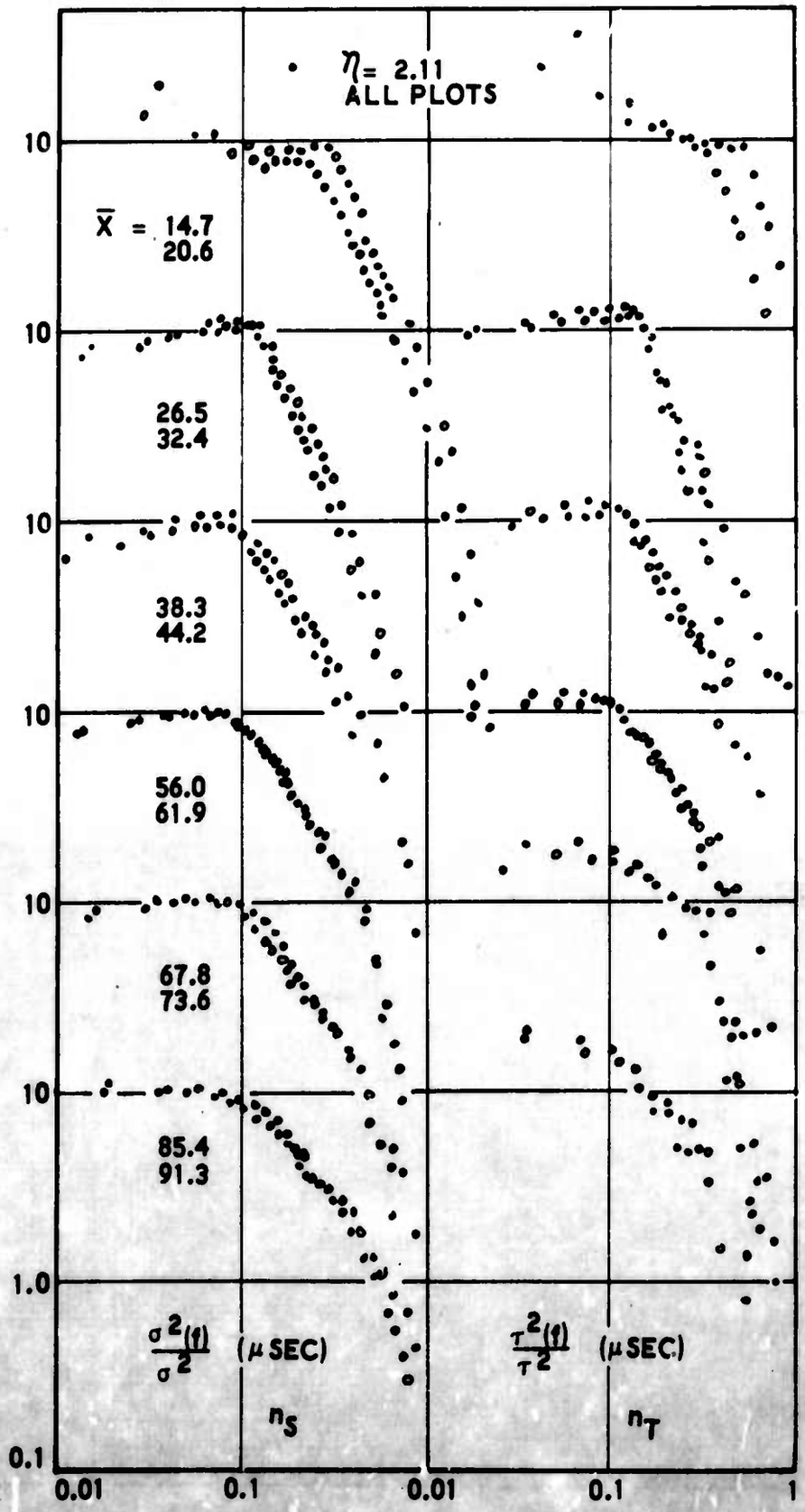

FIGURE 59. AXIAL EVOLUTION OF THE LONGITUDINAL SPECTRA OF MEAN-SQUARE DENSITY (LEFT) AND VELOCITY (RIGHT) FLUCTUATIONS (NORMALIZED WITH THE INTEGRATED FLUCTUATION) AT THE WAKE FRONT.

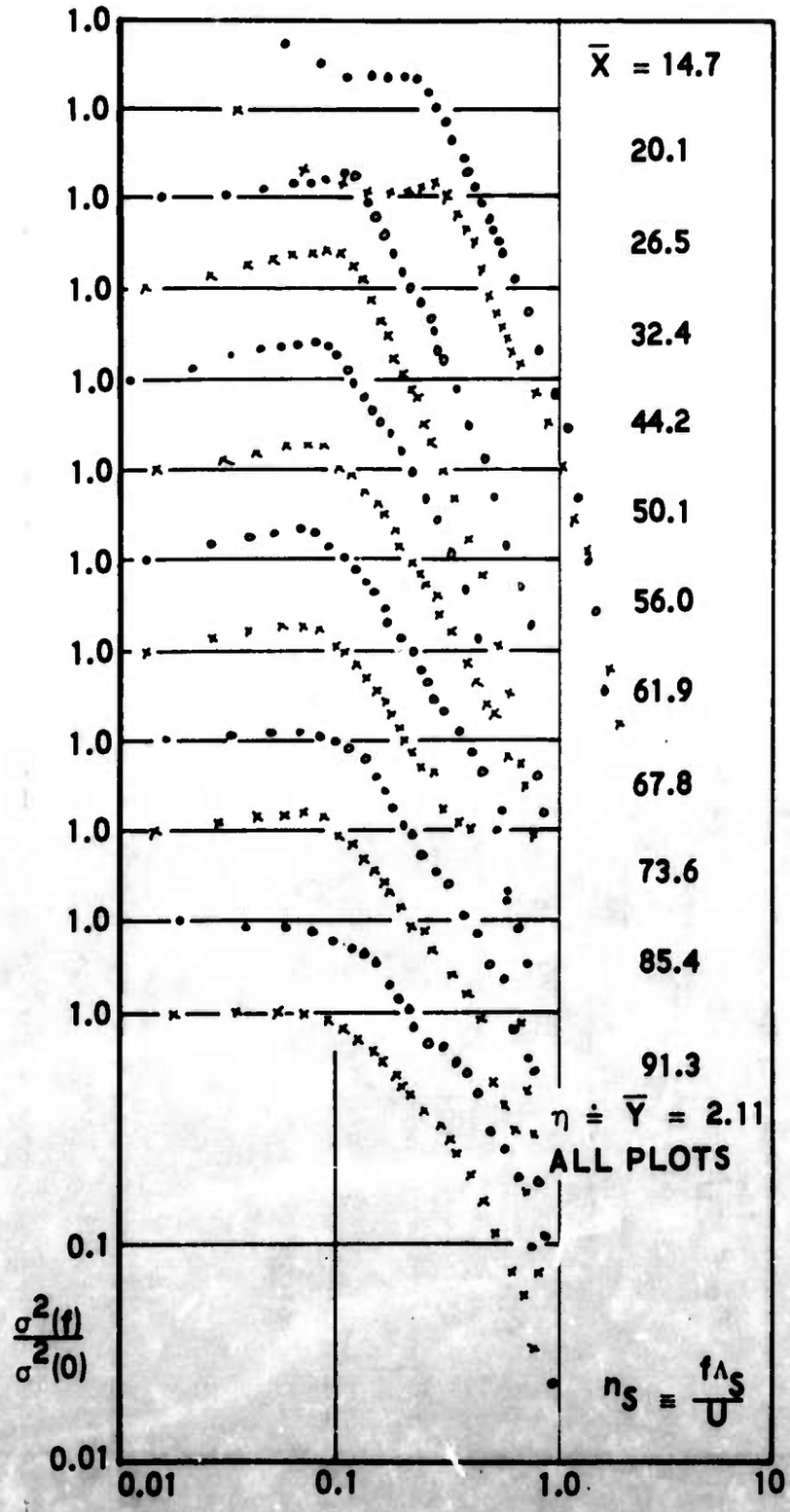

FIGURE 60. AXIAL EVOLUTION OF THE LONGITUDINAL SPECTRA OF MEAN-SQUARE DENSITY FLUCTUATIONS (NORMALIZED AT ZERO FREQUENCY) AT THE WAKE FRONT.

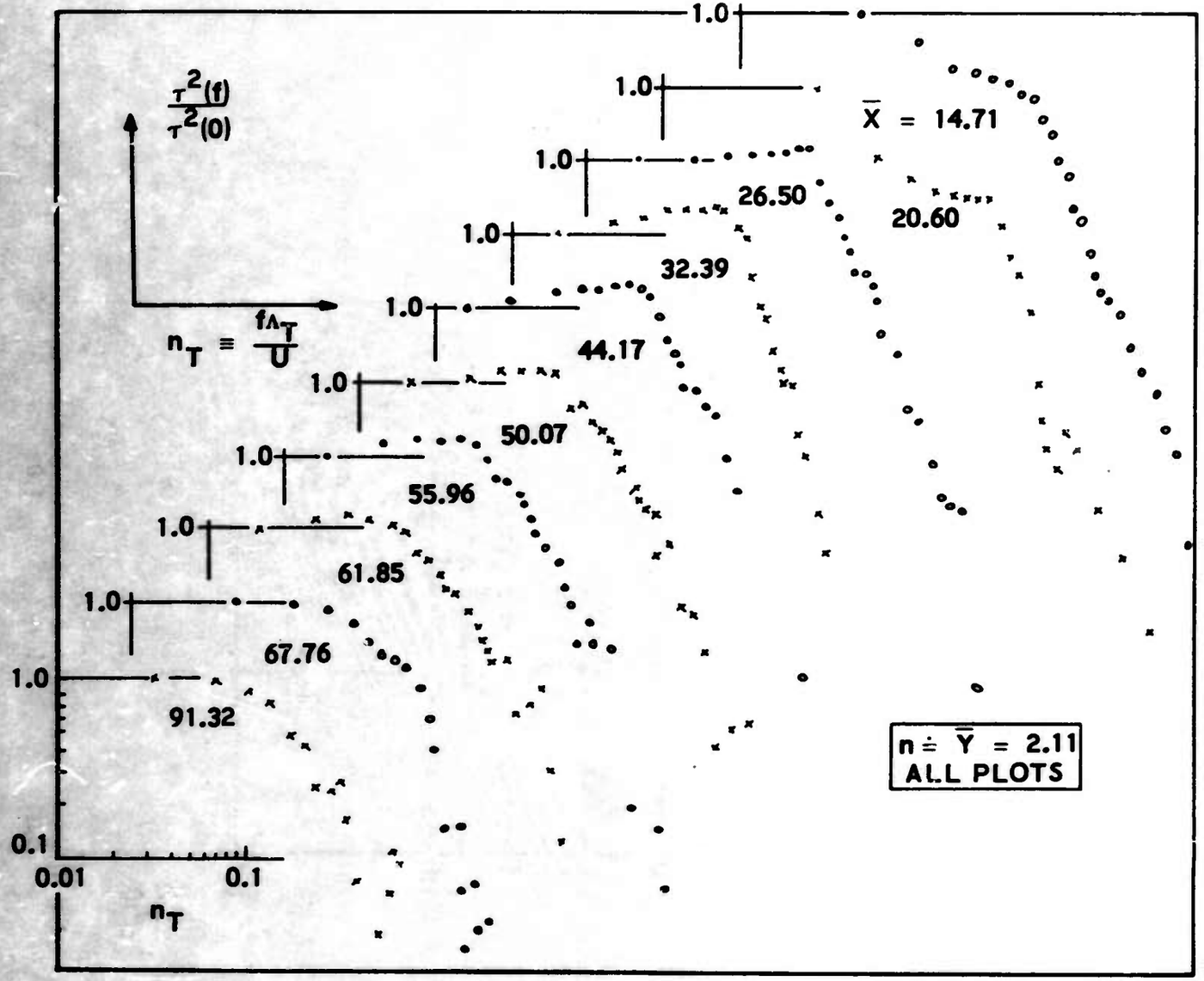

FIGURE 61. AXIAL EVOLUTION OF THE LONGITUDINAL SPECTRA OF THE MEAN-SQUARE VELOCITY FLUCTUATIONS (NORMALIZED AT ZERO FREQUENCY) AT THE WAKE FRONT.

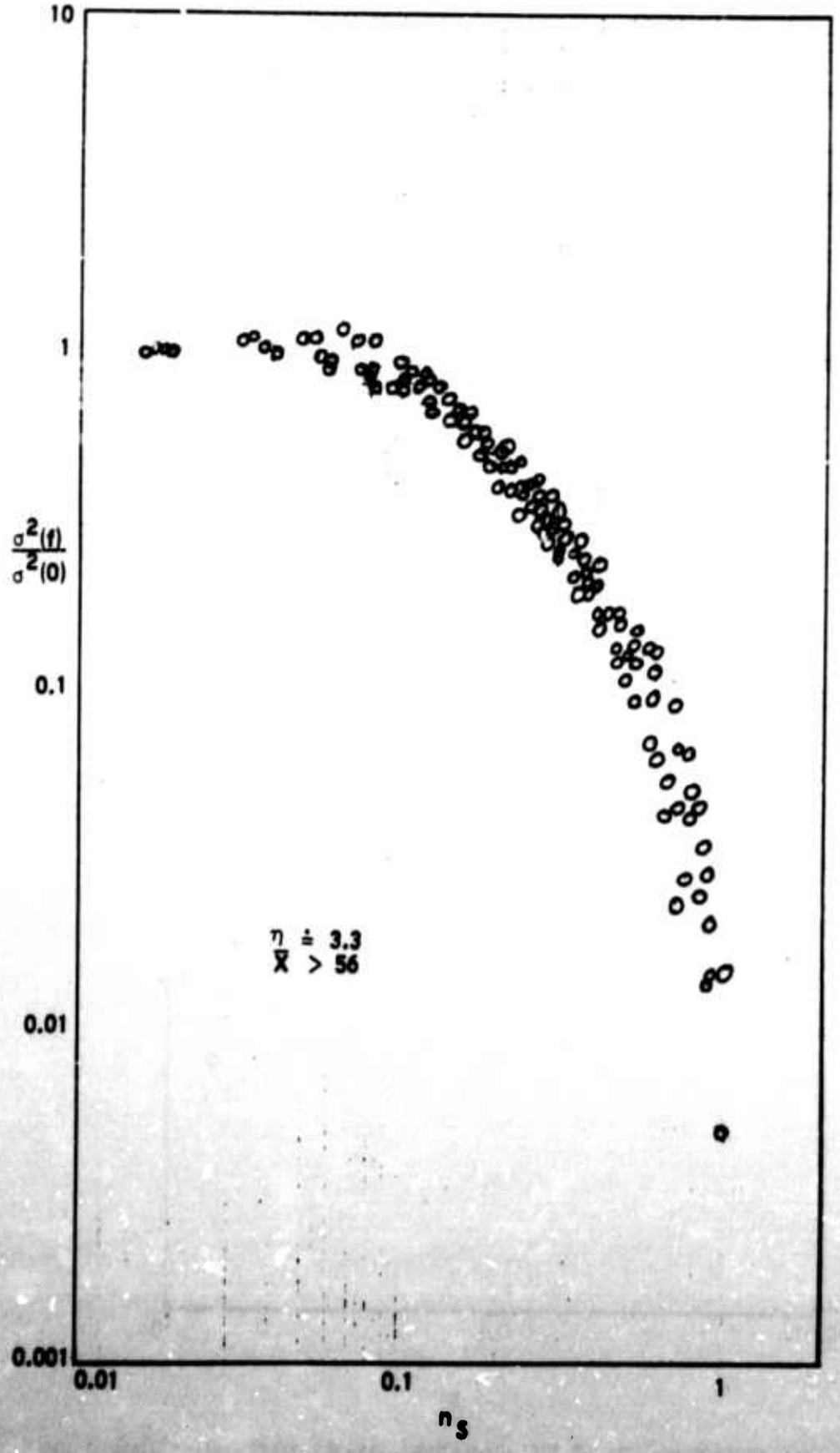

FIGURE 62. LONGITUDINAL SPECTRA OF THE MEAN-SQUARE DENSITY FLUCTUATIONS (NORMALIZED AT ZERO FREQUENCY) AT THE EDGE OF THE SELF-PRESERVING WAKE.

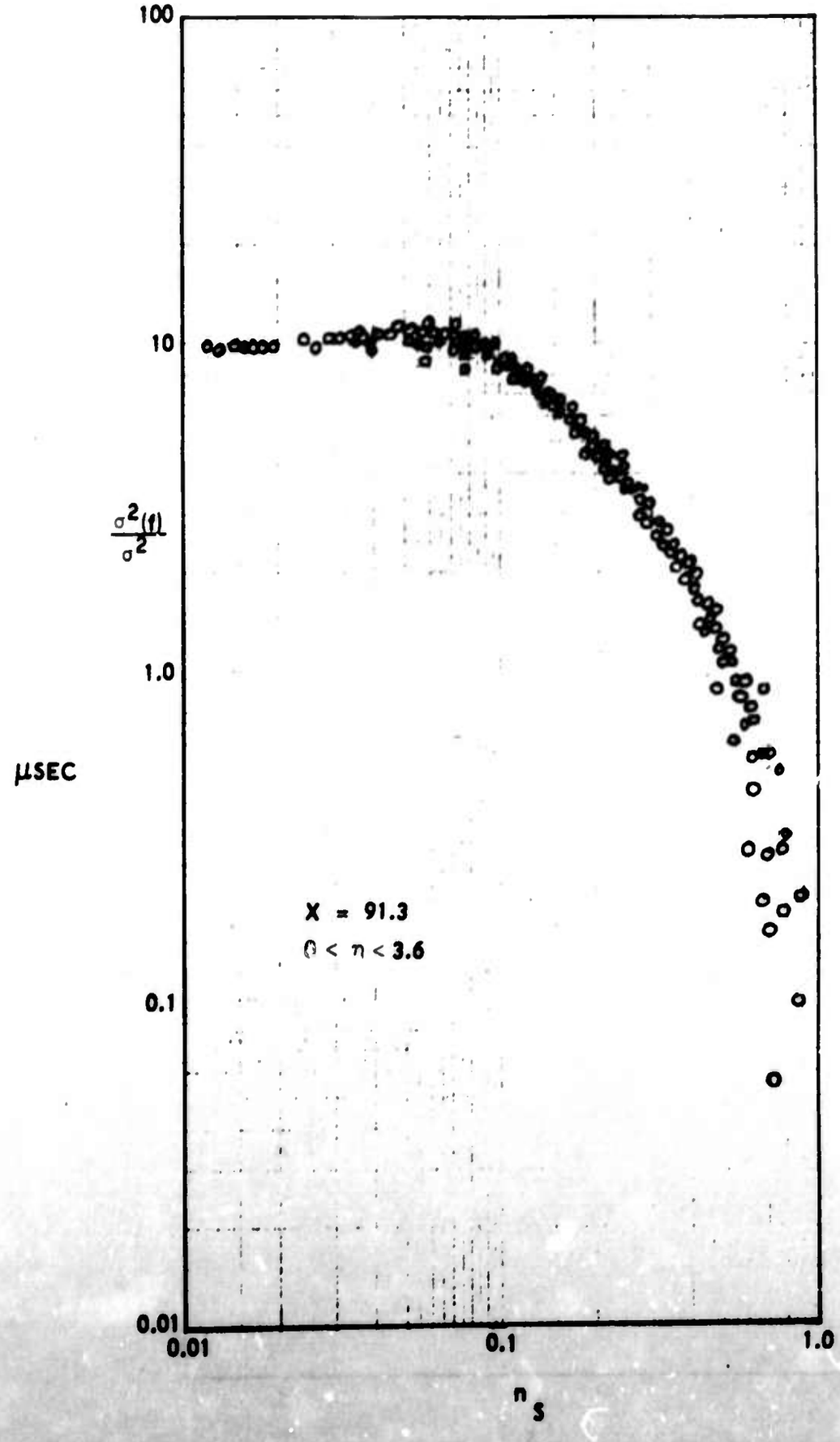

FIGURE 63. LONGITUDINAL SPECTRA OF THE MEAN-SQUARE DENSITY FLUCTUATIONS (NORMALIZED WITH THE INTEGRATED FLUCTUATIONS) IN THE SELF-PRESERVING WAKE.

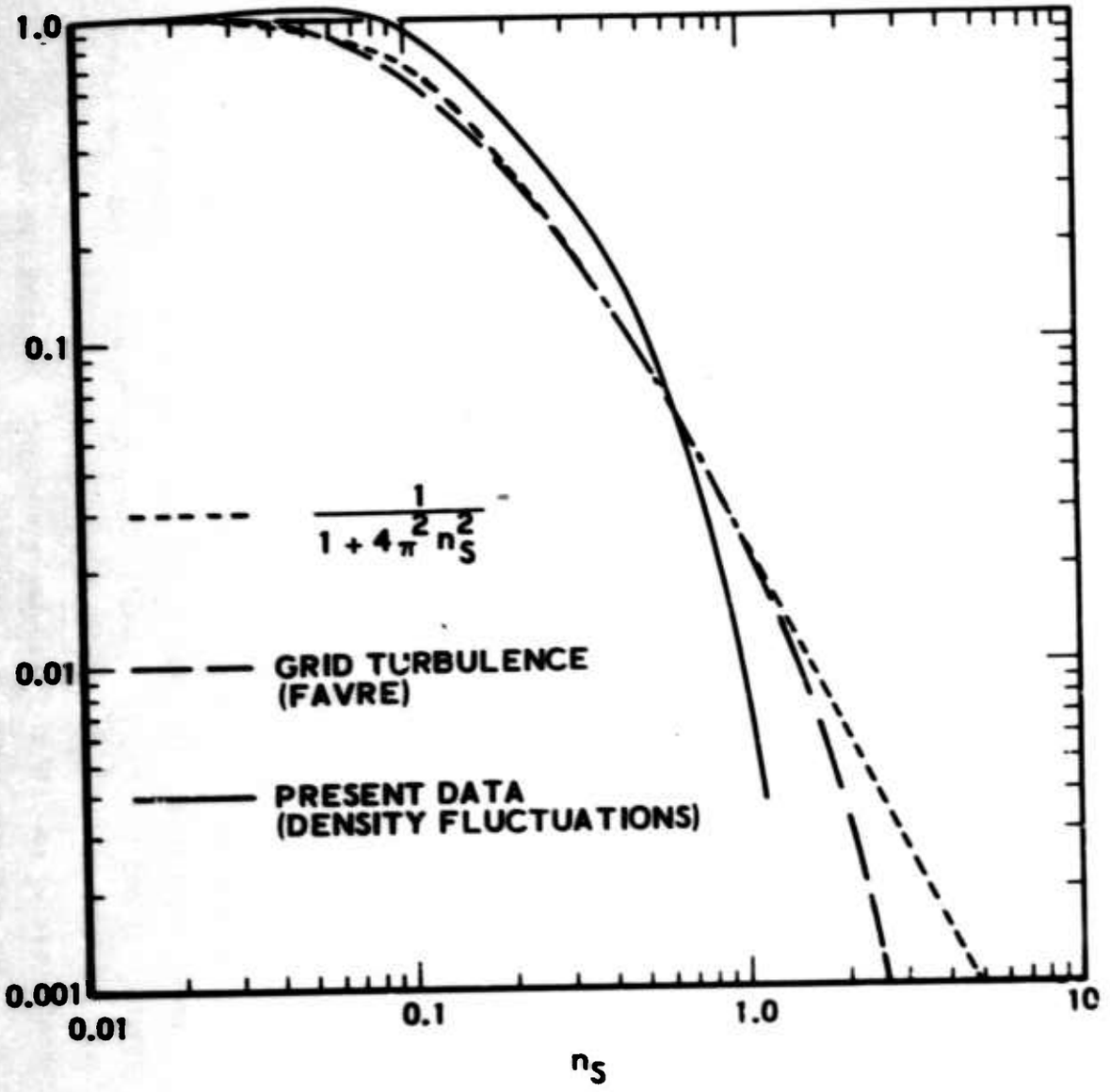

FIGURE 64. LONGITUDINAL SPECTRA OF MEAN-SQUARE DENSITY FLUCTUATIONS (NORMALIZED AT ZERO FREQUENCY) FOR THE COMPRESSIBLE WAKE COMPARED WITH LOW-SPEED RESULTS.

obtained by Favre (Reference 20) behind a grid. A commonly used analytical expression for the one-dimensional velocity fluctuation spectrum is also shown for comparison. These three spectra differ little for eddy sizes larger than the integral scale, but there is considerable disagreement among the three at the higher frequencies. In fact, the fluctuation density thus nomalized shows that in the compressible wake studied the fluctuation density is, for eddies the size of the integral scale, one-half as large as at low speeds.

The new and, to a certain degree unexpected phenomenon, is the appearance of the peak or prominence in the spectra. We have seen that this phenomenon shows certain organized traits which will be used, in the ensuing discussion, to discover its origin.

We have noted that the peak behaves as follows: (1) it appears strongest about halfway between the wake axis and the wake edge, diminishing toward the axis and the edge; (2) it appears most markedly in the initial (relaxation stage) and thereafter decays; (3) the peak frequency is initially quite high (tending toward a length scale approaching the integral scale of the turbulence) but thereafter decreases; (4) the peak is more pronounced, although not by very much, in the density rather than the velocity spectrum. To these we add two additional observations: (5) when the peak frequency is plotted versus the radius at various $\bar{X}$ as in Figure 65, we note that in the usual dimensional units the frequency is on the order of 50 kilocycles per second at the beginning, and that its previously noted decrease with $\bar{X}$ brings it closer to an average value of between 20 and 30 kilocycles per second. From Figure 65 one further sees that the value of the peak frequency tends to attain a maximum at about the midpoint between the axis (η = o) and the edge. (We shall return to the use of these phenomena.) Last, the hot-wire signal was passed through an intermittency circuit whose function was to rectify the turbulence component and mark, by an on-off signal, the entrance and exit of the wire into the zones of turbulence. The spectrum of this output signal was measured and was found to be

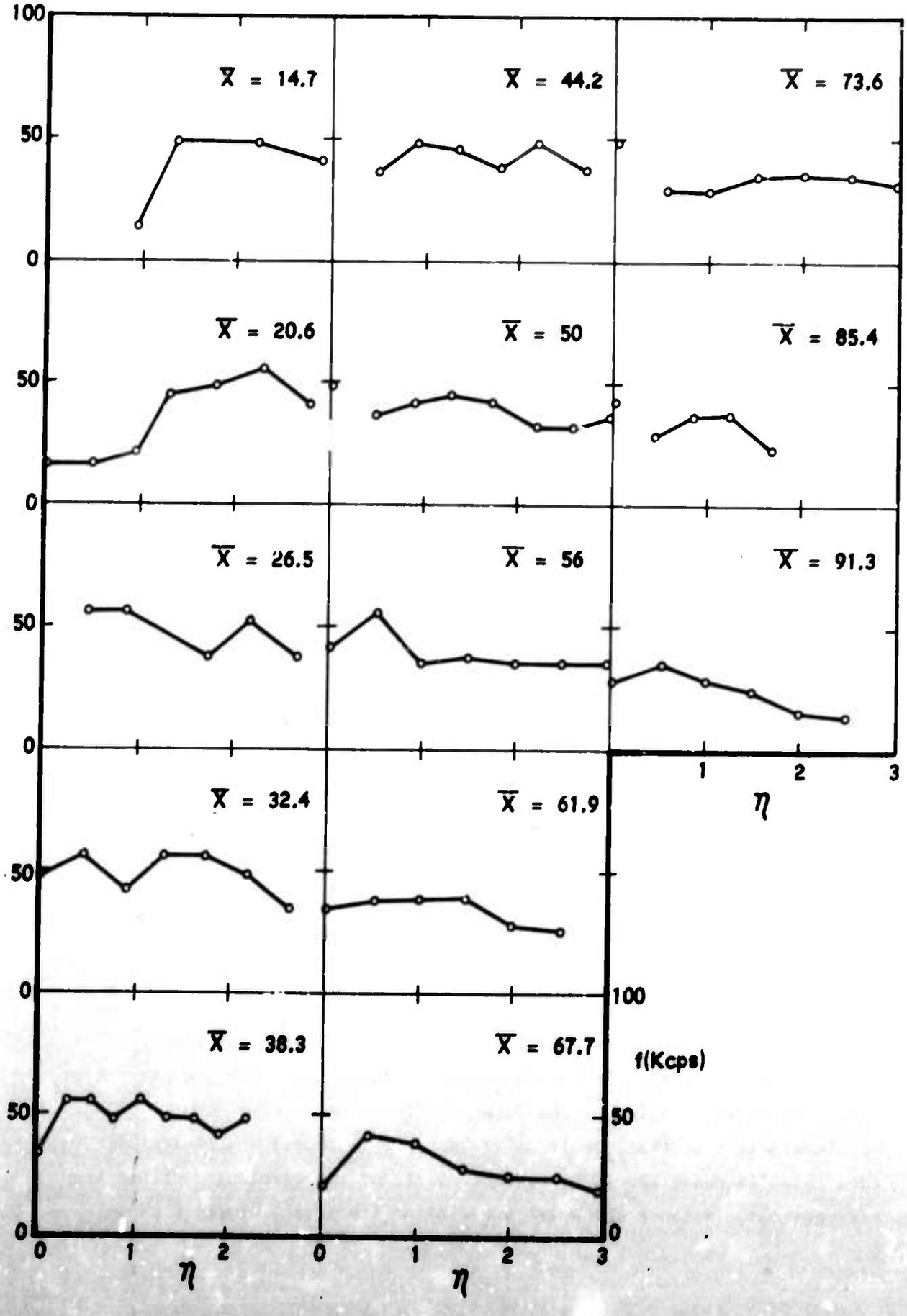

FIGURE 65. PEAK SPECTRUM FREQUENCY VARIATION WITH WAKE RADIUS.

characteristically identical with the total wire output. The peak, especially, survived the rectification process and appeared intact in the rectified spectrum. The latter is, in fact, the same as the Schmidt-trigger output spectrum which Corrsin and Kistler (Reference 21) measured in the turbulent interface of a jet and found to be of the Poisson type.

The latter test provides the strongest first clue as to the origin of the peak, namely that it is due to the fluctuations arising from the corrugations of the interface rather than the turbulence within these corrugations. If, roughly speaking, the intermittent signal is thought of as a superposition of turbulence on a random train of rectangular waves, then the superposition will carry over to the spectrum which should, in principle, be similarly decomposable into the bona-fide spectrum and the pseudoturbulent front signal. Returning to point (5) and Figure 65, we add here the observation, that when the "zeros" of the rectified wave were measured, they yielded a characteristic frequency (crossings of the wire into the turbulent front) also of about 30 kilocycles per second, in agreement with the spectrum measurement results. This frequency naturally also decreased near the axis and again near the wake edge, implying that Figure 65 shows the behavior of the front rather than of the turbulence itself.

Comments (1) through (4) can now be put into proper context. If our hypothesis is correct, then the front pseudoturbulence should be most intense in regions of the most intense intermittency, which occurs at about the middle of the wake radius; this is in agreement with Comment (1). The pseudoturbulence decay, commented on in (2) is, of course, fully predictable. Observation (4) is also easy to interpret because the momentum exchange between the large corrugations of the front and the external flow is probably much more efficient than the exchange of heat. On the other hand, the exact interpretation of the frequency shift is in some doubt. If our hypothesis is true that the front (interface) is indeed weakly periodic, then this frequency should be characteristic of the wavelength of the front corrugations. Because the axial velocity of the front, itself unknown,

must vary in the axial direction, at least initially, there is little useful information the initial peak frequency shift can supply. At the same time, the apparent relaxation of the peak frequency location to about 30 kilocycles per second (see Figure 65) is consistent with observations (Reference 22) of the frequency of "zero occurrences" which was also of about 30 kilocycles per second. As we saw from the spectra, this corresponds to a scale about 12 times higher than the typical macroscale size, which implies a length of between 6L and 12L where L is the transverse scale of the wake. From measurements of the intermittency and zeros, the former agrees with the microscale of the wake front and is thus advanced here as a representative value of the wavelength of the front.

In summarizing, the only new phenomenon emerging from the spectral measurements is not necessarily the inevitable mixing of the turbulent signals with the pseudoturbulence of the front, but rather that the latter is not, apparently, truly random. This organization of the latter into a weakly periodic structure serves at least as an identification of the pseudoturbulent action and could be of potential use in separating the turbulent from the pseudoturbulent phenomena.

The discussion of the modal-spectral analysis will be concluded with a brief glance of the spectral distribution of the velocity-temperature cross-correlation coefficient, as presented in Figure 66. It is seen that anti-correlation is generally most perfect for the largest eddies lying on the wake axis near the transition zone, while it is poorest for the smallest eddies, again on the axis, but far downstream. It is especially interesting that correlation is generally best for the largest eddies at any rate, verifying Morkovin's conclusion that these eddies are the ones responsible for transport across the gradient.

The errors involved in this measurement are in general very difficult to estimate accurately. Estimates can only be made of the sources of error, and the specific techniques reducing such errors can be equally well identified. Thus, major error-producing mechanisms were (1) the inherent

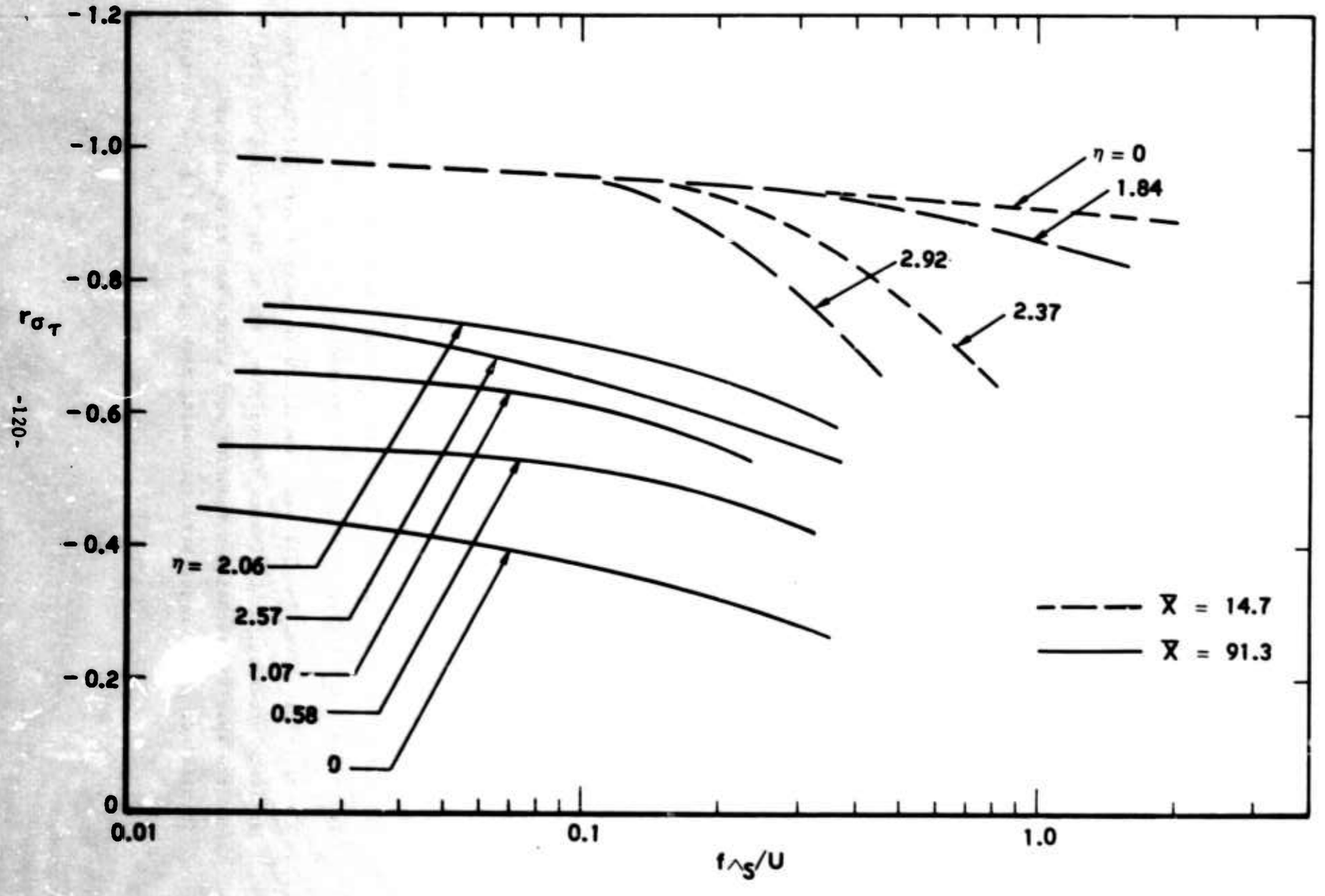

FIGURE 66. SPECTRAL RESOLUTION OF THE VELOCITY-TEMPERATURE CROSS-CORRELATION COEFFICIENT.

alignment difficulties of axi-symmetric models, (2) slight differences in re-installing and re-aligning the model each time it had to be removed from the test section, (3) not fully satisfactory wind tunnel flow (from the standpoint of uniformity), (4) differences in wire characteristics, since the inevitable wire breakages required the uses of many wires,* and (5) unavoidable imperfections in the transfer-function technique. On the other hand, the care exercised in calibrating wires and identifying the strain gage problem has been of great help in reducing anomalies in the data.

By neglecting the sound fluctuations in analyzing the data we have in effect stated that the normalized pressure fluctuations are insignificant compared to the density and temperature fluctuations. In this context the self-consistency of the experiment can be checked by computing the pressure fluctuations induced by velocity fluctuations as

$$\frac{\Delta p}{p} \simeq - \frac{\gamma}{2} M^2 \left(\frac{\Delta u}{u}\right)^2 \qquad (92)$$

where M is the Mach number. The following tabulation presents results obtained for two radial locations at $\bar{X} = 14.7$. The agreement with the imposed condition seems very satisfactory, particularly away from the axis.

Comparison of Pressure and Density Fluctuations

y (inch)	M	$(\Delta u/u)$	$(\Delta p/p)$	$(\Delta \rho/\rho)$
0	1.37	0.24	0.075	0.120
0.10	2.76	0.055	0.016	0.16

The large fluctuation levels encountered naturally cast some doubt on the validity of the technique and the analysis used to reduce the data. Specifically, at least three possible sources of error arise: (1) the wire heat transfer characteristic may be highly nonlinear over the range of the

* The lesson learned is that with critical or delicate model geometries and equally delicate hot wires, one obtains the data as fast as practical without disturbing the model in the meantime.

fluctuations, (2) the wire may become sensitive to the transverse as well as the axial component of the fluctuations in the velocity vector, and (3) the fluctuation modes interact nonlinearly among themselves so that the modal analysis into entropy and vorticity fluctuations is invalid. Because higher-order moments in the turbulence variables greatly complicate the formulas, an exact computation of the errors due to these nonlinearities is impossible, although some rough estimates can be made. Thus, the heat transfer characteristic of the wire is more linear ($Re_o \sim Nu_o$) at the lower Reynolds numbers than at the higher ones and thus derivatives such as $\partial^2 Nu_o/\partial Re_o^2$ are very small; the instrument is therefore more linear at these low Reynolds numbers. The inclusion of nonaxial velocity fluctuations, roughly speaking, sets an error in ($\Delta u/u$) of about 15 percent for fluctuation on the order of 0.2, but the error decreases rapidly with the fluctuation level, i.e., as one moves away (axially or radially) from the point of maximum level. The nonlinear interaction of modes is difficult even to estimate except perhaps for interaction involving sound (see Reference 15).

There is, too, the problem of possible distortion of the mean measurements because of the high turbulence level. Fortunately, the reduction of the mean data rested on the static pressure which is largely insensitive to the fluctuations and on the total temperature which was not found to fluctuate much. These facts, coupled with the insensitivity of the pitot tube to the turbulence, indicate that the (p_T, p, T_o) group of measurements should be always preferred over the (p_T, p, Re_o) group for mapping the mean field in highly turbulent flows.

SECTION 8

CONCLUSIONS

On the basis of the work performed to date, the following conclusions can be drawn regarding the turbulent wake investigated:

(1) The transition to turbulence of the axisymmetric was clearly triggered by the amplification of a laminar instability. The highest local fluctuation levels observed lay in or immediately downstream of the transition zone.

(2) The overwhelming majority of the turbulence properties tended to relax into a self-preserving form within a region of about 40 virtual diameters downstream of transition. However, the possibility exists that the relaxation distance is in general a function of the free-stream flow parameters.

(3) It has been verified that, on account of the small total temperature fluctuations measured, the so-called strong Reynolds analogy holds for wakes produced by adiabatic bodies.

(4) The radial distributions of the temperature (density) and axial velocity fluctuations, when scaled by factors drawn from the Reynolds analogy and the dynamic equilibrium hypothesis, appear to be identical with each other and to their low-speed counterparts. This similarity, occurring in the physical rather than the Howarth-Dorodnitzyn plane, verifies that the equilibration process is local and maintained by the larger eddies. Thus, the velocity and temperature fluctuations are well anti-correlated, mainly for the large eddies.

(5) The axis values of the velocity and temperature fluctuations are likewise in agreement with the qualitative and quantitative features of the dynamic equilibrium hypothesis.

(6) The velocity auto-correlation macroscale is, within the scatter, equal to the transverse wake scale, L; it is fairly constant with radius. In the self-preserving region (by contrast), the density auto-correlation macroscale is about 0.5 L on the axis and increases towards L at the wake edge; these two scales are not therefore everywhere equal to each other. By way of comparison, the maximum shear zone occurs at 1.1 L, the statistical wake front position is at 2.1 L, and the wake edge at 3.3 L.

(7) The normalized spectral densities of the velocity and temperature are virtually identical and uniform with radius in the self-preserving region. They are identical with the low-speed wake velocity fluctuation spectrum at the low frequencies, but of decreased intensity at frequencies corresponding to (and higher than) the macroscale.

(8) The spectral densities are distorted by the pseudoturbulence generated by the wake front intermittency, which is weakly periodic with a wavelength of about 6 L. The relaxation length of this pseudoturbulence appears to be longer than that for the turbulence within this front.

It should be reemphasized that the study presented here deals with an essentially steady-state system where Eulerian statistics are performed by an instrument stationary in a flowing gas. By this process, the resulting map of statistical properties contains a mixture of both the turbulence and the pseudoturbulence of the front. This composite picture is both legitimate and convenient for practical applications but it invites further work by which the turbulence due to the front will be separated from the bona-fide turbulence inside it. In this new, equally relevant representation, where the intermittency factor figures prominently, the radial distributions of properties reported herein will be altered by subtracting the front pseudoturbulence and adding an amount of turbulence normally unaccounted because of intermittency. Such work will be reported at a later date.

REFERENCES

1. Townsend, A. A., "The Structure of Turbulent Shear Flow," Cambridge University Press, 1956.

2. Cooper, R. D. and Lutzky, M., "Exploratory Investigation of the Turbulent Wakes Behind Blunt Bodies," David Taylor Model Basin Report 963, 1955.

3. Hwang, N. H. C. and Baldwin, L. V., "Decay of Turbulence in Axi-Symmetric Wake," ASME Paper.

4. Gibson, C. H., Lin, S. C., and Chen, C. C., Measurements of Turbulent Velocity and Temperature Fluctuations in a Wake of a Sphere, AIAA Paper No. 67-20, New York, January 1967.

5. Carmody, T., "Establishment of the Wake Behind a Disk," Journal of Basic Engineering; ASME Transactions, P. 869, December 1964.

6. Clay, W. G., Hermann, J , Slattery, R. E., "Statistical Properties of the Turbulent Wake Behind Hypervelocity Spheres," Physics of Fluids, Vol. 8, P. 1792, 1965.

7. Fox, J., Webb, W. H., Jones, B. G., and Hammitt, A. G , "Hot-Wire Measurements of Wake Turbulence in a Ballistic Range," AIAA Journal, Vol. 5, No. 1, P. 99, 1967.

8. Taylor, G. I., Proceedings of the Royal Society, London, Vol. 164A, 476, 1938.

9. Lykoudis, P. S., "A Review of Hypersonic Wake Studies," AIAA Journal, Vol. 4, No. 4, P. 577 to 590, 1966.

10. Morkovin, M. V., "Effects of Compressibility on Turbulent Flows," Coll. International Du Centre National de la Recherche Scientifique, No. 108: Mecanique de la Turbulence, Editions Du Centre National de la Recherche Scientifique, 15 Quai Anatole, Paris, France, P. 367, 1962.

11. Laufer, J., "The Fluctuating Field and Energy Spectrum of a Hypersonic Wake," excerpts from NESCO Report SN 219-2, Pasadena, California 1964.

12. Demetriades, A., "Mean Flow Measurements in an Axisymmetric Compressible Turbulent Wake," Philco-Ford Corporation Report U-3978, Newport Beach, California, March 1967; also to be published in AIAA Journal, 1967.

13. Demetriades, A. and Von Seggern, L., Design, Performance, and Operation of the Mach 3 Wind Tunnel, Aeronutronic Division of Philco-Ford Corporation, Report U-3390, November 1965.

14. Morkovin, M. V., "Fluctuations and Hot-Wire Anemometry in Compressible Flows," AGARDograph 24, 1956.

15. Kovasznay, L. S. G , "Turbulence in Supersonic Flow," Journal of Aeronautical Science, Vol. 20, No. 10, P. 657, October 1953.

16. Ladenburg, R. W. (Editor), "Physical Measurements in Gasdynamics and Combustion," High-Speed Aerodynamics and Jet Propulsion, Vol. IX, Chapter F, P. 213 ff, Princeton University Press, 1954.

17. Kistler, A. L., "Fluctuation Measurements in a Supersonic Turbulent Boundary Layer," Physics of Fluids, Vol. 2, No. 3, P. 290, May-June 1959.

18. Hinze, J. O., "Turbulence," McGraw-Hill, New York, 1959.

19. Favre, A., Gaviglio, J., and Burnage, H., "Observations of the Transition of a Supersonic Wake," ONERA, 1967.

20. Favre, A., et al., Reserche Aeronaut., Paris, No. 32, P. 21, 1953.

21. Corrsin, S. and Kistler, A. L., "Free-Stream Boundaries of Turbulent Flows," NACA TR 1244, Washington, D.C., 1953.

22. Demetriades, A., "Turbulent Front Structure of an Axisymmetric Compressible Wake," (to be published).

APPENDIX A

THE TRANSFER FUNCTIONS

A.1 HOT WIRE

The transfer function W of the hot-wire is given by

$$\frac{e(f)_{wire}}{e(f)_{flow}} = \frac{1}{W(f)} = \left(1 + 4\pi^2 f^2 M^2\right)^{-1/2} \quad ; \; M \equiv \text{time constant.} \tag{A.1}$$

where the phase shift is not included; here f is the frequency and M the wire time constant. The latter is given by

$$M = \frac{C}{\alpha_r R_r}\left(1 - 2\alpha_r \frac{R_w - R_r}{R_r}\right) \frac{A_w'}{I^2 (1 + 2 \epsilon A_w')} \tag{A.2}$$

Here C is the overall heat-capacity of the wire

C = (density) x (specific heat) x (volume)

$\alpha_r R_r$ the oven-calibration resistance-temperature slope, R_w the heated and R_r che equilibrium wire resistance, I the current, A_w' the overheat

$$A_w' \equiv \frac{1}{2}\frac{I}{R}\frac{\partial R}{\partial I} \tag{A.3}$$

and ϵ the finite circuit factor which was measured to be 0.008 in our case. The quantity α_r is zero in our case and thus we can re-write (A.2) as

$$M = \frac{c\rho\pi r^2 \ell}{\alpha_r R_r} \frac{A'_w}{I^2} \text{ seconds} \tag{A.4}$$

Where the specific heat c, density ρ, wire radius r, and length ℓ etc., are given in cgs units. The transfer function W is then given by combining (A.1) with (A.4).

At this juncture, it is appropriate also to give the limiting value of M at zero current. By (A.3) and (A.4) we get

$$M = \frac{c\rho\pi r^2}{\alpha_r R_r} \frac{1}{2\bar{e}} \frac{\partial R}{\partial I} \tag{A.5}$$

where $\bar{e}$ is the dc voltage. We recall that at zero current the Nusselt number is

$$\lim_{I \to 0} Nu_o = \frac{\alpha_r R_r}{\pi \ell k_o} \frac{R_{awm}}{\partial R/\partial I^2} \tag{A.6}$$

and since at $I \to 0$

$$R \to R_{awm}$$

and

$$\frac{1}{R} \frac{\partial R}{\partial I^2} = \frac{1}{2\bar{e}} \frac{\partial R}{\partial I}$$

the combination (A.5) and (A.6) gives

$$\lim_{M \to 0} = \frac{c\rho r^2}{k_o Nu_o} \tag{A.7}$$

A.2 AMPLIFIER

The zero-frequency gain G_o of the amplifier is given in Figure A-1. The amplifier transfer function G/G_o has been calibrated for different attenuation settings, is shown on Figure A-2, and has been curve-fitted by

$$\frac{G}{G_o} = \left[1 + (1.25)\ 10^{-12}\ f^2 + (0.75)\ 10^{-17}\ f^3\right]^{-1} \qquad (A.8)$$

where f is in cycles per second.

A.3 COMPENSATOR

When the compensator time-constant dial is set at M_s (which is equal to M_I of program WEB-II) the compensator transfer function is

$$C = \frac{\left|1 + 39.6\ M_s^2\ f^2\right|^{1/2}}{1 + (0.705)\ 10^{-2}\ f\ M_s + (0.369)\ 10^{-3}\ f^2\ M_s^2 - (3.2)\ 10^{-6}\ f^3\ M_s^3} \qquad (A.9)$$

which has been measured to 500 kilocycles per second and is shown in Figure A-3.

A.4 RMS METER

The transfer function of the Ballantine rms meter set at 300 millivolt full scale is

$$e_{VTVM} = \frac{24\sqrt{E}}{1 + \frac{0.297}{\sqrt{E}} - \frac{0.261}{E} + \frac{0.364}{E^{3/2}}} \qquad (A.10)$$

where E is the dc voltage output from the mean square jack on the meter in millivolts. For the 1-volt full-scale setting this is

$$e_{VTVM} = \frac{74\sqrt{E}}{1 - \frac{0.13}{\sqrt{E}} + \frac{0.685}{E} - \frac{0.194}{E^{3/2}}} \qquad (A.11)$$

These curves are shown on Figure A-4.

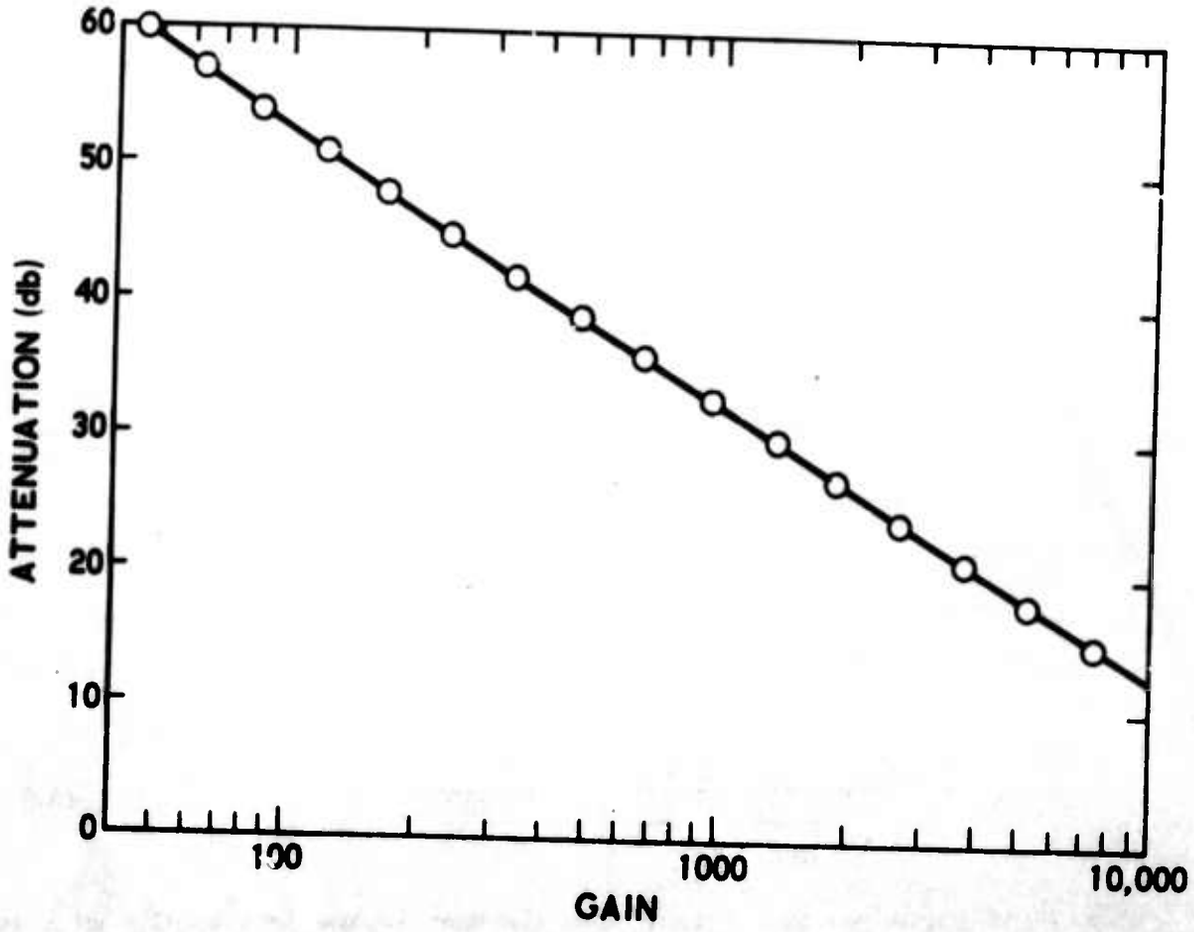

F09840 U

FIGURE A-1. CALIBRATION OF THE ZERO-FREQUENCY GAIN G_o OF THE HOT-WIRE AMPLIFIER.

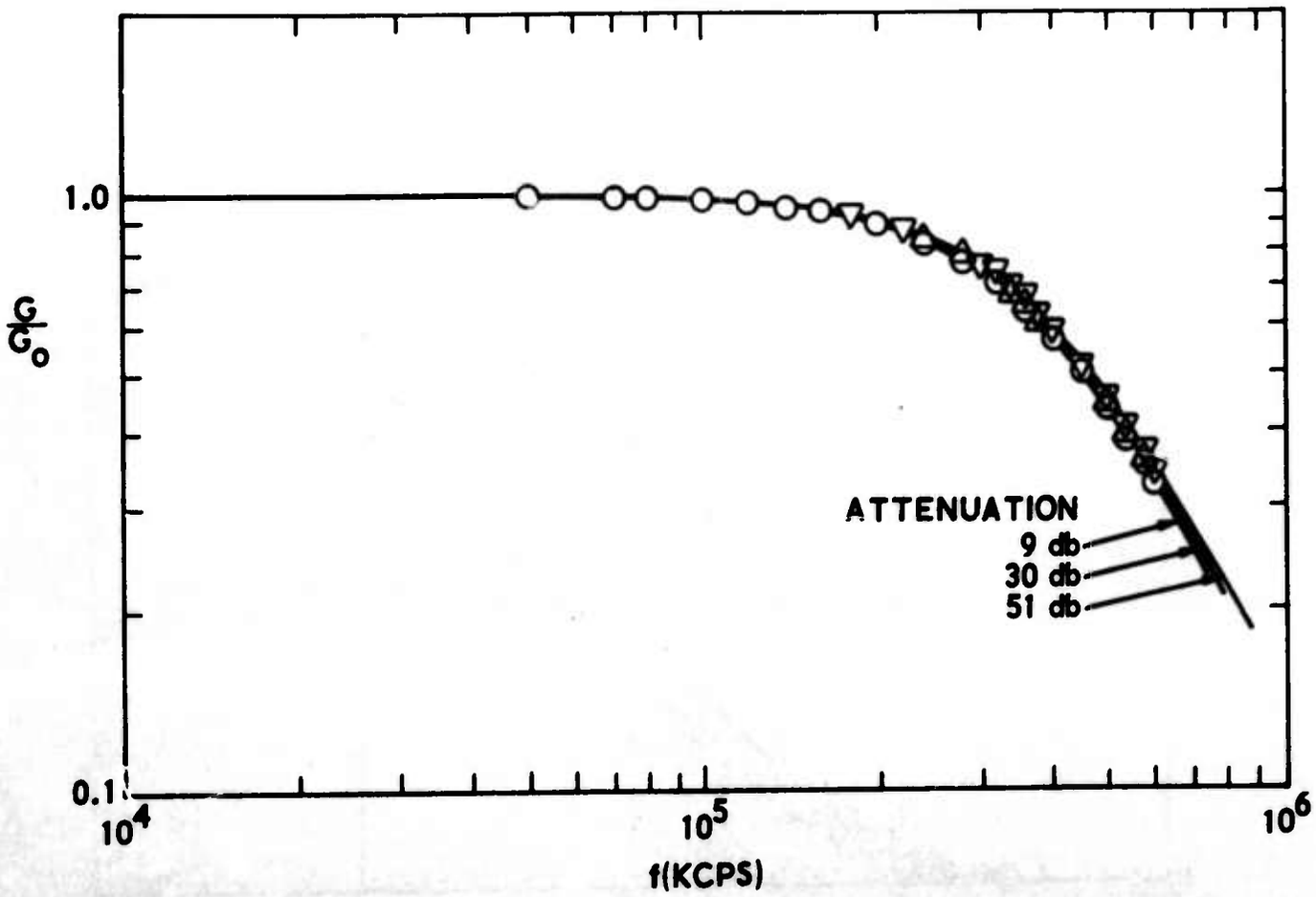

F09841 U

FIGURE A-2. TRANSFER FUNCTION OF THE AMPLIFIER, SHOWN TO BE INDEPENDENT OF ZERO-FREQUENCY GAIN.

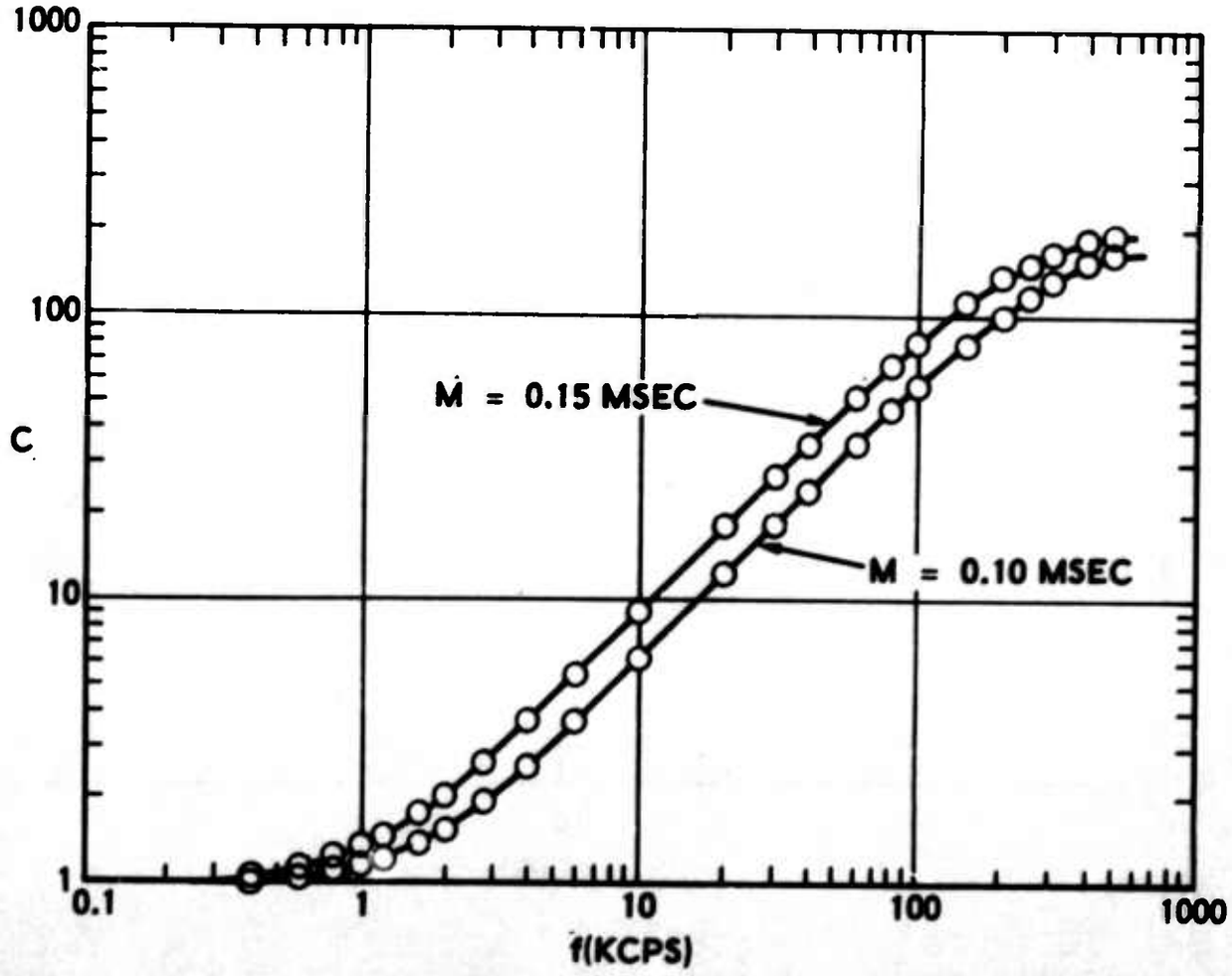

F09842 U

FIGURE A-3. TRANSFER FUNCTION OF THE COMPENSATOR FOR TWO SETTINGS OF THE TIME CONSTANT.

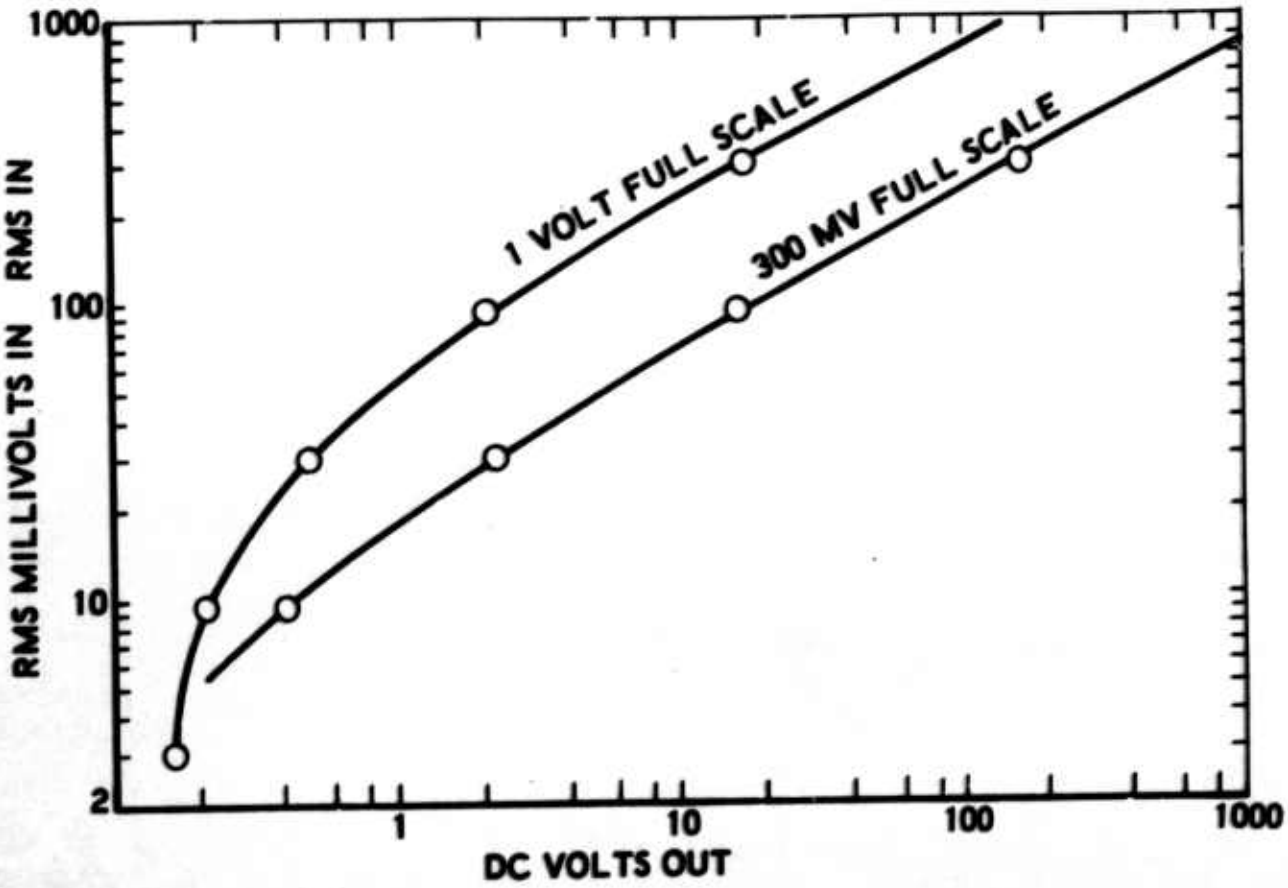

F09843 U

FIGURE A-4. TRANSFER FUNCTION OF THE RMS VOLTMETER FOR TWO FULL-SCALE SETTINGS.

A.5 WAVE ANALYZER

A.5.1 BANDWIDTH

As Figure A-5 shows, checks made on the frequency-independent, selectable bandwidth of the wave analyzer showed excellent filtering characteristics at 0.2-, 3- and 1-kilocycle-per-second width; the latter is used for the measurements.

A.5.2 TRANSFER FUNCTION

The transfer function H, shown in Figure A-6, was found to be independent of frequency; tests are always made at the settings ABSOLUTE, NORMAL, 1 VOLT f.s., -10 decibels down and using a 1000-ohm load. In this case, an rms input of e millivolts is converted to dc millivolts V by

$$e = \frac{V}{H}$$

where

$$H = 0.312 + \frac{3}{V} - \frac{32.94}{V^2} + \frac{33.33}{V^3} \qquad \text{(A.12)}$$

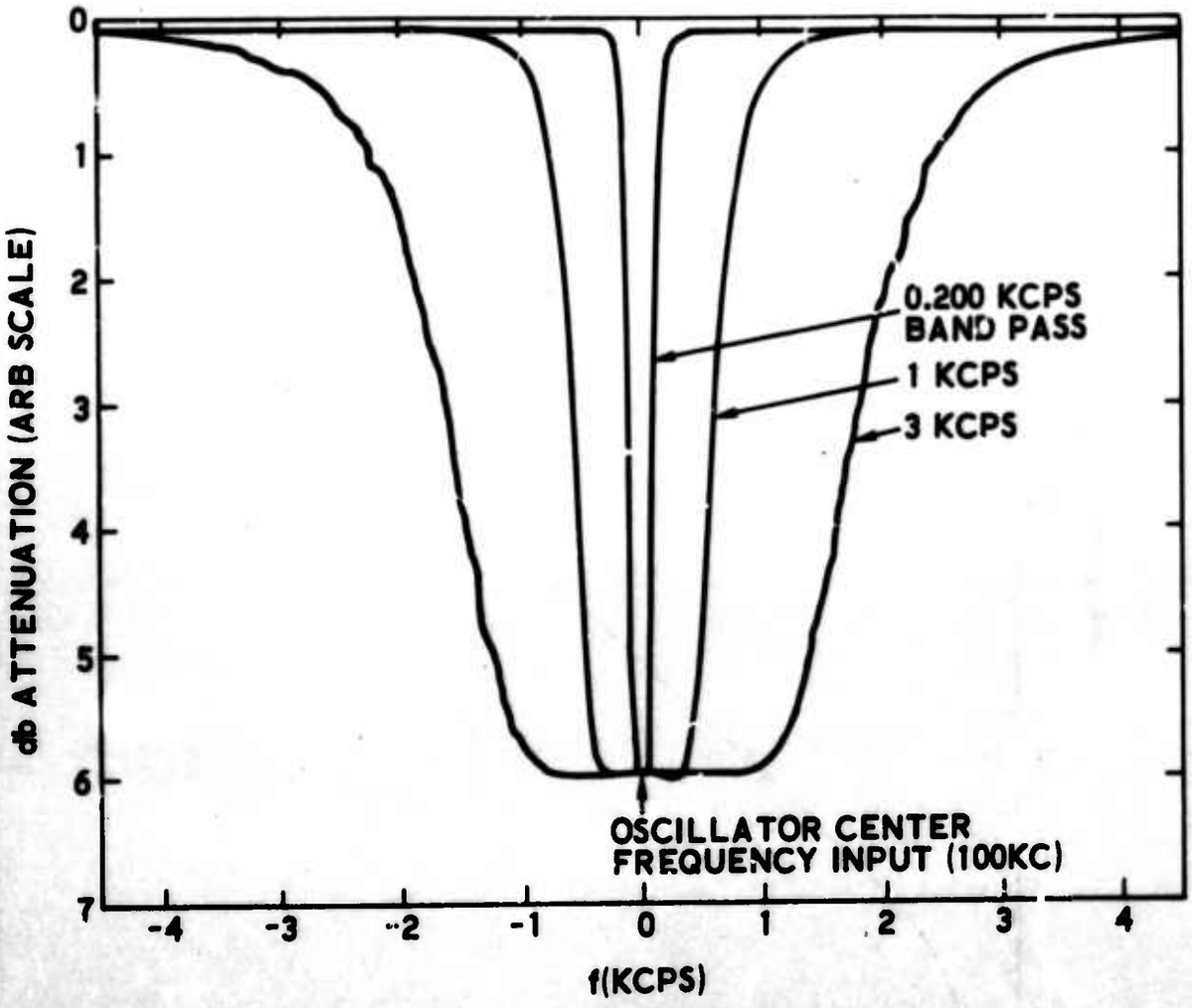

F09844 U

FIGURE A-5. FILTERING CHARACTERISTICS OF THE WAVE ANALYZER AT EACH OF ITS THREE BANDWIDTHS.

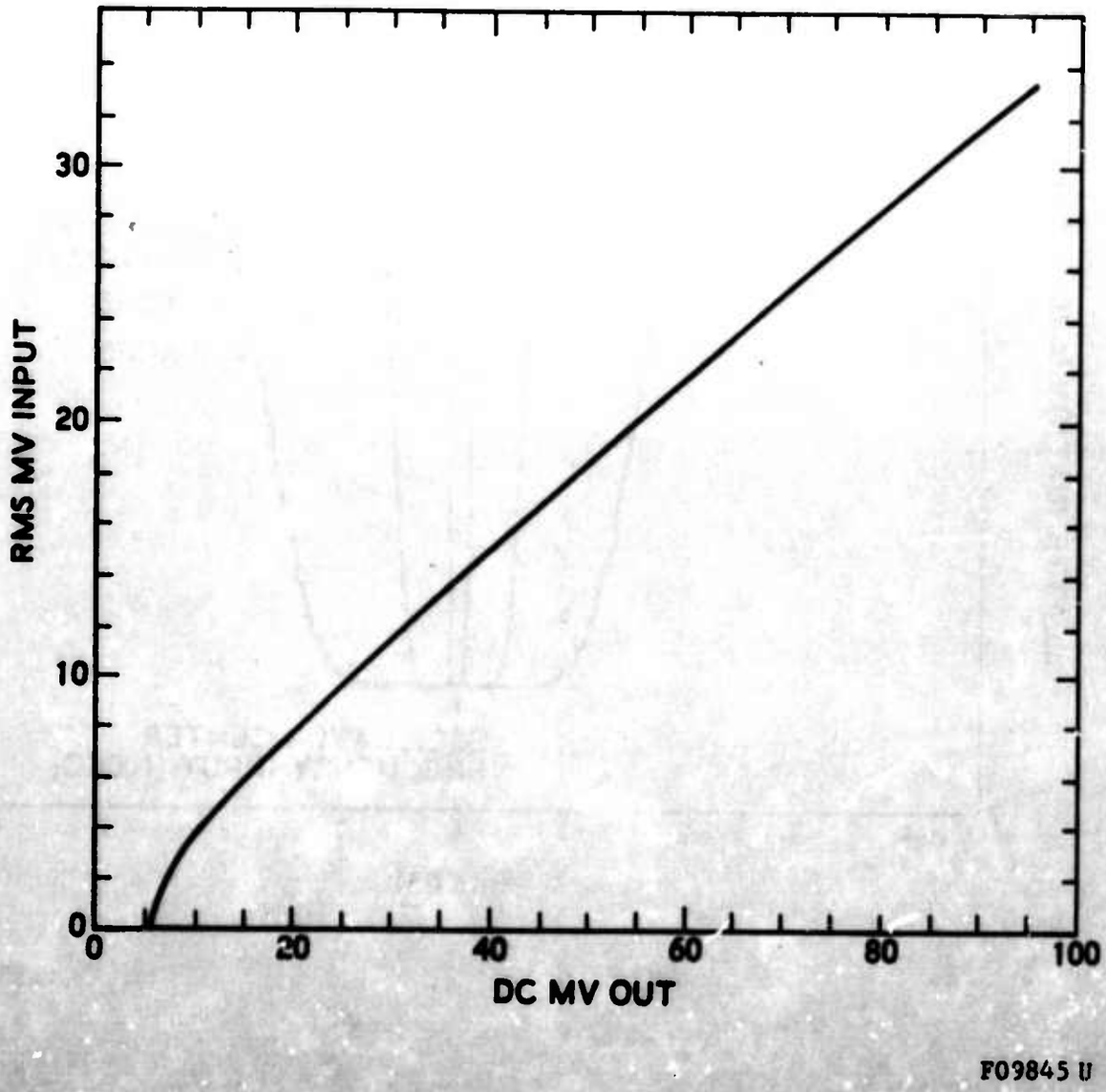

FIGURE A-6. TRANSFER FUNCTION OF THE WAVE-ANALYZER DETECTOR.

APPENDIX B

THE WEB-II COMPUTER PROGRAM

The general purpose of this program is to nullify the frequency-response deficiencies of the apparatus in measuring the frequency-integrated voltage output of the hot-wire at each current and each point in the wake. This is done as follows in each case: the output spectrum is recorded, the overall transfer function measured, and an error-ratio formed from the spectrum measurement alone, indicating how much the measured integrated wire output should be increased to account for apparatus deficiencies.

Each spectrum, taken in the range of 0 to 500 kilocycles per second is first broken into 7-kilocycle-per-second intervals (the latter increase at the higher frequency end) and the analyzer signal and noise output noted and the spectral density of the signal determined; integrated over the spectrum this gives the integrated wire output e^2_{VTVM}. In the meantime, the transfer functions of the amplifier and compensator are evaluated at each frequency. The transfer function of the wire is found as follows: the wire time constant outside the wake is known (for each current and axial position), as is its current-voltage curve. The local time constant at each point in the wake is then found by the formula given in the main text, and the local transfer function of the wire is computed and combined with the others to form the overall transfer function CTF. The value of

the latter at each frequency is now combined with the net wave analyzer output at that frequency to give the ideal hot-wire output at that frequency; integration then leads to the ideal integrated wire output e^{*2}_{VTVM} at that point and current. The error ratio J is formed by e^2_{VTVM} and e^{*2}_{VTVM} and combined with the wire output e^2_{OVTVM} measured with the rms voltmeter to correct the latter.

At each current and point in the wake the program output presents, among other quantities, the wire time constant M (M(MSEC)), the ideal and actual integrated wire outputs e^{*2}_{VTVM} (VTVM*2) and e^2_{VTVM} (VTVM2), respectively, as computed from the spectrum, the same quantity as measured directly e^2_{OVTVM} (EO2), the error ratio J, and the final corrected integrated wire output e^2 (E2). Further, at each station and current the following are among quantities given as a function of the frequency f (FKCPS): the net analyzer output V^2 (f), the wire, amplifier, and compensator transfer functions W, G/G_o and C, respectively, the overall transfer function OTF, and the net wire signal power density in $(volts)^2/cps$.

As noted from the above remarks, this program provides a meticulous and detailed view of the behavior of the complete electromechanical system over the entire matrix of operating situations. In addition to the new insight it offers into the technique of anemometry, it affords numerous cross checks of the procedure and increases accuracy. More importantly, the output can now serve as a starting input for a combined modal-spectral analysis (i.e., the spectra of the velocity or density fluctuations alone), a task normally so cumbersome that it has been attempted only once previously.

The procedural diagram of WEB-II is shown on Figure B-1.

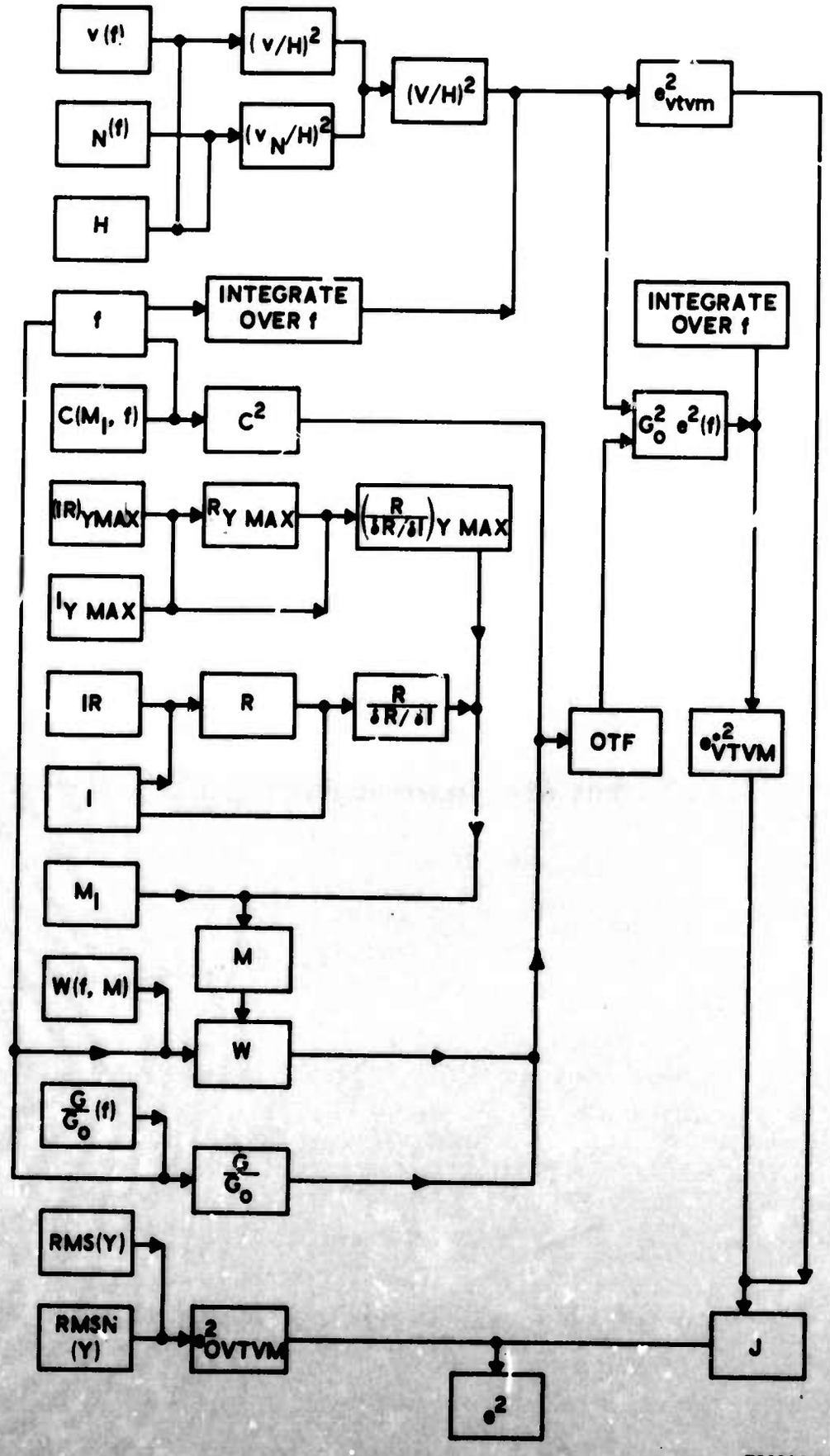

F09846 U

FIGURE B-1. THE WEB-II PROGRAM

APPENDIX C

THE WEB-III COMPUTER PROGRAM

The purpose of this program was to process the turbulence data through the response-restoration process of the WEB-II program and to prepare them for the eventual analysis into frequency-integrated modes (performed with the WEB-IV program).

The basic inputs to this program are the 15 radial traces of integrated raw hot-wire turbulence signal (1 for each of 15 currents) and the corresponding 15 traces of mean wire voltage; the error ratio J is also put in. The coordinates of each trace (distinguished by T for the turbulence and S for the mean or steady traces) are supplied by an analog-to-digital card-punch as "counts;" by appropriate conversion factors (F_T and F_S), these traces are reduced into curves of voltage ET versus radial distance Y. Utilizing the transfer function of the rms voltmeter, the root-mean-square of the turbulent signal (RMST) is obtained. This process is performed by taking discrete points, 20 in all, for each x station. After subtraction of the noise RMSN, the actual integrated wire voltage output at these points is known, and can now be corrected for the ideal response by using the error ratio J (cf. WEB-II program). As one recalls, J had been obtained at 8 currents I, not 15 as available in this program, and also at 10, rather than 20 radial positions; interpolation thus became necessary, and the J's so obtained were then used to get the ideal integrated turbulence signal.

In similar fashion, the mean wire voltage $\bar{e}_s$ was obtained for each point using level L from the plotter curves, corrected into $\bar{e}$ to account for the line resistance (1.04 ohm), squared and combined with e^2 to form the ideal nondimensional frequency-integrated (but amplified) wire turbulence output at each current and point; this was further reduced by dividing by the zero-frequency amplifier gain G_o. Finally, the wire overheat parameter A_w', against which $(e^2/e^{-2})/G_o^2$ is given in the output was formed.

The computing procedure for this program is shown in Figure C-1.

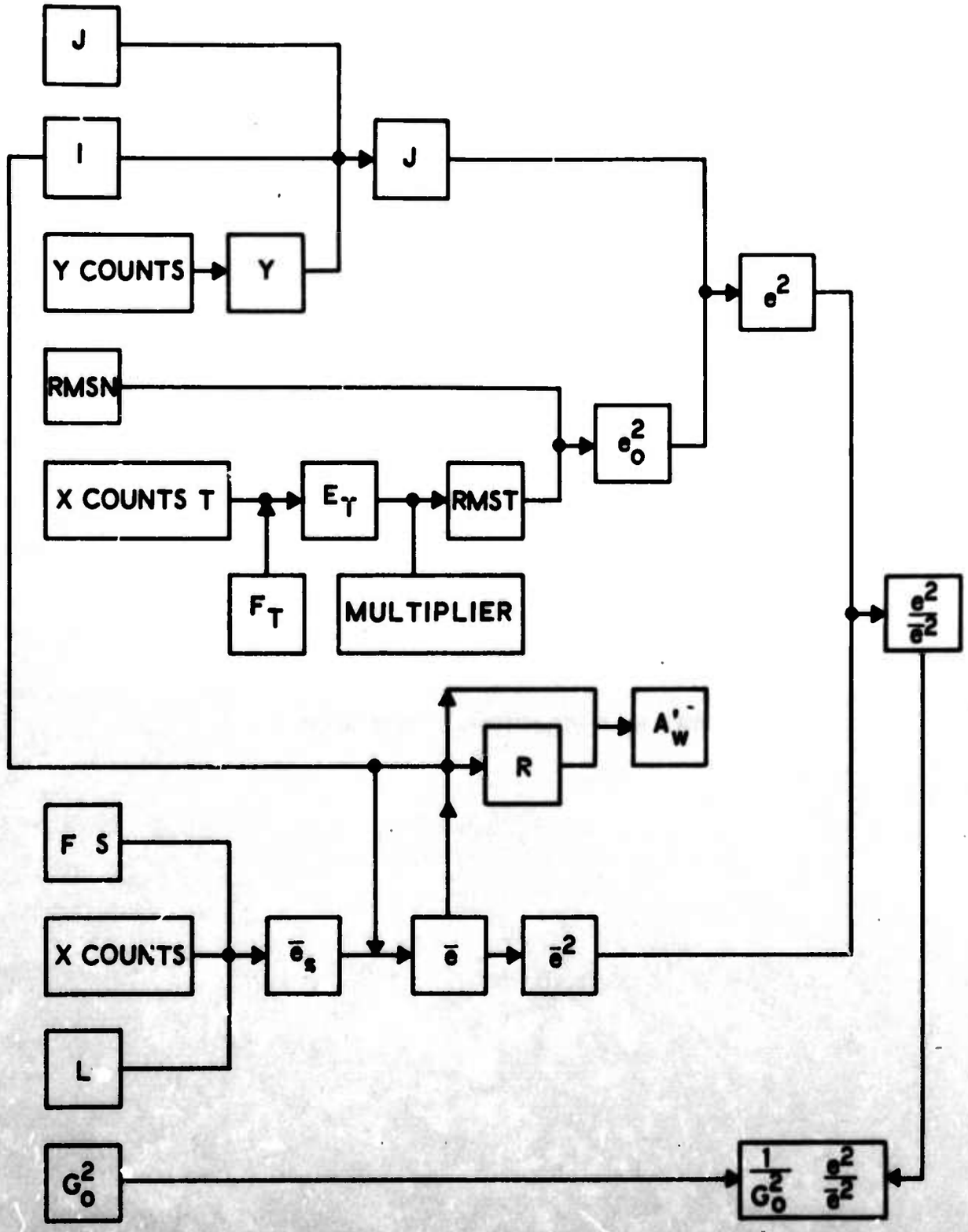

F09847 U

FIGURE C-1. THE WEB-III PROGRAM

APPENDIX D

THE WEB-IV PROGRAM

The purpose of this program was to supply the modal analysis of the radial distribution of frequency-integrated turbulent fluctuations; final objective was therefore to give the velocity and density fluctuations and their correlation as a function of radius and axial position along the wake.

As a first step, the program prepared a list of the flow properties at each point in the wake, as derived by the WEB-I program; the location of these points (20 per x station) were the same as in WEB-III. Various combinations of these flow properties were computed preparatory to insertion in the wire sensitivity coefficients. Since the Reynolds number Re_o and the Re_o-Nu_o and Re_o - η relations were known fr a the flow calibration, the logarithmic derivatives (Re_o/η) $(\partial\eta/\partial Re_o)$ and (Re_o/Nu_o) $(\partial Nu_o/\partial Re_o)$ were computed, as was the wire temperature T_w at each current and the attendant values of τ_{wr} and K. The circuit parameter C_f was computed from the previously measured A'_w. At this point, sufficient information existed for computing the wire sensitivities to the mass flux (e_m) and total temperature (e_T) fluctuations. Use of the local Mach number M(Y) also allowed computation of similar sensitivities e_σ and e_τ to the entropy (temperature) and vorticity (velocity) fluctuations, respectively.

At this point, the net ideal integrated mean square wire voltage $e^2/G_o^2\bar{e}^2$ from WEB-III was introduced at each point and current, giving 15 second-degree polynomials (for the mass flux and T_o representation) with known coefficients, and a similar group for the entropy-vorticity representation. A least-squares solution of these did not work out, and therefore they were solved by fitting them to a second-degree curve, obtaining the mass flux and total temperature fluctuations and their correlation m, t, and r_{mt}, respectively, the corresponding vorticity (τ) and entropy (σ) fluctuations, and the correlation $r_{\tau\sigma}$. Finally, these fluctuations were also given normalized to the local velocity and density differences (u_∞ - u(0)) and ρ_∞ - $\rho(0)$ across the wake, as put in from the WEB-I program.

The computations procedure for this program is shown in Figure D-1.

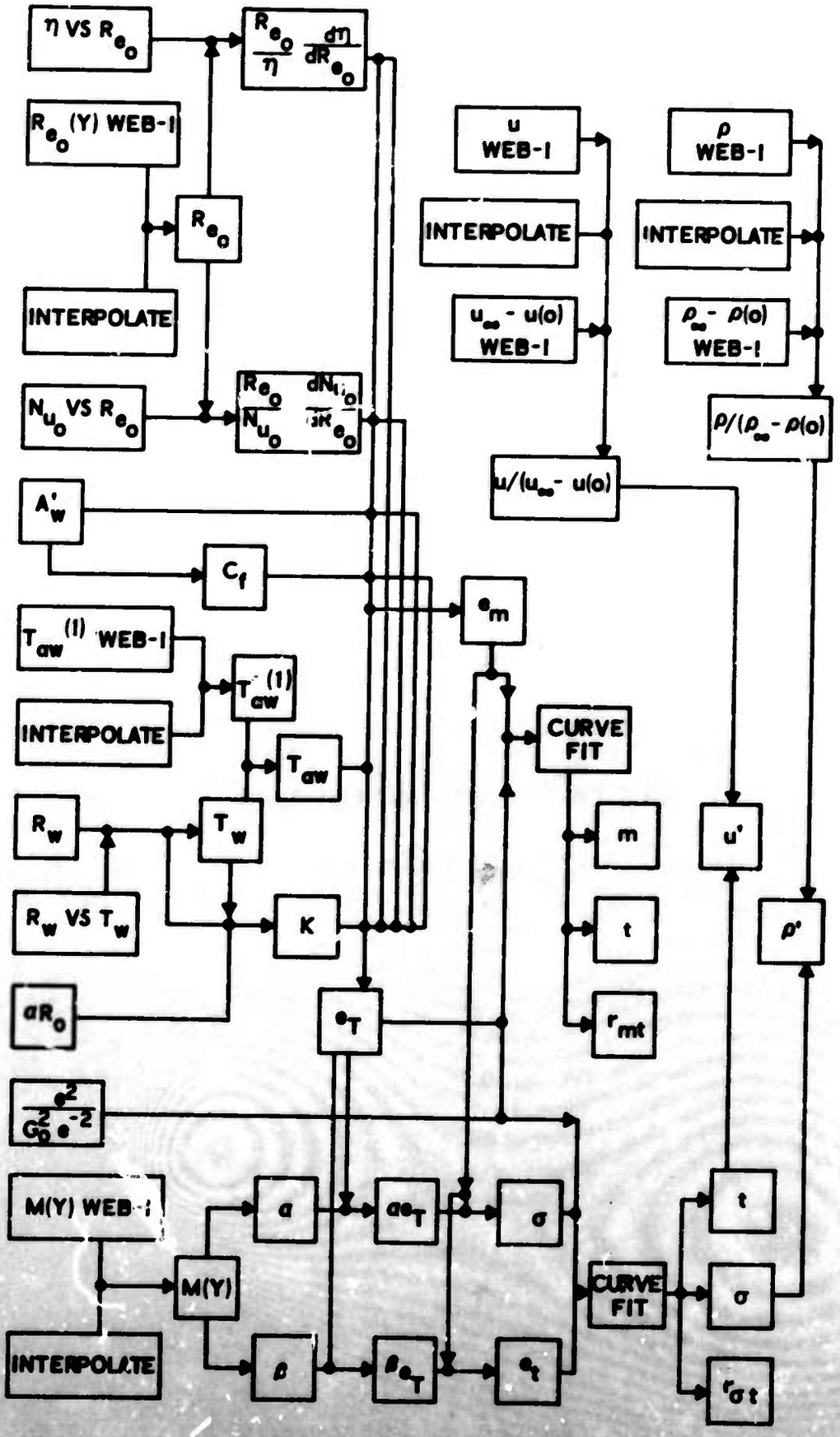

FIGURE D-1. THE WEB-IV PROGRAM

F09848 U

APPENDIX E

THE WEB-VII COMPUTER PROGRAM

The purpose of the WEB-VII computer program is (1) to perform the combined modal-spectral analysis of the turbulent flow and (2) to further manipulate the modal results of the WEB-IV program in order to get parameters interesting from a theoretical viewpoint. Thus, this program supplies spectra, macroscales, turbulent energy ratios and the like.

E.1 MODAL-SPECTRAL ANALYSIS

Here we want to find the fluctuation density at each frequency and at each point in the wake. The main input is the corrected "flow" voltage fluctuation $G_o^2 e^2$, a function of the frequency, which is given in millivolts squared per kilocycle and appears on the last column of the WEB-II outputs. This quantity, it should be noted, appears multiplied by the amplifier zero-frequency gain (squared) G_o^2, and is first divided by the latter to give EZFLOW $(mv)^2/kc$. By dividing the latter by $(IMA)^2$ $(ROHMNET)^2$ $(mv)^2$ we get the normalized (modally integrated) fluctuation density (per kc) at the particular frequency z^2, and by further dividing by the entropy fluctuation coefficient squared $(ES)^2$ (obtained by interpolation for the particular current IMA and YSTATION) we get the Kovasznay-Morkovin variable

$$z_n^2 = \frac{z^2}{(ES)^2}$$

Now we can proceed with the modal analysis at <u>each frequency</u> by solving simultaneously the eight equations

$$Z_{n_i}^2 = D\delta_{n_i}^2 + E\delta_{n_i} + F$$

where i=1, 2.....8 corresponds to each of the 8 wire currents employed in WEB-II for that frequency; here, of course, the variable δ_{n_i} is the ratio of the sensitivity coefficients

$$\delta_n = \frac{ETAU}{ES}$$

This solution gives the results

$$\tau^* = D^{1/2}$$

$$\sigma^* = F^{1/2}$$

$$r_{\sigma\tau}^* = \frac{E}{2\tau^* \sigma^*}$$

with the star denoting spectral density - e.g., τ^* is the rms velocity fluctuation (normalized to the <u>mean local velocity at that point</u>) per kilocycle. Corollary quantities formed by this program are τ^{*2} and σ^{*2} and

$$\tau^2 = \frac{\tau^{*2}}{1000}$$

$$\sigma^2 = \frac{\sigma^{*2}}{1000}$$

The latter are the mean-square velocity and density (temperature) fluctuation density, normalized with the square of the local mean velocity and density, respectively, <u>per cycle per second</u>. One quantity of interest, put out by WEB-VII, is the comparison of the quantities τ^*/σ^*. Another is the spectral density of each mode <u>squared</u> compared with the frequency-integrated mode

$$\frac{\tau^{*2}}{\Sigma\tau^{*2}} \text{ and } \frac{\sigma^{*2}}{\Sigma\sigma^{*2}}$$

where

$$\Sigma\tau^{*2} \equiv \frac{1}{1000}\int_0^\infty \tau^{*2}\, d_f$$

$$\Sigma\sigma^{*2} \equiv \frac{1}{1000}\int_0^\infty \sigma^{*2}\, d_f$$

where the 1000-factor appears in order to convert to integrand into cycles per second (since τ^{*2} and σ^{*2} are obtained within kilocycle "windows"). The latter two integrals should obviously be equal to the integrated velocity and density fluctuations, respectively, at that point in the wake.

The pertinent integral scales (macroscales) are computed from the relations

$$\Lambda_S \equiv \frac{u}{4}\,\frac{s^2(0)}{\Sigma\sigma^{*2}}$$

$$\Lambda_T \equiv \frac{u}{4}\,\frac{t^2(0)}{\Sigma\tau^{*2}}$$

where u is the local flow velocity (obtained from the WEB-I output) and $s^2(0)$ and $t^2(0)$ are the limit values of s^2 and t^2 at zero frequency. In the present instance these quantities were evaluated at 7 kilocycles per second. Because both numerator and denominator in the latter two equations are each normalized to the local mean values, the definition of the scales is independent of these values.

This program finally outputed the nondimensional spectra $s^2/s^2(0)$ and $t^2/t^2(0)$ versus the nondimensional frequencies

$$n_t \equiv \frac{F(CPS)\,\Lambda_t}{u}$$

$$n_s \equiv \frac{F(CPS)\,\Lambda_S}{u}$$

Note that the latter outputs present best comparison between the spectra of these two modas, whereas the output represents best the portions of the spectrum contributing most heavily to each mode.

Other outputs gave comparisons of the scales with the transverse wake scale L (from WEB-V) and the virtual wake (drag) diameter $(C_D A)^{1/2}$.

This program also provided for the manipulation of certain quantities put out by the WEB-IV program; the following were formed as a function of position in the wake:

(1) The quantity TAU/SIGMA and the related quantity

$$SRA = \frac{SIGMA}{TAU} \frac{1}{(\gamma-1)\, M^2}$$

where M is the local Mach number.

(2) The rms velocity and density fluctuations at each XSTATION, each normalized with the axis value. (See UPRIME/UPRIMO and RHOPRIM/RHOPRIMO.)

(3) The local average turbulent energy divided by the local mean kinetic energy

$$\frac{\bar{E}_T}{\bar{E}_m} \equiv ENERGY = 3\tau^2 - 3.46\, r_{\sigma\tau}\, \tau\sigma$$

where we have assumed isotropy in order to compute the turbulent velocity vector from the measured longitudinal component, and where third- and higher-order moments are neglected.

(4) Other quantities manipulating the fluctuations according to the dynamic equilibrium hypothesis.

Typical outputs appear in Figure 41.